Technische Universität München
TUM School of Natural Sciences

Structure and Energetics of Metal-Water Interfaces from Atomistic Simulations

Thorben Eggert

Vollständiger Abdruck der von der TUM School of Natural Sciences der Technischen Universität München zur Erlangung eines

Doktors der Naturwissenschaften (Dr. rer. nat.)

genehmigten Dissertation.

Vorsitz: Priv. Doz. Dr. Martin Tschurl

Prüfende der Dissertation:

1. Prof. Dr. Karsten Reuter
2. Prof. Dr. Christopher Stein

Die Dissertation wurde am 15.02.2024 bei der Technischen Universität München eingereicht und durch die TUM School of Natural Sciences am 09.04.2024 angenommen.

Für meine Familie.

Abstract

Solid-liquid interfaces are at the core of many relevant technologies like fuel cells and electrolyzers, which are prominent solutions for energy storage and production of hydrogen as a future energy carrier. Even though these devices have become more efficient over the past decades, their widespread use is limited by their high cost, which originates to a large degree from expensive e.g. platinum-based catalysts. Identifying and characterizing the catalytic centers as well as their reactivity under realistic conditions is therefore of utmost importance to designing new catalysts for reactions at solid-liquid interfaces. Advances in computing power and atomistic modeling techniques allow today to predict the catalytic activity with semi-quantitative accuracy from atomistic simulation. Nonetheless, the computational cost for an exhaustive sampling of catalyst-electrolyte interfaces under realistic conditions is still prohibitively expensive, which necessitates the use of simplifications e.g. the omission of the electrolyte or the idealization of the catalyst.

In this thesis, the detailed structure and energetics of metal-water interfaces are analyzed using atomistic simulations. First, a protocol is developed to represent interfacial water as two-dimensional, ice-like films, which capture a wide variety of structural motives that are similarly diverse as found in more demanding molecular dynamics simulations of a full liquid electrolyte. The resulting dataset allows the assessment of the sensitivity of the energetics towards the detailed arrangement and intermolecular connectivity of static water layers, which remain the predominant interfacial models to study interfacial electrochemical reactions, e.g. the adsorption process of a proton. However, interfacial water does not only act as an inert environmental matrix within which electrochemical reactions happen. It can equally influence more directly the free energy change by an adsorbing, reactive species. In particular, interfacial water can compete with any other adsorbate for free, catalytically active surface sites. The second part of this thesis quantifies such effects by measuring cavity formation energies at different metal-water interfaces from exhaustive free energy calculations. The study reveals a simple and direct relation between the binding strength of water to a substrate and the energetic cost of removing interfacial water to form an interfacial cavity which naturally occurs upon an adsorption reaction. These results imply a significant deviation of interfacial reactivity, e.g. when adsorption energies are studied in solution and compared to gas phase. On a broader scope, our results provide a pathway to correct computationally appealing implicit solvation models with their continuum representation of water to account for this competition.

Zusammenfassung

Fest-Flüssig-Grenzflächen sind integraler Bestandteil vieler relevanter Technologien wie Brennstoffzellen und Elektrolyseure, die herausragende Lösungen für die Energiespeicherung und die Produktion von Wasserstoff als Energieträger der Zukunft darstellen. Obwohl diese Geräte in den letzten Jahrzehnten immer leistungsfähiger geworden sind, ist ihr weit verbreiteter Einsatz durch ihre hohen Kosten begrenzt, die zu einem großen Teil auf teure Katalysatoren, z. B. auf Basis von Platin, zurückzuführen sind. Die Identifizierung und Charakterisierung der katalytischen Zentren sowie deren Reaktivität unter realistischen Bedingungen ist daher von größter Bedeutung für die Entwicklung neuer Katalysatoren für Reaktionen an Fest-Flüssig-Grenzflächen. Fortschritte bei der Rechenleistung und den atomistischen Modellierungstechniken ermöglichen es heute, die katalytische Aktivität mit semiquantitativer Genauigkeit aus atomistischen Simulationen vorherzusagen. Dennoch sind die Rechenkosten für eine umfassende Untersuchung von Katalysator-Elektrolyt-Grenzflächen unter realistischen Bedingungen immer noch unerschwinglich hoch, was Vereinfachungen, wie zum Beispiel das Weglassen des Elektrolyten oder das Idealisieren des Katalysators, erforderlich macht.

In dieser Arbeit wird die detaillierte Struktur und Energetik von Metall-Wasser-Grenzflächen mit Hilfe atomistischer Simulationen analysiert. Zunächst wird ein Protokoll entwickelt, um Grenzflächenwasser als zweidimensionale, eisähnliche Filme darzustellen, die eine Vielzahl von strukturellen Motiven erfassen, die ähnlich vielfältig sind wie bei anspruchsvolleren Molekulardynamiksimulationen eines vollständigen flüssigen Elektrolyten. Der daraus resultierende Datensatz ermöglicht die Bewertung der Empfindlichkeit der Energetik gegenüber der detaillierten Anordnung und der intermolekularen Konnektivität statischer Wasserschichten, die nach wie vor die vorherrschenden Grenzflächenmodelle zur Untersuchung elektrochemischer Grenzflächenreaktionen, z. B. des Adsorptionsprozesses eines Protons, sind. Grenzflächenwasser fungiert jedoch nicht nur als reaktionsträge Umgebungsmatrix, in der elektrochemische Reaktionen ablaufen. Es kann auch die freie Energieänderung durch eine adsorbierende, reaktive Spezies direkt beeinflussen. Insbesondere kann Grenzflächenwasser mit jedem anderen Adsorbat um freie, katalytisch aktive Oberflächenplätze konkurrieren. Im zweiten Teil dieser Arbeit werden solche Effekte durch Messung der freien Energiekosten zur Bildung einer Kavität an verschiedenen Metall-Wasser-Grenzflächen quantifiziert. Die Studie zeigt eine einfache und direkte Beziehung zwischen der Bindungsstärke von Wasser an ein Substrat und den energetischen Kosten für die Entfernung von Grenzflächenwasser zur Bildung einer Kavität, der natürlich bei einer Adsorptionsreaktion entsteht. Diese Ergebnisse deuten auf eine erhebliche Abweichung der Reaktivität an der Grenzfläche hin, wenn z. B. die Adsorptionsenergien in Lösung und in der Gasphase untersucht werden. Im weiteren Sinne bieten unsere Ergebnisse einen Weg zur Korrektur rechnerisch ansprechender impliziter Solvatationsmodelle mit ihrer Kontinuums Darstellung von Wasser, um diese Konkurrenz zwischen Adsorbate und Lösungsmittel zu berücksichtigen.

Abbreviations

AIMD *ab initio* molecular dynamics 21, 22, 29, 32, 33, 43

BAR Bennett acceptance ratio 16
BOA Born-Oppenheimer approximation 5, 7

CHE computational hydrogen electrode 20
CV collective variable 13–17, 43

DFT density-functional theory 6, 8, 9, 29

FEP free energy perturbation 14–17, 26, 43
FES free energy surface 13, 14, 16, 17, 23, 43
FF force field 7, 9, 19, 26

GGA generalized gradient approximation 9

LAMMPS large-scale atomic/molecular massively parallel simulator 10
LDA local density approximation 8, 9
LJ Lennard-Jones potential 9, 26, 27, 44

MBAR multistate Bennett acceptance ratio 16, 17, 31, 43
MD molecular dynamics 6, 10–12, 14–16, 22, 26, 31, 32, 43

PES potential energy surface 5, 6, 10, 11, 13, 14, 16, 43
PZC potential of zero charge 20, 21

SHE standard hydrogen electrode 1
SLI solid-liquid interface 16, 19, 22, 23, 26–28, 32, 44
SOAP smooth overlap of atomic positions 29
SPT scaled particle theory 24–26, 31

WCA Weeks-Chandler-Andersen potential 26–28, 44

Contents

Abstract v

Zusammenfassung vii

Abbreviations ix

1 Introduction 1

2 Theoretical Background 5
- 2.1 Potential Energy Surface 5
- 2.2 Density Functional Theory 7
- 2.3 Force Fields 9
- 2.4 Molecular Dynamics 10
- 2.5 Free Energy Surface 13
- 2.6 Free Energy Perturbation 15

3 Metal-Water Interfaces in Electrochemistry 18
- 3.1 Overview 18
- 3.2 Atomistic Simulations of Metal-Water Interfaces 19
- 3.3 Interfacial Cavity Formation 23

4 Publications 29
- 4.1 Static and dynamic water structures at interfaces: A case study with focus on Pt(111) 29
- 4.2 Cavity formation at metal-water interfaces 31

5 Conclusion and Outlook 32

List of Figures 44

Appendix 45
- Paper 1 47
- Paper 2 61

1. Introduction

Achieving the Paris Climate Agreement's goal of limiting global warming to well below $2.0\,°\mathrm{C}$ by 2100 requires an immediate and rapid reduction of carbon dioxide emissions [1]. For example, the European Union's agreed target is to reduce the emissions of greenhouse gases by at least $80\,\%$ (compared to 1990) by 2050 [2]. Therefore, the energy supply must shift quickly from typical carbon-based sources such as coal, oil, or natural gas to derivatives of renewable energy sources [3].

However, most renewable energy sources (like wind or solar power) do not offer consistent, scalable, electricity generation, but are instead subject to fluctuations during the day and seasons. This necessitates energy storage systems to balance this volatile behavior [4, 5]. Beyond the generation of electricity, hydrogen could replace fossil fuels because it has a high energy density, its combustion does not emit carbon dioxide, and it can be used as a reducing agent in chemical processes such as steel refining [6]. The large-scale generation of clean hydrogen from renewable energies is, therefore, an important step towards an emission-neutral world [7]. The electrochemical water splitting in electrolyzers and the reverse reaction in fuel cells are promising solutions to these challenges [4–6].

Currently, the production and demand of clean hydrogen are limited, as hydrogen production from fossil sources is significantly cheaper [7]. Two major challenges are the overall efficiency of electrolyzers and fuel cells and their cost [4, 8, 9]. Both are related to the catalysts used in the electrochemical processes. Many commercial fuel cells and electrolyzers operate at low temperatures with an acidic electrolyte and a polymer membrane to separate the half-cells [6]. The reactions take place over platinum-based catalysts, which are nanoparticles embedded in a matrix [8, 10]. Platinum is extremely rare and thus expensive, but the efficiency of platinum-based catalysts is comparatively high [8, 10–12]. For the oxygen evolution reaction, iridium and ruthenium oxides are employed, which are costly as well [4, 9]. Better catalysts would be cheaper, e.g. by reducing the amount of platinum and other expensive materials, and more efficient, while also being stable under the reaction conditions, selective for the desired reactions, and environmentally friendly. Therefore, knowledge of the active centers and the structure of the catalyst-electrolyte interface is of utmost importance for the design of new catalysts according to these goals [13].

Atomistic simulations can directly resolve interfacial structures under different conditions and are thus a versatile tool for the discovery of new catalysts [13]. In addition, the assessment of yet unstudied e.g. newly designed materials via computational screening is more efficient and faster than via experimental methods [14]. As an example, Nørskov and coworkers predicted the activity of different pristine metal surfaces for the oxygen reduction reaction from gas phase adsorption energies [15]. In this pioneering work, they introduced the computational hydrogen electrode by referencing the protons and electrons to the standard hydrogen electrode (SHE) potential, allowing them to directly link theoretical calculations to experimental results. For the hydrogen evolution reaction, they found a correlation between the adsorption energy of hydrogen with the experimentally measured exchange current density on different metal surfaces [16].

However, this early model is highly idealized: the effect of the solvent is (largely) omitted, as well as adsorption-induced work function change. Later additions to this model have recovered some of these effects like double-layer charging [17] or pH dependencies [18], but the current models are still far from the complexity of real systems [19]. In particular, studying the effects of the solvent is challenging because water on many interesting catalyst materials such as Pt(111) exhibits very slow dynamics, requiring long and exhaustive calculations to converge the results [20].

The central focus of this work is the detailed, atomistic study of the interface between water and metals, especially Pt(111). The mentioned slow dynamics are likely caused by a potential energy surface with high energetic barriers between minima and different phase space regions commonly referred to as super basins [21]. To speed up the sampling of different super basins, a global exploration of the phase space is desirable, which yields representative structures of the different regions. These structures could exhibit different geometries such as squares or hexagons. Water exhibits many of these motifs in 2D for different surface densities [22] or temperatures and lateral pressures, respectively [23]. Thus, a natural approach to represent interfacial water is via the use of 2D static water films. Historically, the hexagonal bilayer has been taken as a representative structure because its geometry is consistent with the (111) surface of fcc metals and experimental observations at low temperatures on these surfaces [24–26].

This approach was tested for the Pt(111)-water interface in the first publication of this thesis [27]. After placing water films on the metal substrate and performing a local geometry optimization, a diverse set of local minima structures with different water orientations and bonding geometries was obtained. The broad range of work functions and adsorption energies allowed us to analyze the sensitivity of this system to the precise arrangement of water, and the comparison to *ab initio* molecular dynamics simulations from Refs. [28, 29] revealed a structural bias. The static approach tends to form too many hydrogen bonds at the interface, as the prominent hexagonal layers were less similar than one-dimensional chains of water molecules to the reference data. Despite the bias in the static water layers, the approach could be useful for future studies, e.g. the assessment of kinetic barriers within different interfacial solvent structures.

The second part of this work focuses on a shortcoming of implicit solvation models, which represent water as a continuum and are hoped to capture the average interactions of the solvent with the solute [30]. The exclusion of water from a specific region, the formation of a cavity, is one energetic contribution of the solvation energy and can change drastically at solid-liquid interfaces [20, 31]. However, existing models are typically parameterized via bulk solvation energies and thus describe cavity formation as in the bulk solvent. Such parametrizations are unable to capture effects due to competitive adsorption which leads to a stabilization of adsorbates at solid-liquid interfaces since the energetic cost of removing interfacial water is underestimated [29, 32, 33]. Therefore, knowledge about the free energy of cavity formation at the metal-water interface is one of the key ingredients for improving implicit solvent models which motivated their assessment across a wide range of metallic, substrate materials in the second publication of this thesis [34]. One significant outcome of these studies was the possibility of rationalizing the observed substrate dependence with the adsorption energy of water, which emphasized the competitive nature of adsorption processes at these interfaces. Finally, we compared our result with the existing literature for bulk cavity formation [35–37] to check the convergence of our result as well as the adsorption of phenol to Pt(111), which is known to be affected by the competitive adsorption with water [32, 33, 38, 39]. We found very good agreement for both aspects, which demonstrates the predictive quality and importance of our results for understanding adsorption at solid-liquid interfaces. Our finding that competitive effects correlate well with adsorption energies of single solvent molecules might pave the way for an approximate but straightforward inclusion of such effects in future, improved implicit solvation models.

An overview of the theoretical concepts and methods used is given before summarizing the main results of the published papers.

2. Theoretical Background

2.1. Potential Energy Surface

A typical assumption made in atomistic simulations is the Born-Oppenheimer approximation (BOA) [40]. Since electrons are many times lighter than nuclei, the BOA assumes that electrons immediately adjust to changes in the position of nuclei, separating the degrees of freedom of electrons and nuclei. Therefore, the BOA allows the description of the potential energy $U(x)$ as a function of the nuclear coordinates x (hereafter called atomic positions). Furthermore, the electrons should adiabatically follow any change in the nuclei and remain in their respective ground states for a given set of atomic positions. The BOA is only valid if the different electronic states are separated. The resulting hypersurface $U(x)$ is called the potential energy surface (PES) and is $3N$ dimensional, where N is the number of atoms [40].

Typical points of interest on the PES are the minima, which are (meta)stable states, e.g. isomers of a molecule, and the saddle points, which are transition states connecting them.

Furthermore, the measurement of any property X at equilibrium $\langle X \rangle$ in classical statistical mechanics requires the evaluation of the PES as

$$\langle X \rangle = \int \int X(x,p) \underbrace{Q(N,V,T)^{-1} \exp\left(-\beta E_{\mathrm{tot}}(x,p)\right)}_{P(x,p)} dx\, dp, \tag{2.1}$$

where $Q(N,V,T)$ is the canonical partition function, β is $(k_{\mathrm{B}}T)^{-1}$, x and p are the atomic positions and momenta, $E_{\mathrm{tot}}(x,p)$ is the total energy of a state in phase space, and $P(x,p)$ is its probability. Within the canonical ensemble the number of particles N, the volume V, and the temperature T of a system are fixed. The canonical ensemble describes closed systems that do not exchange particles with the environment or change their volume and are embedded in a heat bath at a fixed temperature. Unless otherwise stated, this is the ensemble of interest in the present work. The corresponding partition function can be rewritten as

$$\begin{aligned} Q(N,V,T) &= \frac{1}{N! h^{3N}} \int \int \exp\left(-\beta E_{\mathrm{tot}}(x,p)\right) dx\, dp & (2.2)\\ &= \frac{1}{\Lambda^{3N} N!} \underbrace{\int \exp\left(-\beta U(x)\right) dx}_{Z(N,V,T)}, & (2.3) \end{aligned}$$

such that one part depends only on the potential energy U / the PES, called the configurational integral $Z(N,V,T)$, and the other part contains all contributions related to the kinetic energy, where h is the Planck's constant and Λ the temperature-dependent de Broglie wavelength [41]. Furthermore, the integration over dp is also analytically possible for the probability, which gives

$$P(x) = Z(N,V,T)^{-1} \cdot \exp\left[-\beta U(x)\right]. \tag{2.4}$$

Eq. 2.4 relates the potential energy of a given set of atomic positions to its probability/importance in the canonical ensemble. Since states with low potential energies have the highest probabilities according to Eq. 2.4, they contribute the most to the average ensemble value in Eq. 2.1. The global minimum represents the most stable state of the system at $0\,\mathrm{K}$ and is therefore of particular importance [40]. An example of a two-dimensional PES with two minima and a transition state between them is shown in Fig. 1.

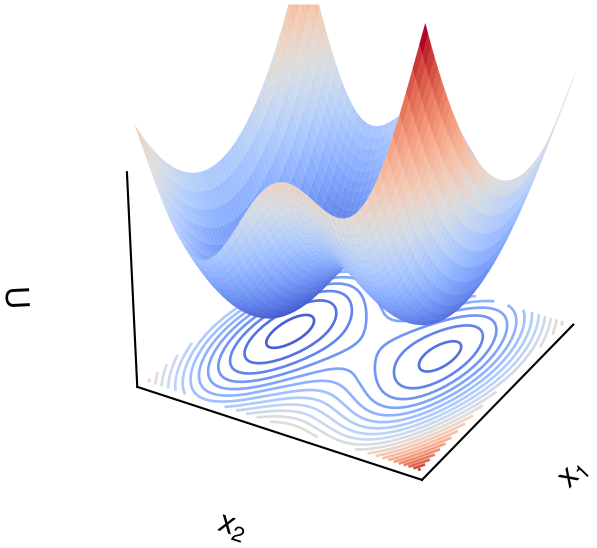

Figure 1 An example of a two-dimensional potential energy surface:
$U = (1.5x_1)^2 + x_1/2 + x_1 y_2 + (1.5x_2)^2 + \cos(1.5\pi x_2) + x_2/2 - 0.5.$

Obtaining the appropriate probabilities $P(x)$ of individual states necessitates performing the integral in Eq. 2.4 over the whole PES. This can be done e.g. numerically on a grid, as done in Fig. 1. However, such a direct method is only possible for very small systems such as an isolated water molecule [42], since the number of grid points scales exponentially with N. Similarly, restricting the search to all minima is not feasible either, since the number of minima on a PES is estimated to grow exponentially with N [21, 43]. Therefore, many different techniques such as molecular dynamics (MD), as discussed in section 2.4, have been developed to only sample regions of high probability according to Eq. 2.4.

Finally, there are two common ways to calculate the potential energy given the atomic positions: 1. quantum mechanics and 2. molecular mechanics. In quantum mechanics, the system of interest is described at the subatomic level with nuclei and electrons, and the calculation of the potential energy requires the determination of the electronic structure. Density functional theory (DFT) belongs to this category and is discussed in the following section.

Molecular mechanics instead treats the system as a collection of classical particles, e.g. without explicitly considering the electronic degrees of freedom. The interactions between the particles are described by effective potentials, which in the simplest case are analytical functions like a harmonic spring between spheres. The parameters required for this model are obtained from experimental or theoretical data. These models are also called force fields (FF) [40].

2.2. Density Functional Theory

The core of all quantum mechanical calculations is the Schrödinger equation [40, 44], which in its time-independent form can be written as

$$H\Psi = E\Psi. \tag{2.5}$$

Eq. 2.5 is an eigenvalue problem with the Hamiltonian H, a wave function Ψ as eigenvector and the energy E as eigenvalue. The Hamiltonian consists of five different contributions

$$H = T_e + \underbrace{T_n}_{0} + V_{ne} + V_{ee} + \underbrace{V_{nn}}_{\text{constant}} \tag{2.6}$$

which include the kinetic energy T of the electrons e and the nuclei n, the attraction between nuclei and electrons V_{ne}, and the repulsion between electrons V_{ee} and nuclei V_{nn}. The brackets in Eq. 2.6 are the results of the BOA. The kinetic energy of the nuclei T_n is neglected and set to zero, and the nuclei-nuclei interaction V_{nn} is constant for a set of fixed atomic positions. As a result, in the BOA the atomic positions enter the Schrödinger equation as fixed parameters and the eigenvalue problem is solved for the degrees of freedom of the electrons. However, exact analytical solutions are only possible for very few systems, so further simplifications are needed to find approximate solutions. Treating the electrons as independent particles interacting with the average potential created by all other electrons yields an eigenvalue problem that can be solved numerically. However, since the average potential depends on the solution, this approach requires an iterative procedure to make the solutions self-consistent, called self-consistent field method [40, 44].

As Hohenberg and Kohn showed [45], all electronic ground state properties can be expressed as a function of the ground state electron density $\rho\left(x\right)$, thus circumventing the need to solve the many-body problem using many-body wavefunctions. Furthermore, the ground state electron density can be obtained by minimizing an energy functional $E\left[\rho\right]$. In contrast to the electronic many-particle wavefunction $\Psi\left(x_1, x_2, ...\right)$, which depends on the $3N_e$ spatial coordinates of the N_e electrons, the electron density $\rho\left(x\right)$ is simply a function in the 3 spatial coordinates, which leads to a significant simplification (dimensionality reduction) of the problem.

However, an exact expression for the density functional $E\left[\rho\right]$ is unknown. Approaches that build on this original idea and rely only on a density functional $E\left[\rho\right]$ are typically referred to today as orbital-free DFT approaches. Unfortunately, most orbital-free DFT functionals known today exhibit significant errors [44]. However, significant improvements in accuracy, and thus the widespread adoption of DFT, was made possible by the reformulation of the DFT approach by Kohn and Sham [46].

Kohn and Sham introduced the concept of an (artificial) reference system of non-interacting electrons, which yields the same electron density as the real, interacting one. In the non-interacting case, it is possible to express the many-particle wavefunction as a product of single-particle wavefunctions, for which the kinetic energy and the electron-electron repulsion can be calculated straightforwardly. In Kohn-Sham DFT, the total energy is given by the sum of four functionals of the electron density

$$E\left[\rho\right] = T_S\left[\rho\right] + E_{ne}\left[\rho\right] + J\left[\rho\right] + E_{xc}\left[\rho\right], \tag{2.7}$$

where T_S is the kinetic energy of the reference system, E_{ne} and J are the classical Coulomb potentials for the nuclear-electron and electron-electron interactions, respectively. The energy difference to the real system is summed up in the so-called exchange-correlation functional E_{xc}. It includes the difference in kinetic energy between the non-interacting and the real system, and the aforementioned exchange and correlation contribution due to the quantum-mechanical nature of the interacting electrons. Finally, contributions due to self-interaction within the electron density would also be accounted for, if the 'true' E_{xc} functional were known. This advantage comes at the cost of reintroducing wave functions into DFT. The resulting one-electron Hamiltonian in Kohn-Sham DFT is as follows

$$h_i^{\mathrm{KS}} = -\frac{1}{2}\nabla_i^2 - \sum_k^{\mathrm{nuclei}} \frac{Z_k}{|x_i - x_k|} + \int \frac{\rho\left(x'\right)}{|x_i - x'|}dx' + V_{xc}. \tag{2.8}$$

Since the electrons do not interact, the total Hamiltonian is the sum of the one-electron operators from Eq. 2.8 as

$$\sum_{i=1}^{N} h_i^{\mathrm{KS}}|\chi_1\chi_2\ldots\chi_N\rangle = \sum_{i=1}^{N}\epsilon_i|\chi_1\chi_2\ldots\chi_N\rangle \tag{2.9}$$

with the wavefunction $|\chi_1\chi_2\ldots\chi_N\rangle$ consisting of one-electron orbitals χ_i. Since the expression of the first three contributions is fixed and exact, the improvement of Kohn-Sham DFT relies on finding E_{xc} to correct for the mentioned shortcomings. As a first step, E_{xc} is expressed as a function of the local density, and the individual contributions are summed up, hence the correction is called the local density approximation (LDA). The exchange energy for the uniform electron gas is analytically known and can be used for this purpose. The corrections for the other contributions are more complicated and the expressions are fitted to known references. LDA works well for systems with a fairly uniform electron density, such as metals, but gives poor results for systems with strongly varying electron densities, such as molecules [44]. Including the local gradient of the electron density in E_{xc} yields the generalized gradient approximation (GGA), which improves the performance of DFT for these systems. More sophisticated corrections involve the curvature (meta-generalized gradient) or mix in contributions from wavefunction methods such as Hartree-Fock (hybrid) [40, 44].

2.3. Force Fields

Instead of solving the complicated eigenvalue problem to obtain the potential energy as a function of nuclear coordinates described in the previous section, FFs have a fixed functional form which, in the simplest case, takes the atomic positions as input to yield a potential energy [40]. A classic example is the well-known Lennard-Jones potential (LJ)

$$U_{\mathrm{LJ}}\left(r\right) = 4\epsilon\left[\left(\frac{\sigma}{r}\right)^{12} - \left(\frac{\sigma}{r}\right)^{6}\right], \tag{2.10}$$

which describes the energy as a function of the distance r between two atoms. It is therefore a pair potential and has two free parameters: the potential well depth ϵ and the distance σ, at which the potential is zero. U_{LJ} exhibits a minimum at $2^{1/6}\sigma$, commonly referred to as r_0. Numerical values for these parameters are usually determined by experimental or theoretical data for all atomic species in a calculation and serve purpose for only a specific system. The total potential energy is the sum of the partial energies of all atoms. Since the LJ potential has a simple analytical form, the forces acting on each atom are simply obtained as the derivative of the energy with respect to the distance r. The choice of an appropriate FF for the system of interest is crucial since they can only capture effects that are described by explicit terms. Common choices are harmonic potentials for covalent bonds or angles between three atoms that force them to oscillate around their equilibrium value. The topology information, which atoms are bonded or form such an angle, must also be specified. Similarly, charges can be assigned to atoms as point charges and the electrostatic interactions can be calculated via the Coulomb potential [40]. Consequently, there is a wide variety of classical FF in the literature, most of which are intended for a specific type of system. For example, the embedded atom method, which includes a term for the dislocated electrons of conductors, has proven useful for simulating metals, whereas FF describing explicit bonds are typically used to describe organic matter such as proteins [47]. Alternatively, machine-learned interatomic potentials can predict energies and forces without also solving the Schrödinger equation, which has the advantage over classical FF of not requiring an assigned functional form. Therefore, machine-learned interatomic potentials can capture a wide variety of interactions. However, the construction/parametrization of such machine-learned interatomic potentials needs a considerable amount of reference data to determine (learn) their more complex functional form and thus arrive at accurate predictions [48].

2.4. Molecular Dynamics

As mentioned in the previous section 2.1, a brute force approach to evaluate the full PES is only possible for extremely simple systems [49]. In addition, many states have negligible probabilities and thus their contribution to any averaged quantity is also negligible. Since low energy states have the highest probabilities according to Eq. 2.1, sampling these regions, typically around the low-lying minima, should yield accurate averages. Exploring this relevant region of phase space by following the temporal evolution of the system is the basic idea of molecular dynamics (MD) [49]. The most straightforward application of MD is within the microcanonical ensemble, where the time evolution of a closed system is simulated by numerically integrating Newton's equations of motion for a finite, chosen timestep Δt. The available integration techniques are best understood by considering Taylor expansions of atomic positions $\vec{x}$ and velocities $\vec{v}$.

$$\vec{x}\left(t+\Delta t\right)=\vec{x}\left(t\right)+\frac{d\vec{x}\left(t\right)}{dt}\Delta t+\frac{1}{2!}\frac{d^2\vec{x}\left(t\right)}{d^2t}\Delta t^2+\frac{1}{3!}\frac{d^3\vec{x}\left(t\right)}{d^3t}\Delta t^3+\dots \tag{2.11}$$

$$\vec{v}\left(t+\Delta t\right)=\vec{v}\left(t\right)+\frac{d\vec{v}\left(t\right)}{dt}\Delta t+\frac{1}{2!}\frac{d^2\vec{v}\left(t\right)}{d^2t}\Delta t^2+\frac{1}{3!}\frac{d^3\vec{v}\left(t\right)}{d^3t}\Delta t^3+\dots. \tag{2.12}$$

The first-order velocity term is Newton's second law of motion $\vec{F}=m\cdot\vec{a}=m\cdot d\vec{v}\left(t\right)/dt$ and shows that MDs require the calculation of forces $\vec{F}$. Using this expression and truncating the expansion after the first order term, one obtains the so-called Euler algorithm

$$\vec{x}\left(t+\Delta t\right)=\vec{x}\left(t\right)+\vec{v}\left(t\right)\cdot\Delta t+O\left(\Delta t^2\right) \tag{2.13}$$

$$\vec{v}\left(t+\Delta t\right)=\vec{v}\left(t\right)+\frac{\vec{F}\left(t\right)}{m}\cdot\Delta t+O\left(\Delta t^2\right). \tag{2.14}$$

The Euler algorithm is simple but requires very small timesteps for simulations since the error scales with the square of the timestep $O\left(\Delta t^2\right)$. A more stable algorithm, which also demands only one force evaluation, is the Störmer-Verlet time integration [50]. Several schemes of this algorithm exist, but the most popular is the so-called Velocity-Verlet algorithm implemented in the *Large-scale Atomic/Molecular Massively Parallel Simulator* (LAMMPS) [51]. The algorithm introduces a half-step in Eq. 2.13:

1. $\vec{v}\left(t+\frac{\Delta t}{2}\right)=\vec{v}\left(t\right)+\frac{\vec{F}\left(t\right)}{m}\cdot\frac{\Delta t}{2}$
2. $\vec{x}\left(t+\Delta t\right)=\vec{x}\left(t\right)+\vec{v}\left(t+\frac{\Delta t}{2}\right)\cdot\Delta t$
3. $\vec{v}\left(t+\Delta t\right)=\vec{v}\left(t+\frac{\Delta t}{2}\right)+\frac{\vec{F}\left(t+\Delta t\right)}{m}\cdot\frac{\Delta t}{2}.$

First, the velocities are updated by half of the timestep $t+\frac{\Delta t}{2}$ with the force at time t. In the second step, the positions are propagated with the half-step velocity and finally, the velocities are updated again with the new positions, so that at the end of each iteration the positions and velocities are in phase. In addition, the algorithm has other advantages, it is fully time-reversible and energy-conserving for rather large timesteps, even though the error scales with $O\left(\Delta t^2\right)$ as well [52].

MD simulations can be run in different ensembles with their constraints for energy, volume, temperature, or pressure, among others. The corresponding ensembles are the microcanonical (NVE), the canonical (NVT), or the isothermal-isobaric (NPT) ensemble. A microcanonical MD using the same example PES is shown in Fig. 2. The total energy is fixed so that the energy is transformed from potential to kinetic energy and vice versa. The simulation samples the environment of a minimum and is similar in this respect to a marble in a bowl without friction.

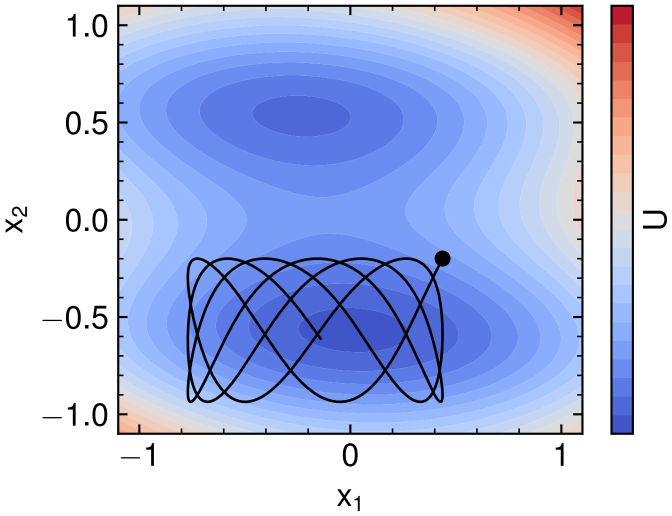

Figure 2 A microcanonical (NVE) MD on the example PES from Fig. 1. The dot marks the initial position and the initial velocity is set to zero.

Simulating the other ensembles, such as the canonical ensemble, is more difficult because it requires a controlled temperature rather than just fixing the total energy. For the latter, the relationship between temperature and velocity via the equipartition theorem is used:

$$\frac{1}{2}m\langle v^2\rangle = \frac{n}{2}\cdot Nk_BT \rightarrow T = \frac{m\langle v^2\rangle}{n\cdot Nk_B}, \tag{2.15}$$

where n is the number of translational degrees of freedom. Furthermore, the velocities in a canonical ensemble should follow the Maxwell-Boltzmann distribution as

$$P\left(v\right) = \left(\frac{\beta}{2\pi m}\right)^{1.5} \exp\left(-\beta\frac{mv^2}{2}\right), \tag{2.16}$$

so that for a finite system the temperature in the canonical ensemble fluctuates around the set value. The simple approach of applying Eq. 2.15 by multiplying all velocities by a factor so that the temperature remains constant is called the Berendsen thermostat [53]. However, such a 'simple' rescaling approach does not sample the canonical ensemble [49]. Instead, a common thermostat to properly sample the canonical ensemble is the Nosé-Hoover thermostat [54, 55], which couples the atomistic system to a virtual heat bath of the specified temperature. This modifies the equations of motion by introducing a friction coefficient ξ, which also evolves with time. The equations then become

$$\dot{x} = v \tag{2.17}$$

$$\dot{v} = F/m - \xi v \tag{2.18}$$

$$\dot{\xi} = \left(\sum_i m_i v_i^2 - \frac{3N}{\beta}\right)/Q, \tag{2.19}$$

where the dot above the variables denotes their time derivative and Q is the coupling parameter to the heat bath. It is important to note, that a single Nosé-Hoover thermostat will fail under certain conditions, such as in systems with more than one conserved quantity [49, 52]. However, using a chain of such thermostats acting on each other has been shown to sample the canonical ensemble accurately even in these cases [56]. Finally, a trajectory that correctly samples the specified ensemble should yield accurate time-averaged quantities such as

$$\langle X\rangle_t = \frac{1}{M}\sum_i^M X\left(t_i\right). \tag{2.20}$$

The equivalence of the time $\langle X\rangle_t$ and the ensemble mean $\langle X\rangle$ is called the ergodic hypothesis and implies that the system can explore the entire relevant phase space. Since MD simulations evolve the system in time, samples with a small time difference are correlated. Therefore, the averages in Eq. 2.20 will be biased if the trajectory is not long enough to decorrelate the samples. The necessary steps for the decorrelation of samples depend on the property of interest and need to be verified, e.g. by running several independent simulations and comparing the resulting averages [49].

2.5. Free Energy Surface

Similar to the calculation of average quantities (cf. Eq. 2.1), the absolute free energy F of a system [41, 49] necessitates the computation of the partition function

$$F = -\beta^{-1} \cdot \ln\, Q\left(N, V, T\right). \tag{2.21}$$

Again, evaluating the entire phase space is impossible except for simple model systems, thus making $Q\left(N, V, T\right)$ inaccessible. Similarly, the absolute free energy is not measurable in experiments unlike free energy differences ΔF. In that regard, the free energy difference between state A and B is

$$\Delta F = F_\mathrm{A} - F_\mathrm{B} = -\beta^{-1} \cdot \ln\left(\frac{Q_\mathrm{A}}{Q_\mathrm{B}}\right) = -\beta^{-1} \cdot \ln\,\left(\frac{Z_\mathrm{A}}{Z_\mathrm{B}}\right), \tag{2.22}$$

where the configurational integrals Z_A and Z_B demand sampling of the relevant phase space of state A and B, respectively. These are as well connected to the probability of the respective states as discussed in sec 2.4. If both states can be separated by a variable z, the probability P of state A is

$$P_\mathrm{A} = C^{-1} \int\int \exp\left(-\beta E_\mathrm{tot}\left(x, p\right)\right) \delta\left(z - z_\mathrm{A}\right) dx\; dp = C^{-1} Q_\mathrm{A}, \tag{2.23}$$

where C is a normalization constant and the PES is only evaluated in the space space volume of state A through the δ-function. Combining Eq. 2.22 and Eq. 2.23 yields a direct approach to calculate a free energy surface (FES) as a histogram of z:

$$\Delta F = F_\mathrm{A} - F_\mathrm{B} = -\beta^{-1} \cdot \ln\,\left(\frac{P_\mathrm{A}}{P_\mathrm{B}}\right) \rightarrow \Delta F\left(\{z\}\right) = -\beta^{-1} \cdot \ln\left[P\left(\{z\}\right)\right]. \tag{2.24}$$

From Eq. 2.24 is is evident that the PES and the FES $\Delta F\left(\{z\}\right)$ have two major differences:

1. The number of dimensions of the PES involve all atoms ($3N$), whereas the dimensions of an FES depend on the so-called collective variable (CV) or order parameter $(\{z\})$. FESs have in general a lower dimensionality than the PES.
2. The PES is in principle unique for a chosen system and methodology to calculate the energy. In contrast, there are infinitely many FESs for the same system.

Therefore, the quality of an FES depends crucially on the chosen CV. An ideal CV should separate the states of interest and has as few dimensions as possible. To this end, all degrees of freedom, which are not important to describe a process/transformation should be integrated out, leaving only the CV. As an example, the same PES from the previous sections is plotted in Fig. 3 with two possible CVs (x_1, x_2). Evidently, x_1 is not a suitable choice to discriminate between the two wells, while taking x_2 as CV yields an FES with the two wells.

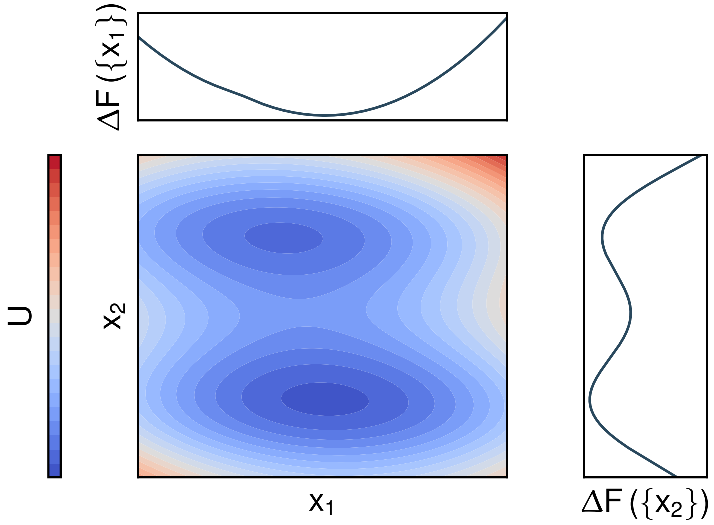

Figure 3 The exemplary PES from Fig. 1 with two possible FESs using x_1 and x_2 as CVs and Eq. 2.24.

A more application oriented example is the folding of a protein in water [57]. The degrees of freedom of the water molecules are not of interest, but, e.g. the distance between two protein chains, which are not bound to each other and in close proximity in the folded state. Hence, this distance could be a suitable descriptor to separate the unfolded and folded state. Many different configurations are then mapped to the same CV, hence the dimensionality is reduced and the process can be understood in one dimension. The CV does not have to be a combination of Cartesian coordinates, but can also be the charge or the coordination number [58]. In addition to these considerations about CVs, Eq. 2.24 states that free energy differences can be calculated from MDs by recording the value of the CV. For an ergodic system, which means that the whole phase space is accessible, an infinitely long MD simulation should yield an accurate FES. In reality, an MD run might be trapped in a minimum or a region in phase space as shown in Fig. 2. This will naturally bias the FES and exemplifies that this approach is only feasible for systems without e.g. large energetic differences between states and barriers. Any such bottleneck limits the sampling of the relevant phase space and leads to errors. For these cases, more complex methods have been developed to overcome these bottlenecks and access the free energy difference [41, 49]. One of these methods is free energy perturbation (FEP), which will be explained in detail in the following section and was used in the second publication [34] of this thesis.

2.6. Free Energy Perturbation

The basic idea of free energy perturbation (FEP) can be derived from Eq. 2.22 [41, 49]. Both states are described by their own Hamiltonians and the energy difference for a given set of configurations $\Delta U\left(x\right)$ of both Hamiltonians is used to calculate the free energy difference. This approach allows the alchemical transformation of atoms or the restriction of the system to a certain part of the phase space, e.g. by fixing the value of the CV and changing it over different runs [59]. The latter is particularly useful for driving the system into regions that are rarely sampled in an unconstrained MD simulation. The free energy difference can then be obtained via Eq. 2.28, the so-called Zwanziger equation [60]. It is obtained from Eq. 2.22 by multiplying with $\exp\left[-\beta U_{\mathrm{B}}\left(x\right)\right]\cdot\exp\left[\beta U_{\mathrm{B}}\left(x\right)\right]$:

$$\begin{aligned}\Delta F = F_{\mathrm{A}} - F_{\mathrm{B}} &= -\beta^{-1}\cdot\ln\left(\frac{Z_{\mathrm{A}}}{Z_{\mathrm{B}}}\right) &(2.25)\\ &= -\beta^{-1}\cdot\ln\frac{\int\exp\left[-\beta U_{\mathrm{A}}\left(x\right)\right]dx}{\int\exp\left[-\beta U_{\mathrm{B}}\left(x\right)\right]dx} &(2.26)\\ &= -\beta^{-1}\cdot\ln\int P_{\mathrm{B}}\left(x\right)\exp\left(-\beta\left[U_{\mathrm{A}}\left(x\right)-U_{\mathrm{B}}\left(x\right)\right]\right)dx &(2.27)\\ &= -\beta^{-1}\cdot\ln\left\langle\exp\left(-\beta\left[U_{\mathrm{A}}\left(x\right)-U_{\mathrm{B}}\left(x\right)\right]\right)\right\rangle_{\mathrm{B}}. &(2.28)\end{aligned}$$

In principle, only state B needs to be sampled and, subsequently, the free energy difference is extrapolated by calculating the potential energy difference between state A and B. This method works if state A and B overlap/are close in the phase space. For further separated states, the path between them can be divided into several smaller steps and Eq. 2.28 applied to all neighboring ones to go from A to B or vice versa. Unfortunately, this simple approach is prone to statistical errors, since only the overlap of two states is used and only in one direction. A better scheme would employ the difference between several states and using the overlap in both directions. This issue was addressed by Bennet [61] and further refined by Shirts [62]. Starting from the identity in Eq. 2.29, Bennet introduced a weighting $w\left(x\right)$ to the forward and backward integration

$$\begin{aligned}\frac{Q_{\mathrm{A}}}{Q_{\mathrm{B}}} &= \frac{Q_{\mathrm{A}}}{Q_{\mathrm{B}}}\cdot\frac{\int w\left(x\right)\cdot\exp\left[-\beta U_{\mathrm{A}}\left(x\right)\right]\cdot\exp\left[-\beta U_{\mathrm{B}}\left(x\right)\right]dx}{\int w\left(x\right)\cdot\exp\left[-\beta U_{\mathrm{A}}\left(x\right)\right]\cdot\exp\left[-\beta U_{\mathrm{B}}\left(x\right)\right]dx} &(2.29)\\ \Delta F &= -\beta^{-1}\cdot\ln\frac{\left\langle w\left(x\right)\cdot\exp\left[-\beta U_{\mathrm{A}}\left(x\right)\right]\right\rangle_{\mathrm{B}}}{\left\langle w\left(x\right)\cdot\exp\left[-\beta U_{\mathrm{B}}\left(x\right)\right]\right\rangle_{\mathrm{A}}}. &(2.30)\end{aligned}$$

Eq. 2.30 is valid for any choice of $w\left(x\right)$, but Bennet found the optimal choice, which minimizes the estimated statistical error in the free energy difference $\sigma_{\Delta F}$, to be

$$w\left(x\right) = \frac{K}{\left(Q_{\mathrm{A}}/N_{\mathrm{A}}\right)\exp\left[-\beta U_{\mathrm{B}}\left(x\right)\right]+\left(Q_{\mathrm{B}}/N_{\mathrm{B}}\right)\exp\left[-\beta U_{\mathrm{A}}\left(x\right)\right]}, \tag{2.31}$$

where K is a constant and N the number of (uncorrelated) samples from state A and B. Combining Eq. 2.31 and Eq. 2.30 yields the common expression of the Bennett Acceptance Ratio (BAR) method [61] as

$$\Delta F = -\beta^{-1} \cdot \ln \left[\frac{\langle \{1 + \exp\left(\beta\left[U_{\mathrm{A}}\left(x\right) - U_{\mathrm{B}}\left(x\right) + C\right]\right)\}^{-1} \rangle_{\mathrm{B}}}{\langle \{1 + \exp\left(\beta\left[U_{\mathrm{B}}\left(x\right) - U_{\mathrm{A}}\left(x\right) - C\right]\right)\}^{-1} \rangle_{\mathrm{A}}} \cdot \exp\left(\beta C\right) \right], \tag{2.32}$$

with $C = -\Delta F + \beta^{-1} \cdot \ln\left(N_B / N_A\right)$ in case of the optimal choice. Since the ratio ΔF is on both sides of Eq. 2.32, this equation must be solved self-consistently for ΔF. BAR was generalized to the free energy difference of multiple states by Shirts and Chodera into the Multistate Bennet Acceptance Ratio (MBAR) method [62]. Multistate free energy differences are calculated between all sampled states and not only for neighbouring states. This leads to a set of equations, which need to be solved self-consistently and reads as

$$F_i = -\beta^{-1} \ln \sum_{k=1}^{K} \sum_{n=1}^{N_k} \frac{\exp\left[-\beta U_i\left(x_{kn}\right)\right]}{\sum_{k'=1}^{K} N_k' \exp\left[\beta F_{k'} - \beta U_{k'}\left(x_{kn}\right)\right]}, \tag{2.33}$$

where the first and third sums run over the K states of interest and the second sum over the number of samples N_k in state k. The free energy F_i is only determined up to an additive constant, such that only free energy differences ΔF are meaningful. Similar to the Zwanziger Equation, MBAR can estimate the free energy difference to states, which were not explicitly sampled. For this purpose, N_k of the unsampled state is set to zero and this procedure is especially useful to e.g. interpolate between points to generate a smooth free energy profile [62]. Analogous to the weightings from Eq. 2.31, MBAR determines weightings/probabilities for all configurations in each state, which can be used to calculate expectation values (cf. Eq. 2.1) from all sampled configurations. This is useful to remove the bias introduced in MDs to sample free energies or monitor the change of a property with respect to the CV [63].

As an example, FEP with MBAR was applied to the exemplary PES in Fig. 4. Eleven evenly spaced values x_2 were fixed and a canonical ensemble was generated. For each ensemble six uncorrelated samples were drawn, which are marked with crosses in the left panel of Fig. 4. Afterwards, all configurations were evaluated in each of the eleven ensembles by adjusting x_2 to the respective position. These energies were finally used to run MBAR with the software package pymbar [62]. The resulting free energy profile is plotted on the right side of Fig. 4. In addition, the free energy surface from the grid evaluation of the PES is plotted as well. Since both curves are largely the same, MBAR has successfully predicted the FES.

Furthermore, MBAR can integrate over several CVs at the same time. For the investigation of cavities at solid-liquid interfaces (SLIs) in Ref. [34], we calculated the free energy differences between states with a different cavity position and size at the same time, which resulted in a well converged free energy profile. Another important advantage of BAR and MBAR is the direct calculation of the statistical error of the obtained free energy with MBAR being the best estimator for free energy differences [64]. To this end, the disadvantage of MBAR is the costly

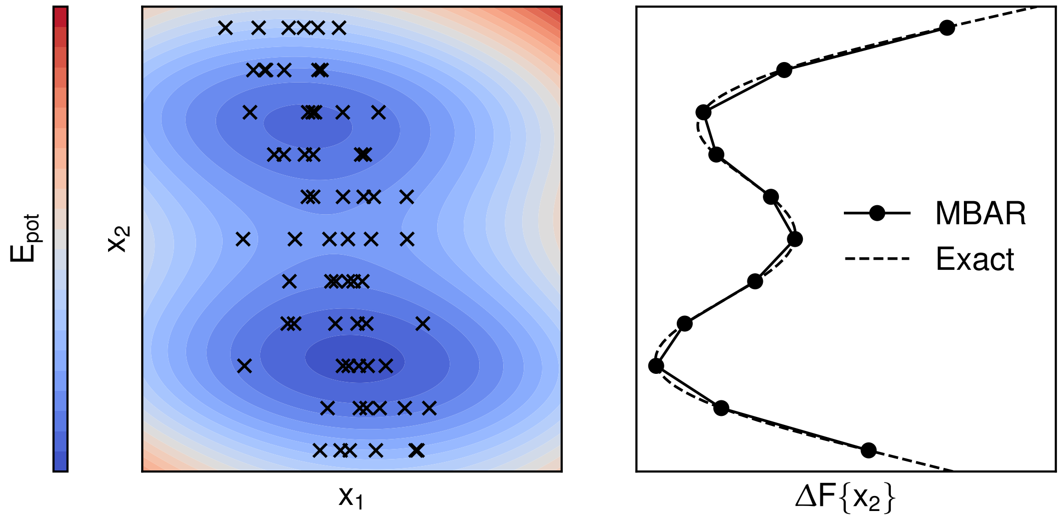

Figure 4 FES using x_2 as CV using Eq. 2.24 (Exact) and FEP via Eq. 2.33 with pymbar [62]. Eleven independent, canonical ensembles were generated at evenly spaced values of x_2 for the calculation with MBAR. The crosses in the left panel mark the location of the samples.

post-processing, if many samples in different states need to be evaluated, such that solving Eq. 2.33 becomes very memory intensive [63]

3. Metal-Water Interfaces in Electrochemistry

3.1. Overview

Metal-water interfaces are present in many electrochemical devices like fuel cells and electrolyzers, which are prominent solutions for the global energy storage and conversion challenges [1, 4, 6, 65]. The schematic setup of a fuel cell, which generates electricity from the reaction of hydrogen and oxygen is shown in Fig. 5. A fuel cell consists of two half-cells with the electrode and the electrolyte as well as an electron conductor and an ion conductor, which is typically a polymer membrane in modern fuel cells/electrolyzers operating at low temperatures. At the anode, the oxidation reaction takes place, and at the cathode, the reduction reaction, which is the hydrogen oxidation and the oxygen reduction reaction, respectively. In an electrolyzer, the reactions and flows are reverted by applying the opposite potential [65].

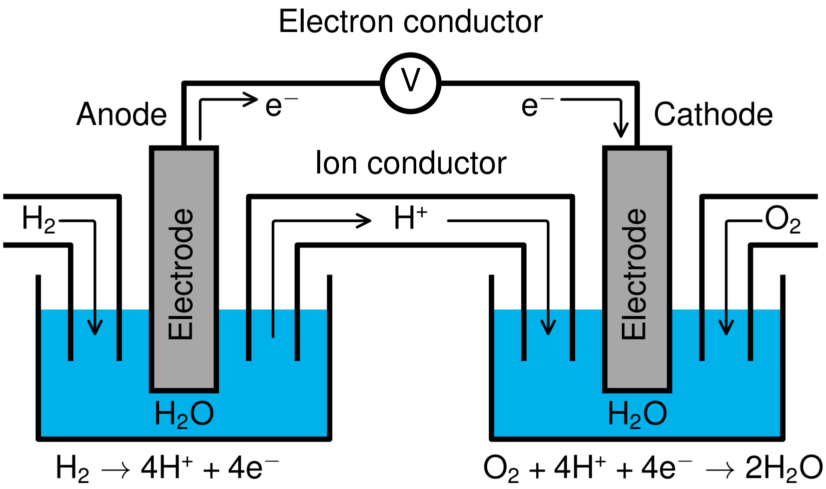

Figure 5 Schematics of a fuel cell for the conversion of hydrogen and oxygen gas to water.

The driving force for the reaction is the overpotential, which is the difference to the equilibrium potential of the reaction and is lost as heat during operation. The magnitude of this overpotential depends on the electrodes. During the reactions shown in Fig. 5 the reactants adsorb on the surface and are converted stepwise to the final product, which desorbs from the surface. A potential has to be applied, such that the free energy change of all steps becomes negative and thus the reaction runs spontaneously [65]. As demonstrated by Nørskov and coworkers, this concept allows for the prediction of catalyst activities from free energy diagrams [15]. In addition, the catalyst governs the kinetics of the reactions. Following the Sabatier principle, the binding strength of the catalyst has to be strong enough to prevent the desorption of the reactants and intermediates before the reaction takes place. However, the products are not desorbing if the binding is too strong, which blocks the catalyst for other reactants [65].

For the hydrogen evolution reaction, Nørskov and coworkers found the relation between theoretical binding strength and experimentally measured exchange current density for pure metal catalysts [16], which exemplifies the utility of theoretical predictions for the development and understanding of catalysts. For both the hydrogen oxidation and oxygen reduction reaction platinum-based catalysts are employed in current fuel-cells since they compromise low overpotentials with comparably fast kinetics [6, 11–13, 66]. However, the low abundance of platinum and the associated costs limit its applicability [4]. Better catalysts would consist of cheap and abundant materials, are stable during operation, and be selective towards the desired reaction while maintaining/enhancing the efficiency and kinetics of the current ones. To systematically optimize catalysts following these targets, it is necessary to identify the active center of the catalyst under reaction conditions [13]. The above-mentioned predictions on the hydrogen evolution reaction were based on adsorption energies in the gas phase without modelling the electrolyte. However, the omission of the electrolyte can alter the energetics tremendously [38]. Therefore, atomistic simulations of the SLI are an important tool to unravel the detailed structure and hence aid the development of new catalysts. Currently, though, most theoretical studies are focused on well-defined test systems like the Pt(111)-water interface [67] because of the high computational cost of accurate first-principles calculations. The interfaces in commercially available fuel cells are way more complex as the catalysts are nanoparticles with different facets, edges, kinks, and defects, while the electrolyte contains salts and other additives [19]. Therefore, the transfer of knowledge from the model systems to real systems is a huge challenge in molecular modeling, which necessitates coarse-graining to reduce the computational costs [68]. To this end, coarse-grained models for water, e.g. implicit solvation or static water models, enable the scanning of many catalyst materials and sites, which allows for the modelling of more complex systems and aids the discovery of new catalysts [30].

3.2. Atomistic Simulations of Metal-Water Interfaces

Despite its simple molecular formula, water exhibits a variety of anomalous properties. An everyday example is the particularly high surface tension and the density anomaly of water which makes ice float on liquid water. Such behaviors originate to a large extent from the interplay of the two intermolecular forces: Van der Waals interaction and hydrogen bonding [69, 70]. Van der Waals forces occur through fluctuations in the electron density and lead to an interaction modeled by the LJ potential. The hydrogen bonding of water results from the polar, covalent bond between oxygen and hydrogen. The positively charged hydrogen interacts with a lone pair of the negatively charged oxygen of another water molecule. In the simplest case, this interaction is approximated as an electrostatic interaction with no charge transfer [70], which is described by the Coulomb interaction of fixed partial charges. The classical FF model of water [71] used in the second publication of this thesis [34] describes the interactions in exactly this manner and can predict many properties such as the density with a reasonable accuracy [72].

The hydrogen bond formation is the dominating factor for the structuring of water and leads to the preferred tetrahedral arrangement of water. Expressed as the Bernal-Fowler rules, the oxygen in ice phases should be fourfold coordinated by other oxygens, while only one hydrogen should link two oxygens forming a hydrogen bond [73, 74]. However, there are many possibilities in the overall ordering of water and its phase diagram contains many of them [74]. While a variety of most stable phases and coexistence lines between multiple phases for the specified conditions (here: temperature and pressure) at equilibrium is known, several theoretically predicted phases have not yet been observed [75].

This complexity of the water structure is equally present in two-dimensional systems. Here, the diversity of structural motifs spans many different polygons like squares, pentagons, or hexagons [22, 23]. In contrast to bulk water, where all water molecules donate two hydrogen bonds and accept two according to the Bernal-Fowler rules [73], these numbers vary in two dimensions. In a hexagonal lattice, each water molecule forms three hydrogen bonds (2 acceptors and 1 donor / 1 acceptor and 2 donors). This hexagonal arrangement is commensurate with the (111) surface of fcc metals and was also observed in low-temperature experiments making it a model for these systems [24–26]. Because of the presence of water in e.g. low-temperature fuel cells and electrolyzers or heterogeneous catalysis at metal-water interfaces, knowledge about the structuring of interfacial water is of fundamental interest, as any adsorbate or intermediate will interact with water as the solvent. Therefore, the energetics of static water layers can be considered a baseline for any further calculations, e.g. at metal-water interfaces. Two key properties, which can be accessed from atomistic simulations of metal-water interfaces, are adsorption energies E_ads and work functions Φ. The former is a measure of the binding strength of the metal surface to one or multiple adsorbates and in the case of adsorbing water is calculated as

$$E_\mathrm{ads} = \frac{1}{N_\mathrm{H_2O}} \left[E_\mathrm{slab|H_2O} - \left(E_\mathrm{slab} + N_\mathrm{H_2O} \cdot E_\mathrm{H_2O} \right) \right] , \tag{3.1}$$

where $E_\mathrm{slab|H_2O}$ is the energy of combined system, E_slab of the clean slab, $E_\mathrm{H_2O}$ of an isolated water molecule and $N_\mathrm{H_2O}$ the number of water molecules [27]. Within the framework of the computational hydrogen electrode (CHE) of Nørskov *et al.* [15], the stability of a structure and the activity of a catalyst are predicted based on an identical measure of adsorption energies of relevant reaction intermediates, e.g. adsorbed hydrogen.

Computing such adsorption energies at applied potential conditions necessitates, in addition, charging of the interface by an appropriate amount [17]. In this respect, one of the central quantities of interest is the work function of the interfacial system, as it directly impacts how much excess charges are present on the surface at a given applied potential and therewith the energetics of e.g. charged adsorbates. Adsorbed water on a metallic electrode is known to reduce the work function significantly which leads to a sizeable offset of the so-defined potential of zero charge (PZC) from the respective vacuum value [17]. As a result, obtaining realistic PZC values within a given interfacial water model, e.g. static water environment, is a prerequisite to model appropriately the interfacial conditions at an applied electrode potential. Typically the work function of the total system is referenced to the clean slab and therefore in the case of adsorbing interfacial water we evaluated the work function change $\Delta\Phi$ as

$$\Delta\Phi = \Phi_{\mathrm{slab}|\mathrm{H_2O}} - \Phi_{\mathrm{slab}}, \tag{3.2}$$

which can be directly compared to the experimentally measured PZC. At this potential, the electrode has no excess charge and corresponds, therefore, to the simulation of the metal-water interfaces in a canonical ensemble [28].

The analysis of static water structures clarifies that $\Delta\Phi$ and E_{ads} depend sensitively on the precise arrangement of water molecules as shown in Fig. 6 for the Pt(111)-water interface, taken from Ref. [27]. Because water has a significant dipole, the opposite orientation of every second water molecule in both structures leads to a difference in the work function of roughly $1.5\,\mathrm{eV}$. Similar effects of the water reorientation on the work function were reported in the literature [24, 76–78]. Note that this difference exceeds by far the predicted electrochemical stability window of water on Pt(111) [79]. Furthermore, the connectivity of the two structures is different, which is underlined by the blue color of parallel-oriented and tightly adsorbed water molecules. The configuration on the left is additionally slightly closer to the slab, which together with the previous points causes the large difference in the adsorption energy of almost $0.1\,\mathrm{eV}$ per water molecule. These values are similar to reported values in the literature [24, 76–78].

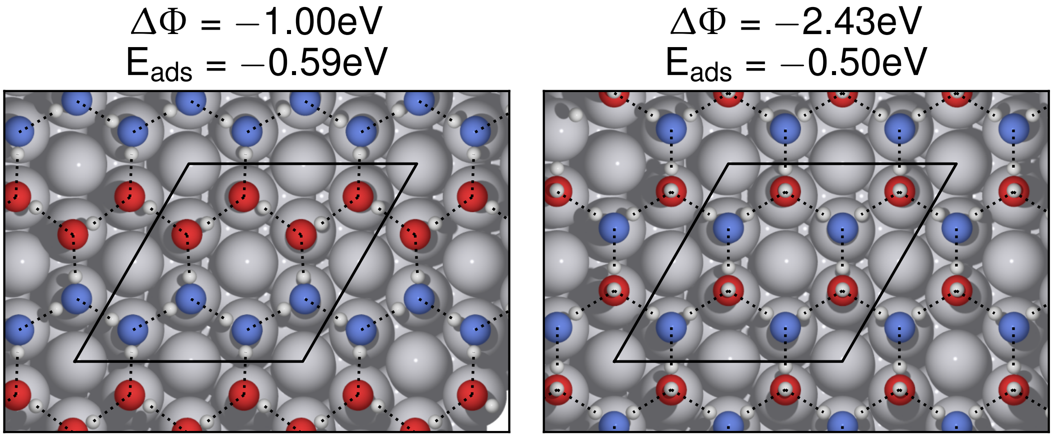

Figure 6 Example configurations for a hexagonal water arrangement on Pt(111), where the dangling hydrogen bond is either pointing towards (H-down) or away from the surface (H-up). The different orientation of the non-planar water molecules induces a significant reduction of the work function $\Delta\Phi$. The structures and values for the work function reduction and adsorption energy were taken from Ref. [27]. Intermolecular hydrogen bonds are marked with dotted lines and parallel-oriented and tightly adsorbed water molecules are colored blue.

While these two configurations can be considered as potential prototype structures of water at negatively and positively charged Pt(111), respectively, the metal-water interface at ambient conditions does not show this degree of order [80, 81] as displayed in Fig. 7. In addition, many *ab initio* molecular dynamics (AIMD) studies on different metal-water interfaces have revealed, that the ordering and orientation of interfacial water depends sensitively on the metal surface [28, 80, 82–84]. While the first water layer on Pt(111)/Pd(111) has a bimodal density distribution, only one density peak exists on Au(111)/Ag(111) [28]. Additionally, the closely bound water molecules on Pt(111)/Pd(111) exhibit a very low mobility [83, 85]. Also, the orientation and hydrogen bonding depends on the metal [28, 82, 84, 86]. Especially under electrochemical conditions with applied potential or charge, the first water layer changes its orientation and adsorption behavior [31, 83, 85, 87–89]. Despite all these differences to ice-layers, the interfacial water has very slow dynamics [20, 90, 91], such that MD simulations rather explore the local phase space than the global one. This results in differences in averaged values between different MD runs [29] and limits these simulations to a few test cases like water on Pt(111) or Au(111) [67]. A possible solution to this problem relies on the exploration of the global space via the creation of a diverse set of structures. Since the properties of water in the second water layer are already similar to bulk water, this approach can be limited to the interfacial water. Through a local geometry optimization such an approach could explore many different local minima. Finally, averages over such an ensemble should yield similar results as MD simulations and this was the basic idea of the first publication described in this thesis [27].

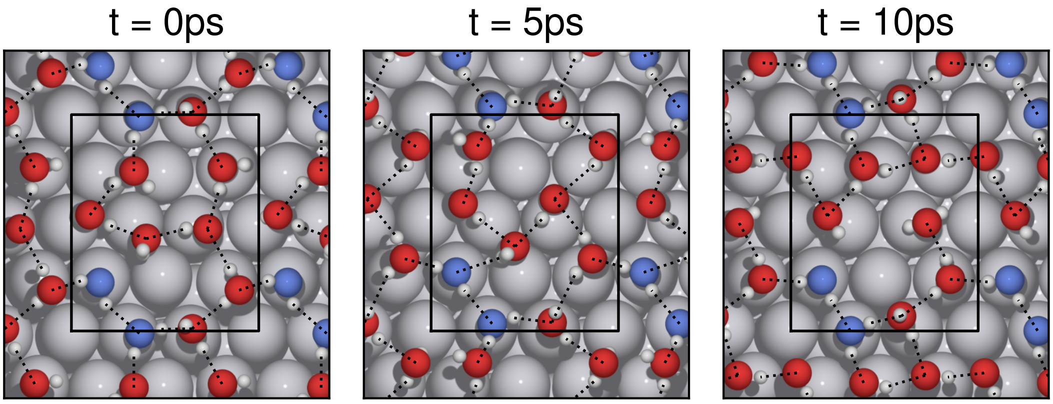

Figure 7 Example snapshots from an AIMD of interfacial water on Pt(111). Intermolecular hydrogen bonds are marked with dotted lines and parallel-oriented and tightly adsorbed water molecules are colored blue.

In addition, water (or any other solvent) changes the energetics of other adsorbates at the SLI. For example, the experimentally observed adsorption energy of phenol on Pt(111) is reduced in an aqueous environment compared to the gas-phase adsorption [38], which is referred to as competitive adsorption. The connection between competitive adsorption and interfacial solvation can be rationalized by considering the free energy change of bringing a solute to an interface in a solvent. This free energy change can be decomposed, at least phenomenologically, into the free energy changes due to the (partial) removal of the solvation shell of the solute, the removal of the local solvation environment of the substrate, and finally the formation of a (chemical or physical) bond between the solute and the substrate. The first and last contributions depend on the solute-solvent and solute-substrate interactions, respectively. The energetic cost of interfacial solvent removal, on the other hand, is likely to be dominated by the specific interactions between the solvent and the substrate only. These general baseline free energy contributions are rather agnostic to the specific adsorbate being studied and relate only to the interfacial solvation properties of the substrate. It is these ideas that motivated the studies in the second publication [34].

3.3. Interfacial Cavity Formation

As outlined in the previous section, calculating converged values of adsorption energies or work functions at metal-water interfaces requires excessive sampling. To screen different adsorption processes on various metal surfaces under different conditions, the sampling of water's degrees of freedom has to be sped up. Similarly to the dimensionality reduction in an FES, the degrees of freedom of water might be integrated out by replacing the explicit water with a continuum representation. Such models are called implicit solvation models [30] and the free energy change of solvation can be calculated as

$$\Delta G_{\mathrm{sol}} = \Delta G_{\mathrm{el}} + \underbrace{\Delta G_{\mathrm{cav}} + \Delta G_{\mathrm{rep}} + \Delta G_{\mathrm{dis}} + \Delta G_{\mathrm{tm}} + P\Delta V,}_{\mathrm{non-electrostatic\ terms}} \tag{3.3}$$

where ΔG_{el} is the contribution of the dielectric response and all other terms regard the non-electrostatic contributions [92, 93]. They include the creation of a free volume for the solute ΔG_{cav}, the repulsion between solute and solvent ΔG_{rep}, the attractive dispersion ΔG_{dis}, the change of the thermal motion ΔG_{tm}, and the change of the volume/ the required work $P\Delta V$ [92, 93]. While the decomposition of solvation energies into individual parts is not unambiguous, a general understanding of adsorption processes at SLIs under electrochemical conditions e.g. applied potential can be obtained by the usage of implicit solvation models [94–96]. Following Eq. 3.3, a solvation process can be understood in two steps: the creation of the cavity ΔG_{cav} in the solvent and subsequently the insertion of the solute and the embedding of the solute into the solvent ΔG_{emb}, which contains all other terms. This idea is illustrated in Fig. 8.

By construction of the decompositon and as evident from Fig. 8, ΔG_{cav} and thus its computational assessment only requires knowing the cavity's size and shape. Therefore, cavity formation applies to any solute and is, therefore, of fundamental interest for solvation processes. From thermodynamics, the work required to create an infinitely large spherical cavity (or in this case, a bubble) can be expressed as

$$W\left(r_{\mathrm{cav}}\right) = P\frac{4}{3}\pi r_{\mathrm{cav}}^3 + 4\pi r_{\mathrm{cav}}^2\gamma = PV + \gamma A, \tag{3.4}$$

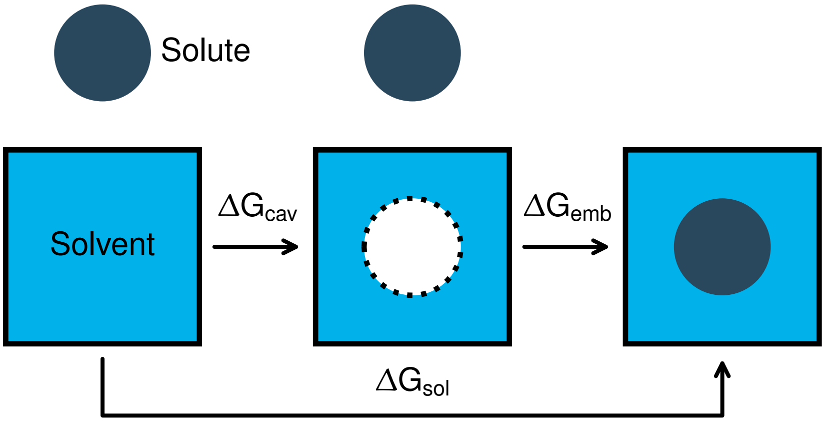

Figure 8 Solvation as a two-step process. 1. The cavity is created within the solvent to accommodate the solute. 2. The solute is inserted into the cavity and embedded into the solvent.

where P is the surrounding pressure, r_{cav} is the radius of the spherical cavity and γ the surface tension [97]. However, for smaller cavities and droplets, it is known that the surface tension is size dependent, which can be expressed using the Tolman length δ [98] as

$$\tilde{\gamma}\left(r_{\mathrm{cav}}\right)=\gamma\left(1-\frac{4\delta}{r_{\mathrm{cav}}}\right). \tag{3.5}$$

It is generally accepted that δ is positive for cavities and negative for droplets [99]. Combining Eqs. 3.4 and 3.5 yields an expression suitable for smaller cavities:

$$W\left(r_{\mathrm{cav}}\right)=P\frac{4}{3}\pi r_{\mathrm{cav}}^{3}+4\pi r_{\mathrm{cav}}^{2}\gamma\left(1-\frac{4\delta}{r_{\mathrm{cav}}}\right). \tag{3.6}$$

Furthermore, a similar expression can be derived from scaled particle theory (SPT), which uses the known radial distribution function of a liquid of hard spheres to calculate the required work to form a cavity [100]. Finally, the work is expressed as a polynomial expansion

$$W\left(r_{\mathrm{cav}}\right)=K_0+K_1\cdot r_{\mathrm{cav}}+K_2\cdot r_{\mathrm{cav}}^{2}+K_3\cdot r_{\mathrm{cav}}^{3}, \tag{3.7}$$

where the coefficients are a function of the diameter of the hard spheres and the density of the pure liquid, as well as the pressure and temperature [101]. Comparing Eq. 3.6 and Eq. 3.7 shows that the atomistic treatment added a cavity size-independent term K_0, which has no counterpart in thermodynamics. Normalizing the work or cavity formation by the created interfacial area yields a size-dependent or effective surface tension, which is plotted for both expressions in Fig. 9. Focusing on the effective surface tension is justified, since the contribution of the pressure for small cavities is negligible at ambient conditions [102]. For the 4 coefficients, SPT relations were used:

$$K_0 = \beta\left[-\ln(1-y) + \frac{9}{2}\left(\frac{y}{1-y}\right)^2\right] - \frac{\pi p a^3}{6} \tag{3.8}$$

$$K_1 = -\frac{\beta}{a}\left[\frac{6y}{1-y} + 18\left(\frac{y}{1-y}\right)^2\right] + \pi p a^2 \tag{3.9}$$

$$K_2 = \frac{\beta}{a^2}\left[\frac{12y}{1-y} + 18\left(\frac{y}{1-y}\right)^2\right] - 2\pi p a \tag{3.10}$$

$$K_3 = \frac{4}{3}\pi p \tag{3.11}$$

with a being the hard sphere diameter of water, ρ the number density and $y = \pi a^3 \rho/6$ the packing fraction.

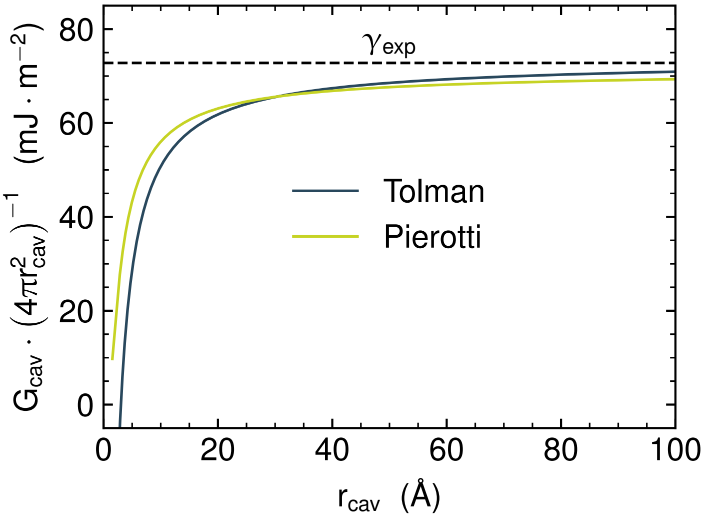

Figure 9 Area-normalized cavity formation free energy at $20\,^{\circ}\mathrm{C}$ and $1\,\mathrm{atm}$ according to Eq. 3.6 (Tolman lenth: $\delta = 0.7582\,\text{Å}$ [103], surface tension of water: $\gamma = 0.0728\,\mathrm{J\,m^{-2}}$ [102]) and Eq. 3.8 (number density of water: $\rho = 0.0334\,\text{Å}^{-3}$ [104], hard-sphere diameter of water: $\sigma = 2.888\,\text{Å}$ [102]).

It is evident from Fig. 9 that the study of small cavities ($r_{\mathrm{cav}} < 10\,\text{Å}$) is of particular interest, since the effective surface tension changes drastically in this regime. However, the solvent and the solute are approximated as single hard spheres in the SPT framework and, due to the ambiguity of choosing appropriate hard-sphere diameters – e.g. for non-spherical solvent molecules – results are only semiquantitative and highly sensitive [102]. In contrast, free energy calculations from atomistic simulations can access the size dependence of the effective surface tension and clarify these shortcomings of SPT [35–37, 105, 106]. Using the established connection between probability and free energy (cf. Eq. 2.24), the cavity formation free energy can be determined by inserting test particles into a configuration and evaluating their interaction with all other particles in the system, commonly referred to as Widom insertion method [107]. Since the interaction between a cavity modelled as a hard sphere and all other atoms is infinite if the atoms are closer than the hard sphere radius and zero beyond that, it is sufficient to check the distance between test particles and closest neighbouring atom. Afterwards the free energy is calculated as

$$\Delta G_{\mathrm{cav}} = -\beta^{-1} \cdot \ln \left[P \left(r_{\mathrm{cav}} \right) \right] \tag{3.12}$$

with the probability $P\left(r_{\mathrm{cav}}\right)$, that the distance to the closest neighbouring atom is smaller than the cavity size r_{cav}, for all inserted test particles. This approach utilizes the trajectories of simulations / a simulation without an explicit cavity and demands a simple post-processing. However, the statistical error is large as large cavities are rarely formed naturally thus limiting its applicability to small cavities only [106]. For spatially inhomogeneous systems, the probability in Eq. 3.12 can be evaluated as a function of space as well [20, 108]. A different approach introduces explicit cavities to the solvent and calculates the energy difference for expanding the cavity. The cavity would be modeled via a repulsive potential which creates a solvent-free space. The size depends on the parameters of the employed potential and the free energy difference can be calculated with FEP for the different sized cavities [109]. The results of this approach are not directly comparable to SPT or particle insertion, because they treat the particles as hard spheres, while in FEP the cavity is modeled via a soft potential. Therefore, relations between a soft potential and hard spheres are required, which are established for the so-called Weeks-Chandler-Andersen (WCA) potential [110, 111]. The WCA potential is a shifted and truncated LJ potential:

$$U_{\mathrm{WCA}}(r) = \begin{cases} 4\epsilon \cdot \left[\left(\frac{\sigma}{r}\right)^{12} - \left(\frac{\sigma}{r}\right)^{6} \right] + \epsilon & r \leq 2^{1/6}\sigma \\ 0 & r > 2^{1/6}\sigma \quad , \end{cases} \tag{3.13}$$

It was shown that the Boltzmann factor criteria links the potential to the corresponding hard sphere radius, such that $U_{\mathrm{WCA}}(r = r_{\mathrm{cav}}) = k_{\mathrm{B}}T$ [110, 111]. An example for a LJ and a corresponding WCA potential is shown in Fig. 10. The hard sphere radius and the cutoff of the WCA potential are shown as well. The WCA potential can easily be constructed by choosing these two parameters and calculating ϵ and σ correspondingly.

Furthermore, these free energy calculations demand long MD runs to converge and the system size must be large enough that cavities do not interact with their periodic images. Therefore, these studies are mainly carried out with FFs [35–37, 105, 106]. However, there is a dependence on the chosen FF for key properties like the surface tension [72]. Furthermore, the formation of cavities might change heavily at an SLI [20, 31, 112, 113]. A simple explanation is that at hydrophobic surfaces, water is expelled and the formation of cavities is favored, while at hydrophilic surfaces it is the other way around [113]. This rather trivial connection,

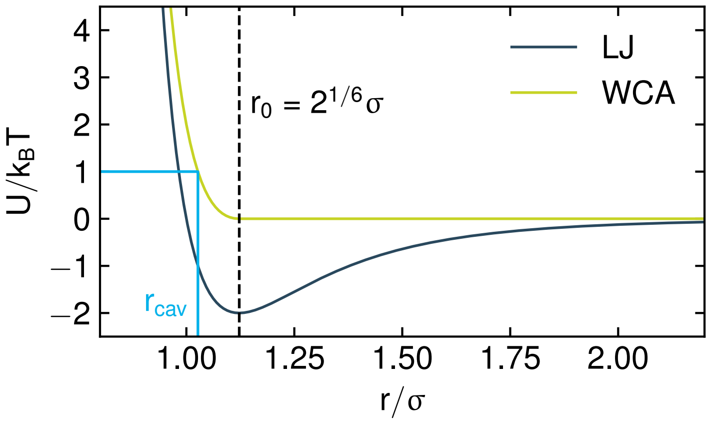

Figure 10 Example of the LJ and WCA potential with $\sigma = 1.5$ Å and $\epsilon = 2k_\mathrm{B}T$. The blue line marks the corresponding radius of a hard sphere for $U\left(r_\mathrm{cav}\right) = k_\mathrm{B}T$ and the dashed, black line the cutoff of the WCA potential.

however, does not allow for a quantification of this phenomenon, which is required for adsorption processes at an SLI. In Fig. 11 this is demonstrated by showing the corresponding two-step process at these interfaces. The competition between the solvent and an adsorbate for the adsorption site on a substrate is called competitive adsorption [29, 33, 38, 39] and it can to a large degree be understood by considering cavity formation at an SLI as depicted in Fig. 11 [30]. A comparison with Fig. 8, clarifies the central difference to cavity formation in bulk liquids: While only one type of interface is present for a cavity in solution, two types of interfaces are created when forming it at an SLI – the solution-cavity and the substrate-cavity interface.

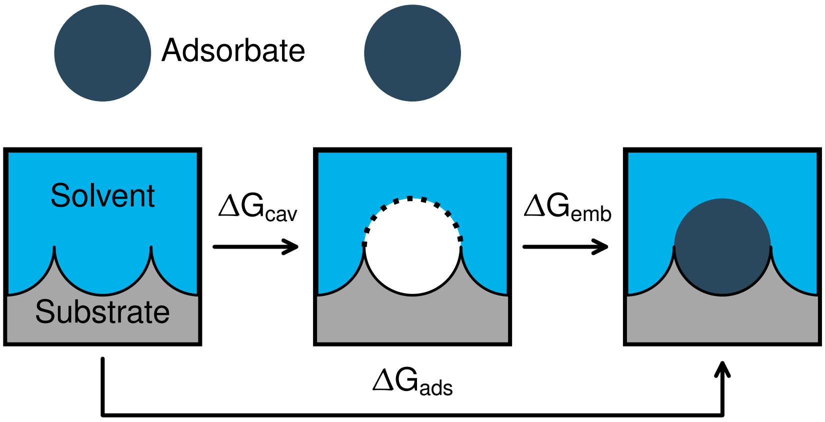

Figure 11 Adsorption at SLIs as a two-step process. 1. The cavity is created at the SLI to create space for the adsorbate. 2. The adsorbate is inserted into the cavity, binds to the substrate and is embedded into the solvent.

As described in the previous sections, reactions at SLI are highly relevant but predictions of current implicit solvation models are prone to errors [29, 33]. This originates from the parametrization of these models, since they are trained on bulk solvation energies and hence take cavity formation energies only into account in its bulk form as shown in Fig. 8 [29, 30]. For bigger adsorbates as phenol or benzene, the adsorption energies at the Pt(111)-water interface from implicit solvation models are significantly lower than in experiments [38] or in calculations with explicit solvation models [33, 39]. However, in principle implicit solvation models can be adjusted to account for cavity formation at SLI as shown by Bramley *et al.* [32], which reduces the deviations from experimental values. This requires to include substrate-specific ΔG_{cav} in such implicit solvent models. As the respective parameter values are not known *a priori* and hardly accessible from experiments the focus of the second publication of this thesis is the calculation of the cavity formation free energy for different metal-water interfaces [34]. The cavity was modelled via WCA potentials and their position and size were changed to calculate the free energy difference.

4. Publications

4.1. Static and dynamic water structures at interfaces: A case study with focus on Pt(111)

Alexandra C. Dávila López[*], Thorben Eggert[*], Karsten Reuter, and Nicolas G. Hörmann
J. Chem. Phys. **2021**, *155*, 194702.
[*]These authors contributed equally to the work.

Summary: In this work, we analyzed the structural and energetic properties of static and dynamic water layers from first principles of the Pt(111)-water interface. For this purpose, we developed a routine for the systematic creation of static water layers on different substrates. First, predefined water films of different geometries like chains or hexagons were placed on a substrate via lattice matching. Subsequent geometry optimization with DFT yielded a diverse set of configurations with a wide range of work function changes and adsorption energies. Through the study of the hydrogen bonding and comparison with existing data from AIMDs, we found correlations between the number of hydrogen bonds and the adsorption energy and a systematic bias towards free hydrogen bonds pointing towards the surface within the static ensemble. We attributed this structural bias to the absence of further water layers and the thermal motion from the AIMDs. Encoding the chemical environment with the smooth overlap of atomic positions (SOAP) as descriptor confirmed this finding as the most similar structures from the static ensemble were the ones with a few hydrogen bonds and a chain-like geometry. Nonetheless, we outlined the utility of a diverse set of interfacial water structures in prevalent high throughput studies that rely on quasi-static water environments, as AIMDs are too expensive, as well as for calculations of kinetic barriers.

Individual Contributions: I performed the structural comparison between the static and dynamic layers included in this work. This includes the geometrical properties like the coordination number and the hydrogen bonding, as well as the encoding of the local environment with the SOAP descriptor and the subsequent dimensionality reduction via principal component analysis. Additionally, the first water layer of the literature data sets needed to be identified, for which I contributed to the development of an inhouse algorithm to detect surface atoms. I performed the DFT single-point simulations of data from Ref [28] to reanalyze the work function change and adsorption energy. Furthermore, I contributed to the python package published alongside this work. Finally, Alexandra C. Dávila López, Nicolas G. Hörmann and I wrote the manuscript.

4.2. Cavity formation at metal-water interfaces

Thorben Eggert, Nicolas G. Hörmann, and Karsten Reuter
J. Chem. Phys. **2023**, *159*, 194702.

Summary: In this study, we analyzed cavity formation at eight different metal-water interfaces with classical force fields. Free energy perturbation with MBAR was performed to calculate the cavity formation free energy as a function of cavity position and size. The subsequent analysis of the obtained free energy profiles revealed substrate-dependent cavity formation energies. We rationalized this dependency with the binding strength of the substrates with water as the adsorption energy of a single water molecule. In addition, we used a simple Gibbs-Model of two phases with a sharp interface to fit the curves, which yielded effective interface tensions for the substrate-water and water-vacuum interface. We benchmarked our findings for the effective surface tension of water against literature values and found a good agreement. The investigation of the substrate-water effective surface tensions revealed a deviation from the expected asymptotic behavior from SPT. As the origin, we pointed out the lattice of the substrate, which resulted in a modulation of the free energy depending on the surface sites blocked by the cavity. Lastly, we pointed out that our findings are in good agreement with studies of the adsorption of phenol on Pt(111) in an aqueous environment, which exemplifies the utility of our approach to correct implicit solvation models with substrate-dependent cavity formation energies.

Individual Contributions: Nicolas G. Hörmann and I developed the general idea to spatially resolve the cavity formation free energies at different metal-water interfaces together. I generated and analyzed the data for this publication. For this purpose, I developed the protocol for the MD simulations with an explicit cavity and the subsequent free energy perturbation via MBAR. Together with Nicolas G. Hörmann and Karsten Reuter, we related our findings to SPT and the concept of competitive adsorption. The manuscript was written jointly by Nicolas G. Hörmann, Karsten Reuter, and me.

5. Conclusion and Outlook

Even though SLIs are present in many (electro)chemical applications, resolving their atomistic structure remains an ongoing challenge with many unknowns. The complicated nature of these systems limit studies at present to a few model systems like the Pt(111)-water interface. Despite the impressive findings on these systems, the models are of course idealized, and the thermodynamic conditions may differ in experiments or real applications [19]. Therefore, transferring the knowledge gained from these models to real systems is necessary to systematically improve them [30, 68].

In the first publication of this work [27], we investigated the possibility of efficiently exploring the phase space of SLIs by combining substrates with two-dimensional water films. This approach yielded a diverse set of local minima with different water orientations and bonding geometries. In addition, the configurations demonstrated the sensitivity of the work function and adsorption energy to the precise structuring of the interfacial water. The comparison with AIMD data [28, 29] revealed a structural bias towards hydrogen pointing to the surface and higher degree of hydrogen bonding within the interfacial water layer of the most stable structures, whereas the closest similarity was found for chain-like structures. However, the construction protocol enables easy access to different local minima and might therefore be a tool for efficient sampling by providing initial structures to MDs. In addition, previous studies on the adsorption of molecules in the presence of water often utilized the static hexagonal water bilayer, but as shown in this paper other configurations from our protocol might be more appropriate to represent water at ambient conditions.

In the second paper [34], we further developed this idea. Instead of using representative static water structures for the study of competitive adsorption processes at metal-water interfaces, we wanted to quantify the free energy required to remove water from such interfaces. Accessing this energy would allow to improve implicit solvation models [30], which fail to describe competitive adsorption processes at SLIs [29]. We demonstrated that cavity formation at the interface is indeed connected to the metal-water binding strength and that the energetic contribution becomes significant already for rather small adsorbates. Especially for molecules with similar sizes of phenol, we found that the inclusion of cavity formation changed adsorption energies from implicit solvation models by roughly $1\,\mathrm{eV}$ for the Pt(111)-water interface. These findings are in good agreement with experimental findings for phenol on Pt(111) and theoretical works with explicit solvation [32, 33, 38, 39]. The inclusion of substrate-specific cavity formation into implicit solvent models might, therefore, enable the study of adsorption processes at more complex and less ideal systems. In particular, calculations of nanoparticles with edges and kinks, which resemble the catalyst under reaction conditions more closely, would benefit from these findings, since they cannot be sampled appropriately with AIMDs. In addition, the assessment of free energy differences is still rare in AIMD studies as free energy perturbation or integration methods require significantly more sampling and/or direct manipulations of the system's Hamiltonian. From the energetic cost to replace water from the interface, a generic destabilization of adsorbates on hydrophilic substrates is expected, which might shift Volcano plots based on gas-phase adsorption energies, as found for furfural at metal–water interfaces from AIMDs [114].

For future work, the static water layers and the developed protocol can serve as a starting point for calculating kinetic barriers [115, 116] under electrochemical conditions, e.g. at applied potential. The various two-dimensional water films allow a sensitivity analysis of the barriers to the chosen configuration of water. The findings regarding competitive adsorption and cavity formation are not specific to metal-water interfaces but are transferable to other systems. On the same metal, the competitive nature can be adjusted by the solvent [117], which can also be accessed through the study of interfacial cavities. In addition, the correlation between the blocking of favorable adsorption sites and the increasing free energy of cavity formation is an interesting starting point for the study of less homogeneous substrates such as metal oxides [118], where the adsorption energies on the different atoms can vary drastically. In addition, the setup can be adapted to include more complexity of the real system like polarization, ions, and the specific adsorption of water, which will necessitate using more complex force fields or machine-learned potentials. Finally, the inclusion of substrate-dependent cavity formation energies in implicit solvent models and their efficient parameterization is an ongoing challenge.

Acknowledgements/Danksagung

Zunächst möchte ich mich bei meinem Doktorvater, Karsten Reuter, und meinem Betreuer, Nicolas Hörmann, für die vergangenen vier Jahre und die Möglichkeit, in diesem Bereich zu promovieren, bedanken. Besonders dankbar bin ich für die vielen Anregungen und Freiräume, eigene Projekte zu entwickeln und umzusetzen, sowie für die Hilfe und den Rat in den spannenden Phasen der Fertigstellung der Publikationen und dieser Arbeit. Darüber hinaus möchte ich mich bei allen meinen Kollaborateuren bedanken, insbesondere bei Alexandra Dávila López für unsere gemeinsame Publikation, bei Christoph Scheurer und Sebastian Matera für ihre Unterstützung bei der Zusammenarbeit mit Andreas Stierle und Simon Cheng vom DESY, bei Clotilde Cucinotta und ihrer Arbeitsgruppe für den spannenden zweimonatigen Forschungsaufenthalt am Imperial College London und bei Andrea Auer von der Universität Innsbruck für die enge Zusammenarbeit zwischen Experiment und Theorie. Zusätzlich möchte ich Lukas Hofer danken, dessen Bachelorarbeit ich betreuen durfte.

Während der letzten vier Jahre habe ich das soziale Miteinander und den wissenschaftlichen Austausch in unserer Abteilung immer sehr genossen und möchte mich auch dafür bei allen Kollegen und besonders bei meiner Subgroup Hörmann herzlich bedanken. Gerade der fachliche und wissenschaftliche Input von Simeon zu Beginn meiner Promotion hat mir sehr geholfen. Auch die vielen Gespräche und Diskussionen in unserem alten Büro mit Zausi (Nicolas B.) werden mir in bester Erinnerung bleiben. Da der Beginn dieser Arbeit mit dem Ausbruch der COVID-Pandemie zusammenfiel, war der Umzug von München nach Berlin ein noch größerer Umbruch, als ich es mir je hätte vorstellen können. Gerade deshalb möchte ich mich bei der ersten Gruppe am Institut (Elisabetta, Sina, Simon, Frederic, Hanna, David, Christian) bedanken, denn mit ihnen war das Institut sofort mehr als nur ein Arbeitsplatz. Gleiches gilt für meinen alten Mitbewohner und Freund, Max, und meine Freunde vom SC Brandenburg, die Berlin für mich so heimisch gemacht haben. Als wieder mehr soziale Aktivitäten möglich waren, hat die Abteilung auch immer wieder großartige Veranstaltungen auf die Beine gestellt (Weihnachtsfeiern, Sommerfeste und International Food Evenings), danke für dieses tolle Atmosphäre. Besonders bedanken möchte ich mich auch bei Carsten und Alexandra für die gemeinsame Organisation der Gruppenworkshops 2021 und 2022. Vielen Dank auch an die Organisatoren der anderen beiden Workshops, die ich besuchen durfte. Natürlich möchte ich mich auch sehr bei Julia, Steffen und Ruth für ihre Hilfsbereitschaft bei allen Fragen bedanken, sowie bei Simeon und Zausi für die Unterstützung bei technischen Aspekten. Auch die kleinen Aktivitäten (Bouldern, Volleyball, Pub Quiz, Joggen, ...) neben der Arbeit sollen nicht unerwähnt bleiben, vielen Dank.

Auch außerhalb der Arbeit haben mich viele Menschen auf diesem Weg unterstützt und begleitet, bei denen ich mich bedanken möchte: Angefangen bei meinen alten Schulfreunden aus Lüdenscheid, meinen engagierten Chemielehrern, Herr Drees und Frau Koopmann, stellvertretend für die vielen guten Lehrkräfte aus meiner Schulzeit und meinen Freunden und ehemaligen Kommilitonen in München, die meine Studienzeit so großartig gemacht haben, und bei all meinen Freunden in Berlin, die diese Zeit so bereichert haben. Ganz besonders

möchte ich mich bei meiner Freundin Elisabetta für die wunderbare zweite Hälfte meiner Promotion bedanken, in der ich so viel Unterstützung und Freude durch sie erlebt habe.

Abschließend möchte ich mich bei meiner Familie bedanken, vor allem bei meinen Eltern, die mich immer begleitet und unterstützt haben. Danke, dass ihr mir immer die Freiheit gelassen habt, meinen eigenen Weg zu finden.

Berlin, 13. Februar 2024

Bibliography

[1] J. Rockström, O. Gaffney, J. Rogelj, M. Meinshausen, N. Nakicenovic, H. J. Schellnhuber, *Science (80-.).* **2017**, *355*, 1269–1271.

[2] C. Dupont, S. Oberthür in *Decarbonization Eur. Union*, Palgrave Macmillan UK, London, **2015**, pp. 1–24.

[3] K. Calvin, D. Dasgupta, G. Krinner, A. Mukherji, P. W. Thorne, C. Trisos, J. Romero, P. Aldunce, K. Barrett, G. Blanco, W. W. Cheung, S. Connors, F. Denton, A. Diongue-Niang, D. Dodman, M. Garschagen, O. Geden, B. Hayward, C. Jones, F. Jotzo, T. Krug, R. Lasco, Y.-Y. Lee, V. Masson-Delmotte, M. Meinshausen, K. Mintenbeck, A. Mokssit, F. E. Otto, M. Pathak, A. Pirani, E. Poloczanska, H.-O. Pörtner, A. Revi, D. C. Roberts, J. Roy, A. C. Ruane, J. Skea, P. R. Shukla, R. Slade, A. Slangen, Y. Sokona, A. A. Sörensson, M. Tignor, D. van Vuuren, Y.-M. Wei, H. Winkler, P. Zhai, Z. Zommers, J.-C. Hourcade, F. X. Johnson, S. Pachauri, N. P. Simpson, C. Singh, A. Thomas, E. Totin, A. Alegría, K. Armour, B. Bednar-Friedl, K. Blok, G. Cissé, F. Dentener, S. Eriksen, E. Fischer, G. Garner, C. Guivarch, M. Haasnoot, G. Hansen, M. Hauser, E. Hawkins, T. Hermans, R. Kopp, N. Leprince-Ringuet, J. Lewis, D. Ley, C. Ludden, L. Niamir, Z. Nicholls, S. Some, S. Szopa, B. Trewin, K.-I. van der Wijst, G. Winter, M. Witting, A. Birt, M. Ha, IPCC, 2023: Climate Change 2023: Synthesis Report. Contribution of Working Groups I, II and III to the Sixth Assessment Report of the Intergovernmental Panel on Climate Change [Core Writing Team, H. Lee and J. Romero (eds.)]. IPCC, Geneva, Switzerland. Tech. rep., Intergovernmental Panel on Climate Change, **2023**.

[4] T. M. Gür, *Energy Environ. Sci.* **2018**, *11*, 2696–2767.

[5] M. Yue, H. Lambert, E. Pahon, R. Roche, S. Jemei, D. Hissel, *Renew. Sustain. Energy Rev.* **2021**, *146*, 111180.

[6] L. Fan, Z. Tu, S. H. Chan, *Energy Reports* **2021**, *7*, 8421–8446.

[7] U.S. National Clean Hydrogen Strategy and Roadmap, tech. rep., United States Department of Energy, **2023**.

[8] Y. Wang, D. F. Ruiz Diaz, K. S. Chen, Z. Wang, X. C. Adroher, *Mater. Today* **2020**, *32*, 178–203.

[9] S. Shiva Kumar, V. Himabindu, *Mater. Sci. Energy Technol.* **2019**, *2*, 442–454.

[10] M. A. Abdelkareem, K. Elsaid, T. Wilberforce, M. Kamil, E. T. Sayed, A. Olabi, *Sci. Total Environ.* **2021**, *752*, 141803.

[11] I. E. L. Stephens, A. S. Bondarenko, U. Grønbjerg, J. Rossmeisl, I. Chorkendorff, *Energy Environ. Sci.* **2012**, *5*, 6744.

[12] I. E. L. Stephens, J. Rossmeisl, I. Chorkendorff, *Science (80-.).* **2016**, *354*, 1378–1379.

[13] Z. W. Chen, L. X. Chen, Z. Wen, Q. Jiang, *Phys. Chem. Chem. Phys.* **2019**, *21*, 23782–23802.

[14] J. Greeley, T. F. Jaramillo, J. Bonde, I. Chorkendorff, J. K. Nørskov, *Nat. Mater.* **2006**, *5*, 909–913.

[15] J. K. Nørskov, J. Rossmeisl, A. Logadottir, L. Lindqvist, J. R. Kitchin, T. Bligaard, H. Jónsson, *J. Phys. Chem. B* **2004**, *108*, 17886–17892.

[16] J. K. Nørskov, T. Bligaard, A. Logadottir, J. R. Kitchin, J. G. Chen, S. Pandelov, U. Stimming, *J. Electrochem. Soc.* **2005**, *152*, J23.

[17] N. G. Hörmann, O. Andreussi, N. Marzari, *J. Chem. Phys.* **2019**, *150*, 041730.

[18] M. H. Hansen, J. Rossmeisl, *J. Phys. Chem. C* **2016**, *120*, 29135–29143.

[19] H. Oberhofer in *Handb. Mater. Model.* (Eds.: W. Andreoni, S. Yip), Springer International Publishing, Cham, **2018**, pp. 1–33.

[20] D. T. Limmer, A. P. Willard, P. Madden, D. Chandler, *Proc. Natl. Acad. Sci. U. S. A.* **2013**, *110*, 4200–4205.

[21] D. J. Wales, T. V. Bogdan, *J. Phys. Chem. B* **2006**, *110*, 20765–20776.

[22] T. Roman, A. Groß, *J. Phys. Chem. C* **2016**, *120*, 13649–13655.

[23] V. Kapil, C. Schran, A. Zen, J. Chen, C. J. Pickard, A. Michaelides, *Nature* **2022**, *609*, 512–516.

[24] A. Hodgson, S. Haq, *Surf. Sci. Rep.* **2009**, *64*, 381–451.

[25] P. J. Feibelman, *Phys. Today* **2010**, *63*, 34–39.

[26] O. Björneholm, M. H. Hansen, A. Hodgson, L.-M. Liu, D. T. Limmer, A. Michaelides, P. Pedevilla, J. Rossmeisl, H. Shen, G. Tocci, E. Tyrode, M.-M. Walz, J. Werner, H. Bluhm, *Chem. Rev.* **2016**, *116*, 7698–7726.

[27] A. C. Dávila López, T. Eggert, K. Reuter, N. G. Hörmann, *J. Chem. Phys.* **2021**, *155*, 194702.

[28] J. Le, M. Iannuzzi, A. Cuesta, J. Cheng, *Phys. Rev. Lett.* **2017**, *119*, 016801.

[29] H. H. Heenen, J. A. Gauthier, H. H. Kristoffersen, T. Ludwig, K. Chan, *J. Chem. Phys.* **2020**, *152*, 144703.

[30] S. Ringe, N. G. Hörmann, H. Oberhofer, K. Reuter, *Chem. Rev.* **2021**, acs.chemrev.1c00675.

[31] A. Serva, M. Havenith, S. Pezzotti, *J. Chem. Phys.* **2021**, *155*, 204706.

[32] G. Bramley, M.-T. Nguyen, V.-A. Glezakou, R. Rousseau, C.-K. Skylaris, *J. Chem. Theory Comput.* **2020**, *16*, 2703–2715.

[33] P. Clabaut, B. Schweitzer, A. W. Götz, C. Michel, S. N. Steinmann, *J. Chem. Theory Comput.* **2020**, *16*, 6539–6549.

[34] T. Eggert, N. G. Hörmann, K. Reuter, *J. Chem. Phys.* **2023**, *159*, 194702.

[35] F. M. Floris, M. Selmi, A. Tani, J. Tomasi, *J. Chem. Phys.* **1997**, *107*, 6353–6365.

[36] G. Hummer, S. Garde, A. E. García, A. Pohorille, L. R. Pratt, *Proc. Natl. Acad. Sci.* **1996**, *93*, 8951–8955.

[37] F. V. Grigor'ev, A. N. Romanov, V. B. Sulimov, *Russ. J. Phys. Chem. A* **2010**, *84*, 195–202.

[38] J. Akinola, C. T. Campbell, N. Singh, *J. Phys. Chem. C* **2021**, *125*, 24371–24380.

[39] A. Takamatsu, M. Higashi, H. Sato, *Chem. Lett.* **2022**, *51*, 791–795.

[40] C. J. Cramer, *Essentials of Computational Chemistry: Theories and Models*, 2nd ed., Wiley, **2004**.

[41] C. Chipot, A. Pohorille, *Free Energy Calculations*, Springer Berlin Heidelberg, Berlin, Heidelberg, **2007**.

[42] I. I. Mizus, A. A. Kyuberis, N. F. Zobov, V. Y. Makhnev, O. L. Polyansky, J. Tennyson, *Philos. Trans. R. Soc. A Math. Phys. Eng. Sci.* **2018**, *376*, 20170149.

[43] J. P. K. Doye, M. A. Miller, D. J. Wales, *J. Chem. Phys.* **1999**, *111*, 8417–8428.

[44] F. Jensen, *Introduction to Computational Chemistry*, 2nd ed., Wiley, **2007**.

[45] P. Hohenberg, W. Kohn, *Phys. Rev.* **1964**, *136*, B864–B871.

[46] W. Kohn, L. J. Sham, *Phys. Rev.* **1965**, *140*, A1133–A1138.

[47] J. A. Harrison, J. D. Schall, S. Maskey, P. T. Mikulski, M. T. Knippenberg, B. H. Morrow, *Appl. Phys. Rev.* **2018**, *5*, 031104.

[48] J. Behler, *Chem. Rev.* **2021**, *121*, 10037–10072.

[49] D. Frenkel, B. Smit, *Understanding Molecular Simulation*, 2nd ed., Elsevier, **2002**.

[50] L. Verlet, *Phys. Rev.* **1967**, *159*, 98–103.

[51] A. P. Thompson, H. M. Aktulga, R. Berger, D. S. Bolintineanu, W. M. Brown, P. S. Crozier, P. J. in 't Veld, A. Kohlmeyer, S. G. Moore, T. D. Nguyen, R. Shan, M. J. Stevens, J. Tranchida, C. Trott, S. J. Plimpton, *Comput. Phys. Commun.* **2022**, *271*, 108171.

[52] M. P. Allen, D. J. Tildesley, *Computer Simulation of Liquids*, 2nd ed., Oxford University PressOxford, **2017**.

[53] H. J. C. Berendsen, J. P. M. Postma, W. F. van Gunsteren, A. DiNola, J. R. Haak, *J. Chem. Phys.* **1984**, *81*, 3684–3690.

[54] S. Nosé, *Mol. Phys.* **1984**, *52*, 255–268.

[55] W. G. Hoover, *Phys. Rev. A* **1985**, *31*, 1695–1697.

[56] G. J. Martyna, M. L. Klein, M. Tuckerman, *J. Chem. Phys.* **1992**, *97*, 2635–2643.

[57] J. Lemkul, *Living J. Comput. Mol. Sci.* **2019**, *1*, 5068.

[58] C. Abrams, G. Bussi, *Entropy* **2013**, *16*, 163–199.

[59] A. S. Mey, B. K. Allen, H. E. Bruce Macdonald, J. D. Chodera, D. F. Hahn, M. Kuhn, J. Michel, D. L. Mobley, L. N. Naden, S. Prasad, A. Rizzi, J. Scheen, M. R. Shirts, G. Tresadern, H. Xu, *Living J. Comput. Mol. Sci.* **2020**, *2*, 1–52.

[60] R. W. Zwanzig, *J. Chem. Phys.* **1954**, *22*, 1420–1426.

[61] C. H. Bennett, *J. Comput. Phys.* **1976**, *22*, 245–268.

[62] M. R. Shirts, J. D. Chodera, *J. Chem. Phys.* **2008**, *129*, 124105.

[63] Y. Matsunaga, M. Kamiya, H. Oshima, J. Jung, S. Ito, Y. Sugita, *Biophys. Rev.* **2022**, *14*, 1503–1512.

[64] H. Paliwal, M. R. Shirts, *J. Chem. Theory Comput.* **2011**, *7*, 4115–4134.

[65] A. Bagger, I. E. Castelli, M. H. Hansen, J. Rossmeisl in *Handb. Mater. Model.* Springer International Publishing, Cham, **2018**, pp. 1–31.

[66] T. Wang, X. Cao, L. Jiao, *Carbon Neutrality* **2022**, *1*, 21.

[67] A. Groß, S. Sakong, *Chem. Rev.* **2022**, *122*, 10746–10776.

[68] A. Bruix, J. T. Margraf, M. Andersen, K. Reuter, *Nat. Catal.* **2019**, *2*, 659–670.

[69] E. Brini, C. J. Fennell, M. Fernandez-Serra, B. Hribar-Lee, M. Lukšič, K. A. Dill, *Chem. Rev.* **2017**, *117*, 12385–12414.

[70] D. Herschlag, M. M. Pinney, *Biochemistry* **2018**, *57*, 3338–3352.

[71] P. Dauber-Osguthorpe, V. A. Roberts, D. J. Osguthorpe, J. Wolff, M. Genest, A. T. Hagler, *Proteins Struct. Funct. Genet.* **1988**, *4*, 31–47.

[72] S. P. Kadaoluwa Pathirannahalage, N. Meftahi, A. Elbourne, A. C. G. Weiss, C. F. McConville, A. Padua, D. A. Winkler, M. Costa Gomes, T. L. Greaves, T. C. Le, Q. A. Besford, A. J. Christofferson, *J. Chem. Inf. Model.* **2021**, *61*, 4521–4536.

[73] J. D. Bernal, R. H. Fowler, *J. Chem. Phys.* **1933**, *1*, 515–548.

[74] T. Bartels-Rausch, V. Bergeron, J. H. E. Cartwright, R. Escribano, J. L. Finney, H. Grothe, P. J. Gutiérrez, J. Haapala, W. F. Kuhs, J. B. C. Pettersson, S. D. Price, C. I. Sainz-Díaz, D. J. Stokes, G. Strazzulla, E. S. Thomson, H. Trinks, N. Uras-Aytemiz, *Rev. Mod. Phys.* **2012**, *84*, 885–944.

[75] B. Monserrat, J. G. Brandenburg, E. A. Engel, B. Cheng, *Nat. Commun.* **2020**, *11*, 5757.

[76] S. Meng, E. Wang, C. Frischkorn, M. Wolf, S. Gao, *Chem. Phys. Lett.* **2005**, *402*, 384–388.

[77] V. Tripkovic, M. E. Björketun, E. Skúlason, J. Rossmeisl, *Phys. Rev. B - Condens. Matter Mater. Phys.* **2011**, *84*, 115452.

[78] K. Tonigold, A. Groß, *J. Comput. Chem.* **2012**, *33*, 695–701.

[79] J. Rossmeisl, J. K. Nørskov, C. D. Taylor, M. J. Janik, M. Neurock, *J. Phys. Chem. B* **2006**, *110*, 21833–21839.

[80] S. Schnur, A. Groß, *New J. Phys.* **2009**, *11*, 125003.

[81] J. Carrasco, A. Hodgson, A. Michaelides, *Nat. Mater.* **2012**, *11*, 667–674.

[82] L. Bellarosa, R. García-Muelas, G. Revilla-López, N. López, *ACS Cent. Sci.* **2016**, *2*, 109–116.

[83] S. Sakong, A. Groß, *Phys. Chem. Chem. Phys.* **2020**, *22*, 10431–10437.

[84] P. Li, J. Huang, Y. Hu, S. Chen, *J. Phys. Chem. C* **2021**, *125*, 3972–3979.

[85] R. Khatib, A. Kumar, S. Sanvito, M. Sulpizi, C. S. Cucinotta, *Electrochim. Acta* **2021**, *391*, 138875.

[86] S. Gim, K. J. Cho, H.-K. Lim, H. Kim, *Sci. Rep.* **2019**, *9*, 14805.

[87] A. Bouzid, A. Pasquarello, *J. Phys. Chem. Lett.* **2018**, *9*, 1880–1884.

[88] J.-B. Le, Q.-Y. Fan, J.-Q. Li, J. Cheng, *Sci. Adv.* **2020**, *6*, eabb1219.

[89] Z. K. Goldsmith, M. F. Calegari Andrade, A. Selloni, *Chem. Sci.* **2021**, *12*, 5865–5873.

[90] S. K. Natarajan, J. Behler, *Phys. Chem. Chem. Phys.* **2016**, *18*, 28704–28725.

[91] A. E. G. Mikkelsen, J. Schiøtz, T. Vegge, K. W. Jacobsen, *J. Chem. Phys.* **2021**, *155*, 224701.

[92] J. Tomasi, B. Mennucci, R. Cammi, *Chem. Rev.* **2005**, *105*, 2999–3094.

[93] O. Andreussi, I. Dabo, N. Marzari, *J. Chem. Phys.* **2012**, *136*, 064102.

[94] S. D. Beinlich, N. G. Hörmann, K. Reuter, *ACS Catal.* **2022**, *12*, 6143–6148.

[95] S. D. Beinlich, G. Kastlunger, K. Reuter, N. G. Hörmann, *J. Chem. Theory Comput.* **2023**, *19*, 8323–8331.

[96] N. Bergmann, N. G. Hörmann, K. Reuter, *J. Chem. Theory Comput.* **2023**, *19*, 8815–8825.

[97] A. Ben-Naim, *Statistical Thermodynamics for Chemists and Biochemists*, Springer US, Boston, MA, **1992**.

[98] R. C. Tolman, *J. Chem. Phys.* **1949**, *17*, 333–337.

[99] Y. A. Lei, T. Bykov, S. Yoo, X. C. Zeng, *J. Am. Chem. Soc.* **2005**, *127*, 15346–15347.

[100] H. Reiss, H. L. Frisch, J. L. Lebowitz, *J. Chem. Phys.* **1959**, *31*, 369–380.

[101] R. A. Pierotti, *Chem. Rev.* **1976**, *76*, 717–726.

[102] S. Höfinger, F. Zerbetto, *Chem. Soc. Rev.* **2005**, *34*, 1012.

[103] F. Magaletti, M. Gallo, C. M. Casciola, *Sci. Rep.* **2021**, *11*, 20801.

[104] E. W. Lemmon, I. H. Bell, M. L. Huber, M. O. McLinden in *NIST Chem. WebBook, NIST Stand. Ref. Database Number 69*, (Eds.: P. Linstrom, W. Mallard), National Institute of Standards and Technology, Gaithersburg MD, 20899.

[105] D. Chandler, *Nature* **2005**, *437*, 640–647.

[106] I. Sedov, T. Magsumov, *J. Chem. Phys.* **2020**, *153*, 134501.

[107] B. Widom, *J. Chem. Phys.* **1963**, *39*, 2808–2812.

[108] B. Widom, *J. Phys. Chem.* **1982**, *86*, 869–872.

[109] S. Höfinger, F. Zerbetto, *Chem. – A Eur. J.* **2003**, *9*, 566–569.

[110] D. Ben-Amotz, G. Stell, *J. Phys. Chem. B* **2004**, *108*, 6877–6882.

[111] D. M. Heyes, H. Okumura, *Mol. Simul.* **2006**, *32*, 45–50.

[112] R. Godawat, S. N. Jamadagni, S. Garde, *Proc. Natl. Acad. Sci.* **2009**, *106*, 15119–15124.

[113] A. J. Patel, P. Varilly, S. N. Jamadagni, H. Acharya, S. Garde, D. Chandler, *Proc. Natl. Acad. Sci.* **2011**, *108*, 17678–17683.

[114] S. Liu, S. Vijay, M. Xu, A. Cao, H. Prats, G. Kastlunger, H. H. Heenen, N. Govindarajan, *J. Chem. Phys.* **2023**, *159*, 084702.

[115] K. Chan, J. K. Nørskov, *J. Phys. Chem. Lett.* **2015**, *6*, 2663–2668.

[116] P. Lindgren, G. Kastlunger, A. A. Peterson, *ACS Catal.* **2020**, *10*, 121–128.

[117] J. J. Varghese, S. H. Mushrif, *React. Chem. Eng.* **2019**, *4*, 165–206.

[118] H. H. Kristoffersen, J.-E. Shea, H. Metiu, *J. Phys. Chem. Lett.* **2015**, *6*, 2277–2281.

List of Figures

Figure 1 An example of a two-dimensional potential energy surface: $U = (1.5x_1)^2 + x_1/2 + x_1y_2 + (1.5x_2)^2 + \cos(1.5\pi x_2) + x_2/2 - 0.5$. 6

Figure 2 A microcanonical (NVE) MD on the example PES from Fig. 1. The dot marks the initial position and the initial velocity is set to zero. 11

Figure 3 The exemplary PES from Fig. 1 with two possible FESs using x_1 and x_2 as CVs and Eq. 2.24. 14

Figure 4 FES using x_2 as CV using Eq. 2.24 (Exact) and FEP via Eq. 2.33 with pymbar [62]. Eleven independent, canonical ensembles were generated at evenly spaced values of x_2 for the calculation with MBAR. The crosses in the left panel mark the location of the samples. 17

Figure 5 Schematics of a fuel cell for the conversion of hydrogen and oxygen gas to water. 18

Figure 6 Example configurations for a hexagonal water arrangement on Pt(111), where the dangling hydrogen bond is either pointing towards (H-down) or away from the surface (H-up). The different orientation of the non-planar water molecules induces a significant reduction of the work function $\Delta\Phi$. The structures and values for the work function reduction and adsorption energy were taken from Ref. [27]. Intermolecular hydrogen bonds are marked with dotted lines and parallel-oriented and tightly adsorbed water molecules are colored blue. 21

Figure 7 Example snapshots from an AIMD of interfacial water on Pt(111). Intermolecular hydrogen bonds are marked with dotted lines and parallel-oriented and tightly adsorbed water molecules are colored blue. 22

Figure 8 Solvation as a two-step process. 1. The cavity is created within the solvent to accommodate the solute. 2. The solute is inserted into the cavity and embedded into the solvent. 24

Figure 9 Area-normalized cavity formation free energy at $20\,^{\circ}$C and $1\,\mathrm{atm}$ according to Eq. 3.6 (Tolman lenth: $\delta = 0.7582$ Å [103], surface tension of water: $\gamma = 0.0728\,\mathrm{J\,m^{-2}}$ [102]) and Eq. 3.8 (number density of water: $\rho = 0.0334\,\text{Å}^{-3}$ [104], hard-sphere diameter of water: $\sigma = 2.888$ Å [102]). 25

Figure 10 Example of the LJ and WCA potential with $\sigma = 1.5$ Å and $\epsilon = 2k_{\mathrm{B}}T$. The blue line marks the corresponding radius of a hard sphere for $U\left(r_{\mathrm{cav}}\right) = k_{\mathrm{B}}T$ and the dashed, black line the cutoff of the WCA potential. 27

Figure 11 Adsorption at SLIs as a two-step process. 1. The cavity is created at the SLI to create space for the adsorbate. 2. The adsorbate is inserted into the cavity, binds to the substrate and is embedded into the solvent. 27

Appendix

Paper 1

Static and dynamic water structures at interfaces: A case study with focus on Pt(111)
Alexandra C. Dávila López*, Thorben Eggert*, Karsten Reuter, and Nicolas G. Hörmann
J. Chem. Phys. **2021**, *155*, 194702.
*These authors contributed equally to the work.

Reprinted under the terms of the Creative Commons Attribution License (CC BY 4.0).
© 2021 The Authors. The Journal of Chemical Physics published by American Institute of Physics

The Journal of Chemical Physics ARTICLE scitation.org/journal/jcp

Static and dynamic water structures at interfaces: A case study with focus on Pt(111)

Cite as: J. Chem. Phys. **155**, 194702 (2021); doi: 10.1063/5.0067106
Submitted: 13 August 2021 • Accepted: 22 October 2021 •
Published Online: 18 November 2021

Alexandra C. Dávila López,[1] Thorben Eggert,[1,2] Karsten Reuter,[1] and Nicolas G. Hörmann[1,2a)]

AFFILIATIONS

[1] Fritz-Haber-Institut der Max-Planck-Gesellschaft, Faradayweg 4-6, 14195 Berlin, Germany
[2] Chair of Theoretical Chemistry and Catalysis Research Center, Technische Universität München, Lichtenbergstr. 4, 85748 Garching, Germany

Note: This paper is part of the JCP Special Topic on The Chemical Physics of the Electrode–Electrolyte Interface.
[a)]Author to whom correspondence should be addressed: hoermann@fhi-berlin.mpg.de

ABSTRACT

An accurate atomistic treatment of aqueous solid–liquid interfaces necessitates the explicit description of interfacial water ideally via *ab initio* molecular dynamics simulations. Many applications, however, still rely on static interfacial water models, e.g., for the computation of (electro)chemical reaction barriers and focus on a single, prototypical structure. In this work, we systematically study the relation between density functional theory-derived static and dynamic interfacial water models with specific focus on the water–Pt(111) interface. We first introduce a general construction protocol for static 2D water layers on any substrate, which we apply to the low index surfaces of Pt. Subsequently, we compare these with structures from a broad selection of reference works based on the Smooth Overlap of Atomic Positions descriptor. The analysis reveals some structural overlap between static and dynamic water ensembles; however, static structures tend to overemphasize the in-plane hydrogen bonding network. This feature is especially pronounced for the widely used low-temperature hexagonal ice-like structure. In addition, a complex relation between structure, work function, and adsorption energy is observed, which suggests that the concentration on single, static water models might introduce systematic biases that are likely reduced by averaging over consistently created structural ensembles, as introduced here.

© 2021 Author(s). All article content, except where otherwise noted, is licensed under a Creative Commons Attribution (CC BY) license (http://creativecommons.org/licenses/by/4.0/). https://doi.org/10.1063/5.0067106

I. INTRODUCTION

Solid–liquid interfaces (SLIs) are ubiquitous in nature, and their study is highly relevant for understanding the (electro)chemical transformation processes that lead to natural corrosion or (electro)catalytic applications, such as in batteries, electrolyzers, or fuel cells.[1–6] While liquid properties at distances larger than ~1 nm from the interface are already bulk-like[7,8] and approximately described with standard continuum models,[9,10] the structure and composition of the first (few) solvent layers in contact with a solid surface typically show a significant dependence on, e.g., the solid substrate and the thermodynamic conditions, e.g., applied electrode potentials in electrochemistry contexts.[11–19] In aqueous solutions, an accurate atomistic treatment of the substrate–water interface necessitates the explicit inclusion of at least the first water layer for a wide range of properties such as adsorption energies or the potential of zero charge (PZC).[15,20–23] On the other hand, the sensitive dependence of these properties on the interfacial water structure[24–27] necessitates, in principle, an appropriate sampling of these to obtain reliable thermodynamic averages.[11,21,26,28,29] Indeed, as the accurate description of electronic degrees of freedom and the chemical reactivity of the substrate are important, *ab initio* molecular dynamics (AIMD) results based on density functional theory (DFT) are the only reliable benchmarks to date. The long relaxation times of interfacial water[30–32] pose, however, a significant challenge to AIMD simulations and restrict such studies to only a few selected model systems.[14–18,21,26,33–36] As a result, many studies, e.g., on adsorption and solvation energies across different substrates and adsorbates[27,37–41] or on electrochemical reaction barriers[42–49] still rely on simplified and quasi-static interfacial water models. The water–Pt(111) interface is most likely the best studied of such systems and has been addressed by AIMD simulations[13,14,21,29,50,51] and static low-temperature water models.[25,50,52–54] Typical static interfacial water models are comprised of ice-like, hexagonal interfacial layers,[20,48–50,52,54] H^{down}, H^{up}, and chain-H^{down}, and also involve more complex phases[52–55] such as $\sqrt{37} \times \sqrt{37}R25.3°$ and $\sqrt{39} \times \sqrt{39}R16.1°$. The latter structure comprises five, six, and seven water rings.[52–54] Such structures are typically less prominent in room temperature AIMD studies[16,50,56] where only (predominant) *local* water configurations can be identified.[16] This puts forward the question about the relation between theoretical results from static and dynamically sampled extended interfacial water structures and possible structural biases due to the dominant use of hexagonal water (bilayer) arrangements in applied works.[42,48,49] Furthermore, as no "standard" static water models seem available for other than the prototypical fcc-(111) surface, there is a dramatic lack of knowledge of interfacial water structures on other interfaces and substrates.

In order to fill this void, we systematically study and compare ensembles of static and dynamic water structures. We introduce first our construction protocol for obtaining a consistent set of static water structures at solid interfaces for any given surface termination, supercell size, and crystal structure. Here, we start by creating a dataset of selected, topologically different 2D water layers in vacuum. The created 2D water layers can be adsorbed on any given substrate, leveraging optimal lattice matching algorithms and consecutive geometric relaxation via DFT. Subsequently, we apply the algorithm to construct a dataset of 2D static water (2DSW) structures on low index Pt surfaces and compare the obtained structural ensemble of interfacial water with the structure of water layers from other reference works. In particular, we investigate structural similarities within quasi-2D water layers in bulk liquid water and ice, at (liquid) water–vacuum interfaces, and at Pt(111)–water interfaces using the local structure descriptor SOAP (Smooth Overlap of Atomic Positions).[57] One central aspect in this respect is the analysis of the relations between structure, adsorption energy, and work function reduction for Pt(111) with a single adsorbed water layer and as obtained from AIMD and our 2DSW ensemble. In general, the analysis reveals a bias of 2DSW structures toward three intermolecular hydrogen bonds per water and excess hydrogen bonds pointing to the substrate, which yield a maximization of the overall number of bonds within the interface in contrast to the AIMD configurations (see Secs. III B and III C). Nevertheless, we find a decent overlap between AIMD and 2DSW ensemble averages, while single selected static models exhibit large variations in their predictive quality.

II. CONSTRUCTION PROTOCOL FOR WATER LAYERS ON SUBSTRATES

Our starting point for the proposed protocol is the common understanding that the first water layer is extremely important for a variety of properties at metal–water interfaces and that H_2O–H_2O interactions dominate the total energy, at least on coinage metal low index surfaces.[8,58,59] An intuitive approach to model adsorbed water is by using water layers in vacuum as a starting guess, which directly motivates the following procedure:

- Creation of a dataset of 2D water phases in vacuum.
- Creation of the target substrate [(hkl) surface and supercell size].
- Adsorption of 2D water phases that match the substrate supercell geometry.
- Relaxation of the water adsorbate layer.

A. 2D water structures in vacuum

Based on DFT calculations, we initially investigated 15 different polymorphs of 2D water in vacuum consisting of 1–8 water molecules in the primitive cell as reported in the literature.[60–63] We varied lattice constants and unit cell shapes in order to get an overview of the typical 2D water orderings in vacuum. 2D water is highly flexible, and typical literature studies are in the context of confined water, e.g., in between two sheets of graphene, rationalizing size or pressure restrictions in the out-of-plane direction.[61] As these are not present here, a compression mainly leads to a change in the degree of buckling and stacking of water molecules into several layers, an expansion typically to the formation of 1D water chains with varying degrees of separation. In general, energetic differences per molecule between the considered systems with different numbers of water are small, indicating that complex, large-scale water patterns are not necessary to describe the approximate energetic landscape. Furthermore, a wide variety of observed water patterns can already be achieved with only four water molecules[62] in a rectangular primitive lattice, featuring water molecules arranged in rectangles, parallelograms, and hexagons (see Fig. 1). Note that known prototypical motives such as squares, rectangles, parallelograms, and hexagons can be understood within rectangular cells by a variation in the relative position of the molecules within the cell, as shown in Fig. 1(a). Furthermore, all observed buckling patterns (water molecules not in one plane) fall in four classes, where the water network is in a plane, exhibits horizontal or vertical chains, or forms a 2D checkerboard arrangement [see Fig. 1(b)]. In addition, the relative orientation of the water molecules can follow several patterns; the most symmetric (in-plane) representations where each water molecule can maximize the number of hydrogen bonds are drawn in Fig. 1(c).

After these observations that a wide variety of different topologies are, indeed, already possible for four molecules in rectangular cells, we decided to limit ourselves to polymorphs, which obey these restrictions, as they have several advantages: On the one hand, the relatively small water unit cells allow for a more exhaustive representation of the structural landscape due to the reduced number of degrees of freedom. On the other hand, lattice matching can be achieved by smaller increments in the (water) supercell size. As a result, it is more likely to find small substrate supercells, which is beneficial, e.g., in terms of applying the protocol to many different systems. In addition, the choice of equal lattices for all water polymorphs ensures the consistent inclusion of all the considered water topologies on any substrate.

Our final set of 2D water structures consists of eight different topologies [Fig. 1(d)] that are observed in the studied selection of 15 low-temperature polymorphs and include a large variety of position (p), buckling (b), and orientation (o) patterns. We furthermore scanned the lattice constants on a logarithmically spaced grid (99 grid points), for which we report the relative stability with respect to the optimum lattice constant in Fig. 1(e). This clarifies the small energetic differences of any of these topological variants. The first six topologies are chains in the direction of the lattice

© Author(s) 2021

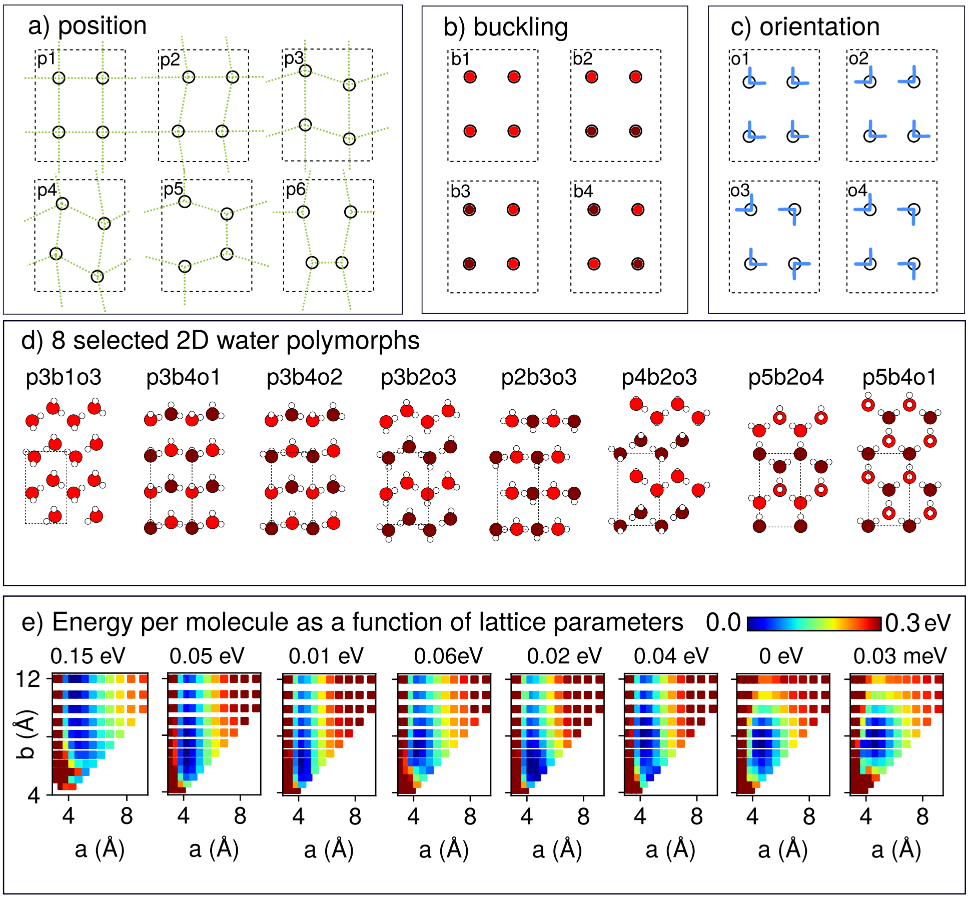

FIG. 1. (a)–(c) Basic motives of high symmetry water structures with four H_2O molecules in a rectangular cell can be discriminated by the following: (a) Different high symmetry oxygen positions in the unit cell, which yields water arrangements in rectangles, squares, parallelograms (and mixed versions), and hexagons. (b) Out-of-plane buckling patterns. Dark red is used for oxygen atoms in a lower plane. (c) Relative water orientations (fulfilling water rules). (d) Our selected set of 2D water polymorphs, named according to the topological descriptors in (a)–(c). (e) Relative energies per water molecule for different lateral dimensions scanned on a grid. Within the eight selected polymorphs, p5b2o4/p3b1o3 yields the most/least stable water structure (cf. minimum energies reported above the energy landscapes).

vector *a* such that their energy is highly sensitive to changes in that direction and largely invariant for changes in the direction of the lattice vector *b*. In contrast, the energy of the latter two configurations with their hexagonal geometry is sensitive to changes in both directions. A logarithmic lattice spacing is chosen as it leads to identical relative offsets of neighboring lattice vectors (here 10%), which ensures lattice matching (see below) without overlaps. Finally, we reduced this set to 20 identical lattice constant combinations for all eight polymorphs, which cover the lowest energy regions in order to construct our final dataset of 160 2D static water polymorphs.

B. Choice of substrate supercells

Choosing an appropriate substrate supercell evidently depends on the quantities and systems of interest. As surface cells with maximum distances to periodic images in the lateral directions are expected to yield the least periodic boundary artifacts, we think all studies on surfaces should ideally be performed in such *maximally isotropic supercells*. For this purpose, we implemented an algorithm that yields (with minimal user intervention) slabs in vacuum, which are *maximally isotropic* in the in-plane directions for any given substrate material, (*hkl*) surface, and target surface area. The algorithm is outlined in the supplementary material, and a Python implementation is provided alongside this work.

C. 2D lattice matching of 2D water phases

With our given dataset of 2D water prototypes at the varying lattice constant and chosen substrate supercell, we use (a slightly modified version of) pymatgen[64–66] to adsorb 2D water on the substrate via leveraging its implemented lattice matching[67] functionality similarly as implemented in the `pymatgen.analysis.interface` module. The logarithmic lattice spacing in our dataset ensures consistency with the lattice vector mismatch constraints in `pymatgen` (relative length differences) and enables non-overlapping matches for neighboring lattice constants.

© Author(s) 2021

In addition, we include possible lateral shifts of the adsorbed water layer (scanned on a regular grid within the primitive surface unit cell and a lateral grid spacing of ~2 Å) while also taking both possible water layer orientations into account in case the water prototype is polar in the out-of-plane direction. A self-contained Python implementation of the outlined 2DSW construction protocol is provided alongside this publication.

D. The 2DSW protocol applied to low-index Pt surfaces

Using the outlined approach, we created lattice-matched 2DSW water structures on *maximally isotropic substrate supercells* for supercell sizes between 6 and 36 surface atoms for the low index surfaces (100), (110), and (111) of fcc-Pt. While a wide variety of possible combinations for the cell size and number of water molecules is possible, interfaces with 8 and 16 water molecules take a special role as they yield matches for all three (*hkl*) terminations. Here, we restrict our analysis to minimal supercell sizes with only eight water molecules. For the Pt(111) termination, which we will analyze in more detail subsequently, the algorithm automatically chooses the well-known $(\sqrt{12} \times \sqrt{12})\mathrm{R}30^\circ$ supercell and yields 80 different initial configurations for interfacial water. These are relaxed via DFT, and we compute the adsorption energetics, as well as geometric and electronic properties (eight initial structures ran into convergence problems, which were not further analyzed and discarded). The computational parameters are reported in Subsection 2 of the Appendix, and the results for Pt(100) and Pt(110) surfaces are shown in the supplementary material.

III. PROPERTIES OF WATER LAYERS

A. Methodology

In order to analyze the water ordering of quasi-2D water layers, we used a variety of sources, including *ab initio*-determined bulk ice[68] and bulk liquid water structures,[72] liquid water slabs in vacuum,[72] liquid water on Pt(111),[15,21] and static ice-like-layers on Pt(111) from Ref. 54 and from our 2DSW construction protocol. Table I lists the according datasets together with our chosen naming convention and the most important associated properties. Note that only the latter two sets of structures [H_2O@Pt(111) ice and H_2O@Pt 2DSW] include natively well-defined quasi-2D water layers, while all other sources also incorporate in parts or in full bulk-like water regions. However, water layers are also evidently present in 3D bulk water structures (H_2O ice, H_2O AIMD) and are, in particular, distinct and non-bulk-like for water–vacuum (H_2O/vacuum AIMD) or water–Pt interfaces [H_2O@Pt(111) AIMD(P), H_2O@Pt(111) AIMD(R)].

TABLE I. Overview of the datasets used in this paper and the correspondingly used exchange–correlation functionals (plus vdW correction). The column "Setup" discriminates between the properties of the original dataset—bulk and symmetric/asymmetric slab calculations. All datasets are publicly available (see original publications), apart from the AIMD(P/R) trajectories, which were provided by the (co-)authors of the respective publications, Le *et al.*[21] and Heenen *et al.*[15]

Name	Reference	Setup	Functional(-vdW)
H_2O ice	68	Bulk	revPBE0[69,70]-D3[71]
H_2O AIMD	72	Bulk	rVV10[73]
H_2O/vacuum AIMD	72	Sym.	rVV10[73]
H_2O@Pt(111) AIMD(P)	21	Sym.	PBE[74]-D3[75,76]
H_2O@Pt(111) AIMD(R)	15	Asym.	RPBE[77]-D3[75,76]
H_2O@Pt(111) ice	54	Asym.	optPBE-vdW[78]
H_2O@Pt 2DSW	This work	Asym.	PBE[74]

In order to study the structure within these layers, we create from the latter datasets first systems with water–vacuum boundaries, if needed, and subsequently extract water layers at water–vacuum interfaces. In particular, we selected snapshots from the bulk H_2O AIMD trajectory and introduced vacuum layers at random positions along the z direction while enforcing the integrity of H_2O molecules. Similarly, for H_2O ice (54 ice phases from Ref. 68), we created water slabs up to a maximum Miller index of 3 using pymatgen[64–66] again while enforcing molecular integrity. For the water–Pt AIMD trajectories [H_2O@Pt(111) AIMD(P), H_2O@Pt(111) AIMD(R)], we removed all Pt-atoms from the system, thus creating a vacuum void. Interfacial water layers were then extracted from the so-preprocessed structures by determining all interfacial water molecules only for the respective vacuum–water interfaces of interest (e.g., the original H_2O@Pt interface) via the algorithm described in Subsection 1 of the Appendix.

The so-created structural datasets for water layers in bulk, at vacuum–water, and at Pt–water interfaces are analyzed via the use of an abstract representation for atomic environments, in particular, based on the local structure descriptor SOAP[57] as implemented in the Dscribe package[79] and as similarly performed for 3D periodic water structures.[68] Local environments are represented for each water molecule by computing a SOAP vector centered on the oxygen atom and using a cutoff radius of 4 Å, consistent with the geometrical characteristics of water. Interfacial water structures are characterized by the average over all SOAP vectors taken from each O atom in a configuration,[79] which thus also allows (global) for a structure comparison across structures that differ in the number of H_2O molecules (cf. also Subsection 3 of the Appendix).

B. The structure of extended water layers

In order to gain an intelligible, e.g., visual, representation of the similarity between and within the different structural ensembles of extended water layers, we apply principal component analysis (PCA) to the complete dataset of average SOAP vectors. The first and second PCA components are depicted in Fig. 2, and the solid lines indicate approximate locations for each dataset as obtained via kernel density estimation.[80] Additional dataset-specific plots are provided in the supplementary material. Figures 2(a) and 2(b) and the color-coding illustrate how PCA discriminates between the average number of intermolecular hydrogen bonds (upper left to the lower right) and the average number of oxygens within the SOAP radius (lower left to the upper right). Hydrogen bonds between two water molecules are defined as in Ref. 16, where the oxygens are closer than 3.5 Å to each other and the angle between O–O–H is less than 35°. There is a broad distribution of structures in the analyzed data, ranging from rather isolated water molecules to highly coordinated ones with four hydrogen bonds to its neighbors and the bulk-ice-derived layers (green line) covering the whole range, with selected

© Author(s) 2021

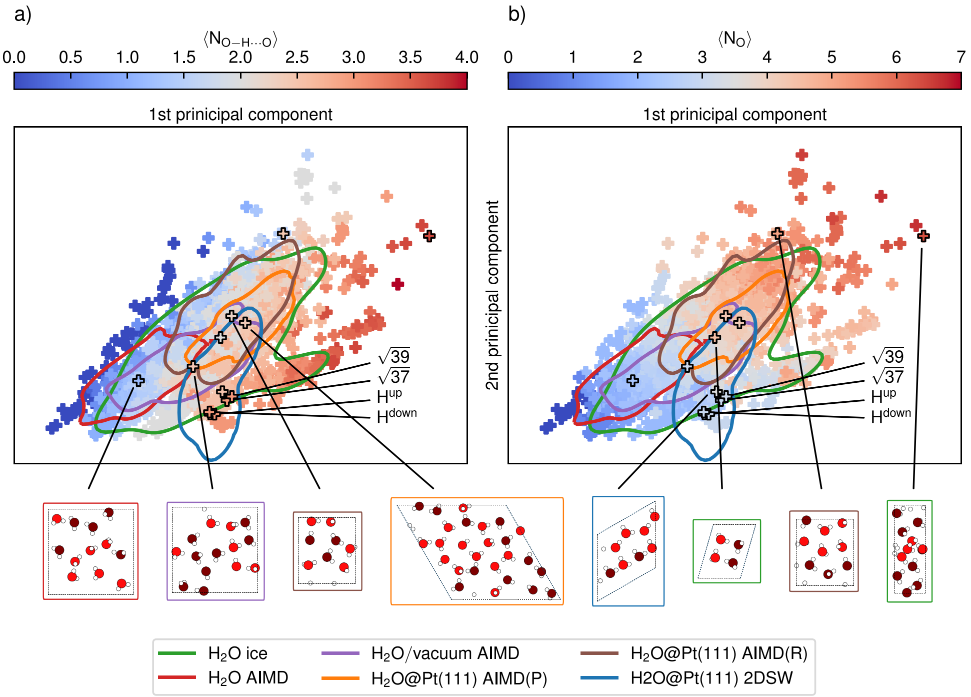

FIG. 2. PCA map for the structure within water layers based on the average SOAP vector (one point corresponds to one structure; cf. Subsection 3 of the Appendix). The datasets are those of Table I, and the color-codings in (a) and (b) correspond to the average number of hydrogen bonds $\langle N_{O\text{-}H\cdots O}\rangle$ as defined in Ref. 16 and the number of nearby oxygen atoms $\langle N_O\rangle$ within a cutoff radius of 4 Å, respectively. The contour lines illustrate the locations of each dataset as obtained via kernel density estimation. For each dataset, we show an exemplary structure as indicated by the frame color.

examples plotted in Fig. 2. Bulk liquid water (H_2O AIMD, red) is mainly located in the low density region at the lower left corner, while water at water–vacuum interfaces (H_2O/vacuum AIMD, violet) and [H_2O@Pt(111) AIMD(P/R), orange/brown] move upward along the diagonal, toward higher density structures. Note that the increase in density (number of nearby oxygens $\langle N_O\rangle$) does not dramatically alter the number of H-bonds $\langle N_{O\text{-}H\cdots O}\rangle$ within the water layer, as can be rationalized from the color codings in Figs. 2(a) and 2(b) and from the reported average values provided in Table II.

TABLE II. Average number of hydrogen bonds $\langle N_{O\text{-}H\cdots O}\rangle$ and number of nearby oxygens $\langle N_O\rangle$ within the cutoff radius of 4 Å per H_2O molecule for each dataset and respective standard deviations in brackets.

Dataset	$\langle N_{O\text{-}H\cdots O}\rangle$	$\langle N_O\rangle$
H_2O ice[68]	1.86(0.88)	3.41(1.38)
H_2O AIMD[72]	1.29(0.45)	2.30(0.51)
H_2O/vacuum AIMD[72]	2.20(0.38)	3.14(0.46)
H_2O@Pt(111) AIMD(P)[21]	2.21(0.21)	4.17(0.41)
H_2O@Pt(111) AIMD(R)[15]	2.19(0.33)	4.17(0.62)
H_2O@Pt(111) ice[54]	3.00(0.00)	3.00(0.03)
H_2O@Pt(111) 2DSW	2.56(0.45)	3.07(0.47)

For comparison, we also marked in Fig. 2 specifically the prototypical low-temperature structures[54]—(hexagonal) $H^{up/down}$ and $\sqrt{37}/\sqrt{39}$—which fall in the region of our static water dataset H_2O@Pt 2DSW, which includes natively hexagonal water layers. It is worth mentioning that the widely used $H^{up/down}$ structures are observed at the extreme boundaries of the configurational space, whereby on average oxygen atoms in $H^{up/down}$ structures form 0.8 more hydrogen bonds than in H_2O@Pt(111) AIMD, as shown in Table II. While there is no overlap between these and the AIMD sampled interface structures on Pt(111) (orange and brown lines), our 2DSW protocol yields at least some overlap. In particular, structures with less hydrogen bonds, which mainly consist of chain-like water arrangements, fall in the region of AIMD results (see also discussion below). These results indicate that ensemble averages based on 2DSW static water structures might approximate AIMD averages more accurately than using only selected low-temperature (e.g., hexagonal) structural models. Interestingly, Le *et al.* pointed out that beyond the first solvation layer, the hydrogen bonding is mainly affected by the water–water interaction rather than the water–metal interaction.[16] This suggests that better results might be achieved by including more water layers in the system.

C. Water layers on Pt(111)

While all 2DSW water structures are provided alongside this work, we show a selection of three obtained structures in Fig. 3,

© Author(s) 2021

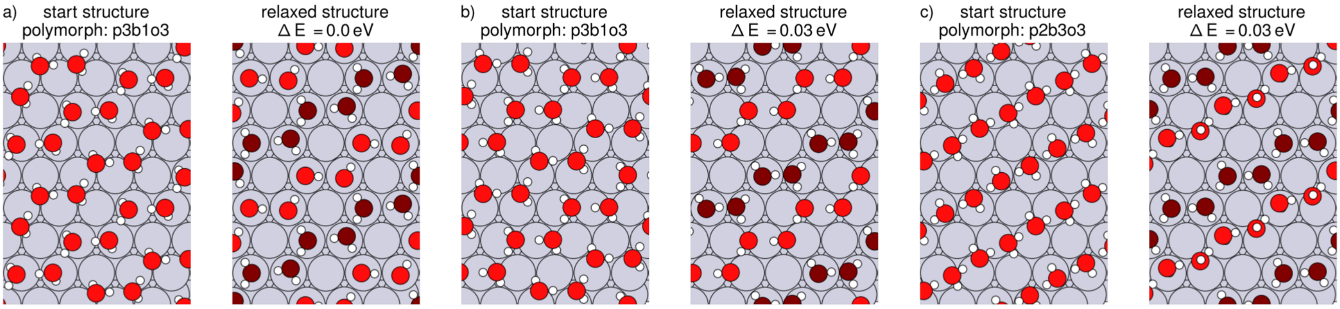

FIG. 3. Selected water–Pt(111) configurations initialized from the p3b1o3 and p2b3o3 polymorphs and their corresponding relaxed structures. (a) The most stable relaxed structure of the whole 2DSW dataset. [(b) and (c)] Two slightly less stable configurations (ΔE = 0.03 eV/H_2O). Oxygen atoms corresponding to flat H_2O molecules are colored by dark red in the relaxed structures.

namely, the lowest energy configuration after relaxation (a) and two local minima [(b) and (c)].

Interestingly, the starting structure of the least stable polymorph p3b1o3 [Fig. 3(a)] leads to the most stable relaxed structure in our set, which is characterized by hexagonal H_2O rings, in which the hydrogen network is distinguished by two chains: one constituted of only H^{down} oriented water molecules and the other chain comprises H_2O molecules parallel to the surface. Here, the structure is stabilized by forming the three hydrogen bonds per oxygen atom as in other ice-like water layers. Furthermore, this structure was also reported by Clabaut *et al.*[54] as the most stable among the hexagonal ice adlayers.

The configuration in Fig. 3(b) is also initialized from the p3b1o3 polymorph, but the start configurations differ from each other in the atomic positions of the water molecules, while Fig. 3(c) started from chain-like water structures. Both relaxed structures in Figs. 3(b) and 3(c) form chains of hexagonal H_2O rings, however, with differing water orientations. Regarding energy, both structures are only 0.03 eV/H_2O less stable relative to the lowest energy configuration [Fig. 3(a)]. Similar chain-structures have been reported for (110) metal surfaces.[53]

In general, our 2DSW protocol yields a variety of hexagonal ring structures comprised of H^{down}, H^{up} oriented water molecules and water molecules parallel to the surface, similarly as shown in Fig. 1(a) at 11 ps in Ref. 51, supporting their importance for simulations in small unit cells.

For the analysis of water layers on the substrate Pt(111), we follow the previous approach and leverage the average SOAP vector as the structural descriptor, this time, however, including specifically the Pt substrate atoms in the atomic environments (see Subsection 3 of the Appendix). Furthermore, we use a SOAP-based average distance measure $\langle \bar{D} \rangle$ to evaluate the structural similarity of a single structure with the AIMD(P) ensemble of interfacial water structures, which we took as our reference (cf. Subsection 3 of the Appendix). The PCA map in Fig. 4 yields similar results as before and illustrates how $\langle \bar{D} \rangle$ (cf. color) is able to measure structural similarity to the reference ensemble. As expected, both AIMD simulations remain close to each other. For the H_2O@Pt(111) ice layers (diamonds), we find a clear trend in distances $\bar{D}$, namely, H^{up} (0.27) > H^{down} ≈ chain-H^{down} > $\sqrt{37} > \sqrt{39}$ (0.21), where the rather large dissimilarity of the hexagonal structures is likely ascribed to the lack of disorder. Similarly as before, our 2DSW ensemble shows better agreement with the AIMD results, although some large dissimilarities $\langle \bar{D} \rangle$ are observed. Further analysis is reported in the supplementary material, where we also analyze other commonly used descriptors of (interfacial) water, such as the atomic density distribution as a function of the distance to the surface and the radial distribution functions within the water adlayers. In general, we find good qualitative agreement in the vertical density profile for the 2DSW ensemble, which is able to reproduce the bimodal oxygen peak structure at the approximately right vertical distance $z_{\text{Pt–O}}$ between slab and bottom-most oxygen atoms {2.2 Å (2DSW) vs 2.0 Å [AIMD(P)]}. However, some differences are observed in the oxygen density profile, e.g., the first peak for AIMD data is wider than the peak for 2DSW, as shown in Fig. S4 of the supplementary material. This can be ascribed to the absence of the dynamic interchange of interfacial water molecules within the solvation layer and with the bulk liquid water.

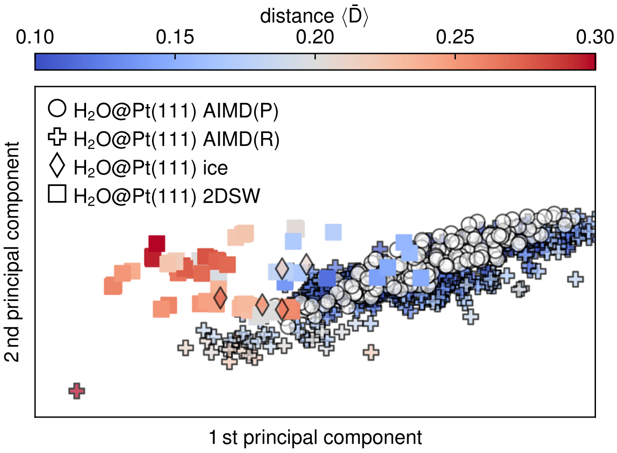

FIG. 4. PCA map for interfacial water structures on Pt(111) with the atomic positions of the substrate Pt atoms included in the SOAP descriptors. Datasets from other sources are highlighted by black edges, and the colors indicate the average SOAP distance $\langle \bar{D} \rangle$ to the AIMD(P) reference dataset, which consists of the colorless circles. (For more details, see the text and Subsection 3 of the Appendix.)

© Author(s) 2021

To this point, we have compared structural similarity to the AIMD(P) reference trajectory; however, we have not yet analyzed how far this influences derived quantities such as average adsorption energies and work function changes, which show a strong structural sensitivity, e.g., to the distance between the metal surface and the water adlayer, as pointed out by Tripkovic *et al.*[25] Similarly, AIMD simulations are comprised of a variety of interfacial water structures due to fluctuating water orientations and ad- and desorption events, which strongly influences the work function due to interfacial charge transfer from the first water layer.[17,18,36] In this regard, Surendralal *et al.* reported values of absolute potentials ranging from 2.5 to roughly 7.5 eV for H_2O@Pt(111) AIMD simulations, which result in an average of 4.86 eV (see the supplementary material in Ref. 81), and it is of interest to see how far 2DSW ensemble averages relate to such AIMD-based reference results. Here, we evaluate the adsorption energy per water molecule as

$$\mathrm{E_{ads}} = \frac{1}{N_{\mathrm{H_2O}}}\Big[\mathrm{E^{DFT}_{H_2O\text{-}Pt}} - \Big(\mathrm{E^{DFT}_{Pt}} + N_{\mathrm{H_2O}}\,\mathrm{E^{DFT}_{H_2O}}\Big)\Big], \tag{1}$$

where $N_{\mathrm{H_2O}}$ is the number of water molecules at the interface and $\mathrm{E^{DFT}_{H_2O\text{-}Pt}}$, $\mathrm{E^{DFT}_{Pt}}$, and $\mathrm{E^{DFT}_{H_2O}}$ are the total energy of the surface with the adsorbed water layer, the energy of a clean surface, and the energy of an isolated water molecule, respectively. The work function change $\Delta\Phi$ due to the adsorption of a water film is determined by the difference in the work function between water-covered and clean slab $\Delta\Phi = \Phi_{\mathrm{H_2O\text{-}Pt}} - \Phi_{\mathrm{Pt}}$, both of which are readily accessible as the position of the Fermi level relative to the electrostatic potential in the vacuum region. We computed the respective quantities for our 2DSW dataset but reanalyzed in the same way the AIMD(P) trajectory with all waters removed except for the first interfacial water layer. Gratifyingly, the so-computed work function reduction $\langle\Delta\Phi\rangle$ for the AIMD(P) trajectory by only the first water layer is identical to the results reported in the original study by Le *et al.*[21] (−1.11 eV here vs −1.1 eV in Ref. 21). This supports once more the major role of only the first water layer.[22,23]

In order to understand better the impact of different possible choices of static interfacial water structures, we studied two specific subsets of our raw 2DSW dataset, which include (i) only configurations with an energy difference $\Delta E \leq 0.05$ eV/H_2O relative to the lowest energy configuration and (ii) configurations with $\langle\bar{D}\rangle < 0.21$. These two subsets are inspired by two typical assumptions in theoretical works, namely, to focus (i) on low energy structures and (ii) on structures that are close to some accurate reference (e.g., experiments or as here more accurate theoretical simulations). Table III summarizes the central properties of the considered structural datasets.

Structurally, the low energy subset (i) exhibits the highest observed number of hydrogen bonds $\langle N_{\mathrm{O\text{-}H\cdots O}}\rangle$, and the number of nearby oxygens $\langle N_{\mathrm{O}}\rangle$ is close to 3, which likely derives from the fact that structural optimization leads to a maximized number of hydrogen bonds within the water layer and maximized number of bonds with the metal surface [cf. most stable configuration in Fig. 3(a)]. Therefore, the structures mainly consist of the hexagonal ($N_{\mathrm{O\text{-}H\cdots O}} = 3$) and some two-dimensional chain structures ($N_{\mathrm{O\text{-}H\cdots O}} = 2.5$). In contrast, the latter subset (ii), which is optimized for structural similarity with the AIMD(P) dataset, is characterized by chain structures, as shown in Fig. 3(b), where the average number of hydrogen bonds (2.23) and the average number of nearby oxygen atoms (3.41) are close to the values of the reference set (cf. Table III and Fig. 4).

For all static water ensembles, we find $\mathrm{E_{ads}}$ values that are significantly lower than the AIMD(P) average, as the latter structures were dynamically sampled with additional bonding partners in the second water layer in the original simulations, which are (artificially) removed in our analysis. Within our dataset, $\mathrm{E_{ads}}$ of the structurally most similar configuration [see Fig. 5(a)] is roughly 0.1 eV higher than the lowest energy configuration. On the other hand, our average adsorption energies fall close to the reported adsorption energies for static water models.[20,52,58,82] While the numerical differences to the AIMD averages are thus evident, a diverse set of local minima configurations as starting points for further investigations, e.g., based on short AIMD simulations or nudged elastic band calculations, might be beneficial for a better understanding of the effects of local water environments on other processes, such as solvation, diffusion, or electrochemical reactions.

In terms of the work function reduction, the better structural agreement of subset (ii) with the AIMD(P) reference dataset does not lead to better agreement in the work function reduction [$\langle\Delta\Phi\rangle = -0.43/-0.30$ eV for 2DSW/subset (ii) vs −1.11 eV for AIMD(P)]. Indeed, the low energy subset (i) performs best with $\langle\Delta\Phi\rangle = -0.83$ eV, which lies within the margin of errors of published AIMD reference results (−1.1 to −0.55 eV[14,21,81]). Note that accurate work functions and work function reductions are relevant for applications in electrochemical contexts as they are directly related to the potential of zero charge of the electrode on an absolute potential scale.[83]

In order to get a better understanding of the correlations between the structural distances $\langle\bar{D}\rangle$, the adsorption energy E_{ads},

TABLE III. Central properties of the (reevaluated) H_2O@Pt(111) AIMD(P) and the 2DSW dataset and of two analyzed subsets: (i) ($\Delta E < 0.05$ eV/H_2O with respect the lowest energy configuration) and (ii) ($\langle\bar{D}\rangle < 0.21$). We report the average number of hydrogen bonds $\langle N_{\mathrm{O\text{-}H\cdots O}}\rangle$, the number of nearby oxygens $\langle N_{\mathrm{O}}\rangle$, the adsorption energies $\langle E_{\mathrm{ads}}\rangle$, the work functions $\langle\Phi_{\mathrm{Pt}}\rangle$ of the bare surfaces, and the work function change $\langle\Delta\Phi\rangle$ due to one water adlayer. The standard deviations as obtained from the study of N_{conf} configurations are reported in parentheses, as well as the estimated uncertainty (standard error of the mean).

	N_{conf}	$\langle N_{\mathrm{O\text{-}H\cdots O}}\rangle$	$\langle N_{\mathrm{O}}\rangle$	$\langle E_{\mathrm{ads}}\rangle$ (eV/H_2O)	$\langle\Phi_{\mathrm{Pt}}\rangle$ (eV)	$\langle\Delta\Phi\rangle$ (eV)
H_2O@Pt(111) AIMD(P)[21]	176	2.21(0.21)	4.17(0.41)	−0.34 ± 0.00(0.03)	5.75 ± 0.00(0.01)	−1.11 ± 0.03(0.33)
H_2O@Pt(111) 2DSW	72	2.56(0.45)	3.07(0.47)	−0.51 ± 0.01(0.05)	5.77 ± 0.00(0.01)	−0.43 ± 0.09(0.76)
H_2O@Pt(111) $\mathrm{2DSW_{(i)}}[\Delta E < 0.05\ \mathrm{eV/H_2O}]$	21	2.83(0.24)	2.93(0.17)	−0.58 ± 0.00(0.01)	5.76 ± 0.00(0.00)	−0.84 ± 0.13(0.60)
H_2O@Pt(111) $\mathrm{2DSW_{(ii)}}[\langle\bar{D}\rangle < 0.21]$	22	2.23(0.29)	3.41(0.44)	−0.49 ± 0.01(0.05)	5.77 ± 0.00(0.01)	−0.30 ± 0.10(0.48)

© Author(s) 2021

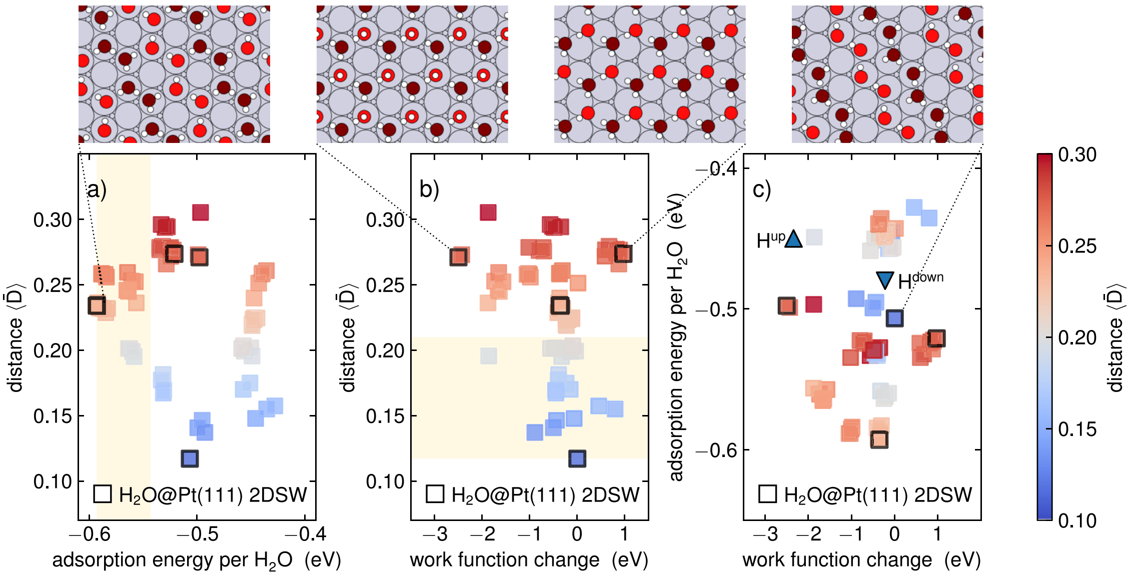

FIG. 5. (a)–(c) The correlations between the average SOAP distance $\langle\bar{D}\rangle$, adsorption energy per H_2O, and work function change for the 2DSW dataset reveal a complex structure–property relationship for interfacial water on Pt(111). The beige areas in (a) and (b) correspond to our selection criteria for subsets (i) and (ii) of the 2DSW dataset, respectively. Triangular data points correspond to hexagonal H^{down} and H^{up} ice layers from Ref. 50.

and the work function change $\Delta\Phi$, we plot an according analysis of the complete 2DSW dataset in Fig. 5. The beige areas in Figs. 5(a) and 5(b) correspond to our selection criteria for subsets (i) and (ii), respectively. Consistent with the described lower stability of dynamical water structures, we also observe here that the best matching structures (blue) are higher in energy [~0.1 eV, Fig. 5(a)]. At the same time, at these E_{ads} values, the distance measure $\langle\bar{D}\rangle$ seems to exhibit a bimodal distribution, thus also incorporating a significant amount of structures with maximal $\langle\bar{D}\rangle$ values. The observed work function change $\Delta\Phi$ exhibits a rather large spread [Fig. 5(b)], which is slightly larger at higher $\langle\bar{D}\rangle$ values. Indeed, structures with different $\langle\bar{D}\rangle$ values can still exhibit similar energies and work function change [Fig. 5(c)], indicating a high degree of complexity for the studied structure–property relationships, providing renewed evidence for the difficulty in treating SLIs, in particular water–metal surfaces with simplified, e.g., individual, static interfacial water models. As energies and work functions are not included in the PCA, the prediction can be a challenging task in some cases as here shown.[84]

IV. DISCUSSION AND CONCLUSIONS

The systematic study of static interfacial water layers on Pt(111) revealed that prototypical, low energy interfacial water structures exhibit quite special orderings and lie rather at the boundaries of the observed configuration space of AIMD simulations. At variance, our 2DSW ensemble, which includes a wide variety of water topologies, does exhibit some more overlap. The main structural discrepancy is the overemphasis of a high number of in-layer H_2O–H_2O bonds for static, single layer water models, which is most prominent for the lowest energy structures (cf. Table III). These differences are, on the one hand, linked to the conceptual differences between local minimum structures and finite temperature MD trajectories and, on the other hand, to the neglect of more water layers in the present work, which can influence the configuration of interfacial water through providing donors and acceptors for hydrogen bonds.[51] Some better structural agreement might be obtained already by extending/substituting the dataset of 2D water start configurations with multilayer water models. Whether an implicit solvent environment[22,23,47,85–87] can appropriately emulate the bonding to the second water layer and whether AIMD simulations of minimal explicit–implicit hybrid models can reproduce results from fully explicit AIMD simulations remain an open question. In particular, similar results would only be expected if the implicit model would stabilize stronger non-H-bond-saturated water structures at the interfaces, e.g., H^{up}, which clarifies the need for such models.

Furthermore, the observed overstructuring of interfacial water might also be influenced by the choice of the substrate supercell, as the studied $\sqrt{12} \times \sqrt{12}$ Pt(111) substrate allows for commensurate hexagonal water orderings. Our protocol thus also provides a starting point for a consistent analysis of such (artificial) periodic boundary effects, which are often discussed, but not yet well understood.

In general, while the work function change and the adsorption energy can vary dramatically for different static water structures, our 2DSW ensemble averages can provide relatively robust averages that show decent correlations with AIMD results, at least trendwise. As many applications still necessitate the study of quasi-static water models, e.g., for evaluating reaction barriers via nudged elastic band methods, these results suggest that ensemble averages over a consistent set of static water structures might provide more robust

© Author(s) 2021

predictions. Indeed, the application of clustering methods to our 2DSW dataset reveals a total number of 11 topologically different prototype structures (see Sec. S.5.A of the supplementary material), which indicates that such an approach would still remain computationally much more feasible than brute-force AIMD-based methods.

Finally, our approach, in particular the implementation as a Python package provided alongside this work, might serve as a good starting point for the study of low-temperature water structures (or other solvents) on other surface supercell sizes and substrate materials or as uncorrelated starting points for AIMD simulations.

SUPPLEMENTARY MATERIAL

See the supplementary material for (i) a discussion about the choice of supercell in the construction protocol, (ii) a description of the in-house algorithm to find water molecules at the interface, (iii) PCA maps for the water configurations by using the local SOAP descriptors, (iv) density profile and O–O radial distribution function plots for $H_2O@Pt(111)$ systems listed in Table I, (v) an overview of the prototype structures found in $H_2O@Pt(111)$ 2DSW, and (vi) further results for Pt(100) and Pt(110) surfaces. For access to the relevant data of this work, see the Data Availability section.

ACKNOWLEDGMENTS

We would like to thank Professor Dr. Jun Cheng and Dr. Hendrik H. Heenen who provided the AIMD(P) and AIMD(R) trajectories, which are related to Refs. 21 and 15, respectively. Furthermore, we want to thank Ambrosio *et al.*, Monserrat *et al.*, and Clabaut *et al.* who made the AIMD trajectories and atomistic structures publicly available alongside their publications, namely, Refs. 72, 68, and 54.

N.G.H. acknowledges financial support through the EuroTech Postdoc Programme, which is co-funded by the European Commission under its framework program Horizon 2020 and Grant Agreement No. 754462, and support from the Deutsche Forschungsgemeinschaft (DFG, German Research Foundation) under Germany's Excellence Strategy—Grant No. EXC 2089/1-390776260. This work was supported by a grant from the Gauss Centre for Supercomputing e.V. (www.gauss-centre.eu) by providing computing time through the John von Neumann Institute for Computing (NIC) on the GCS Supercomputer JUWELS[88] at the Juelich Supercomputing Centre (JSC).

AUTHOR DECLARATIONS

Conflict of Interest

The authors have no conflicts to declare.

Author Contributions

A.C.D.L and T.E. contributed equally to this work.

DATA AVAILABILITY

The data that support the findings of this study are available within the article and its supplementary material or from the original publications (cf. Acknowledgments). The newly generated $H_2O@Pt$ 2DSW structural dataset and Python codes (analysis and determination of interface water molecules) are openly available at https://dx.doi.org/10.17617/3.7c. A Python implementation of the 2DSW protocol is available as an open-source Python package at https://github.com/computationalelectrochemistrygroup/WaterStructureCreator.

APPENDIX: METHODS

1. Determination of interfacial water molecules

Interfacial water layers at (artificially created or naturally present) water–vacuum interfaces are selected by first determining all interfacial O atoms and then adding all chemically bound H atoms (bond cutoff = 1.2 Å). Interfacial O atoms are determined via the following algorithm that is inspired from the definition of quantum mechanical cavities in the context of implicit solvation methods:[89,90]

(a) Define the water-filled region Ω by superimposing soft spheres localized on the atoms with given radius r_0 and that smooth decay from a value of 1 within the sphere to 0 outside it. Evaluate the so-obtained filling function Ω on a numerical grid and renormalize all values $\Omega > 1$ to 1.

(b) Estimate the surface of Ω by computing the numerical derivative $\mathbf{S} = \nabla\Omega$, and define a grid point i as an interfacial grid points i_S whenever

$$\|\mathbf{S}_{i_S}\| \geq \tau \max_i \|\mathbf{S}_i\|, \quad \tau < 1. \tag{A1}$$

(c) Interface atoms are given by the set of closest oxygen atoms to the real space positions $\{\mathbf{r}_{i_S}\}$ of all interface grid points.

More details, e.g., on the numerical implementation in periodic boundary conditions and chosen numerical parameters (e.g., r_0, τ) are provided in the supplementary material.

2. Computational details

Periodic DFT calculations are performed with the Quantum ESPRESSO package[91] (PWscf) and the Perdew–Burke–Ernzerhof-generalized gradient approximation (PBE-GGA)[74] for the exchange–correlation energy functional. All atoms are represented by ultrasoft pseudopotentials from the open-source GBRV library[92] with density and wave function cutoffs of 360and45 Ry, respectively. The water films, modeled with eight H_2O molecules, are placed on side of the surface, and a dipole correction as implemented in ENVIRON[85] is applied. The Pt surfaces are simulated by using a (3×3) supercell with three layers for Pt(100), a (3×2) supercell with four layers for Pt(110), and a $(\sqrt{12} \times \sqrt{12})R30°$ supercell with three layers for Pt(111). The two bottommost metal layers are fixed at their ideal bulk positions. Slabs are separated by ≈17 Å. Geometry optimizations are carried through until the forces on all relaxed atoms were smaller than 0.1 eV $Å^{-1}$. Brillouin zone integrations are performed using Γ-centered Monkhorst–Pack meshes of $(4 \times 4 \times 1)$ and a Marzari–Vanderbilt smearing of 0.02 Ry.

Single point calculations of the interfacial water on Pt(111) for the AIMD simulation from the work of Le *et al.*[21] were performed with the same settings, except that a $(2 \times 2 \times 1)$ k-point grid was used. The symmetric setup of the original AIMD was split in two

© Author(s) 2021

asymmetric setups with three layers of platinum each. The bottom half was rotated by 180° around the y axis to have the same orientation for both sides. No further manipulations were performed on the cell or positions of the atoms.

3. Structural similarity measures

We selected the local structure descriptor SOAP[57] as implemented in the Dscribe package[79] and as similarly performed for 3D periodic water structures[68] for the representation of the atomic environment. The local environment $\mathcal{X}$ around an atom is modeled by summing over Gaussians centered on each atom i in the structure within a cutoff, yielding the density $\rho_{\mathcal{X}}(r)$. After expansion of the density in a basis of orthonormal radial functions $g_b(|r|)$ and spherical harmonics $Y_{lm}(\hat{r})$, the power spectrum $\mathbf{p}(\mathcal{X})_{b_1 b_2 l}$ can be expressed in terms of expansion coefficients c_{blm} as

$$\rho_{\mathcal{X}}(r) = \sum_{i\in\mathcal{X}} \exp\left(-\frac{(x_i - r)^2}{2\sigma^2}\right), \tag{A2}$$

$$\rho_{\mathcal{X}}(r) = \sum_{blm} c_{blm} g_b(|r|) Y_{lm}(\hat{r}), \tag{A3}$$

$$\mathbf{p}(\mathcal{X})_{b_1 b_2 l} = \pi\sqrt{\frac{8}{2l+1}}\sum_m (c_{b_1 lm})^\dagger c_{b_2 lm}. \tag{A4}$$

The c_{blm} coefficients form the components of an abstract SOAP descriptor vector, which is conveniently used for measuring structural similarity throughout this work.

For the analysis of the internal structure of water layers, we evaluate the SOAP vectors centered on the oxygen atoms, including neighboring H and O atoms up to a cutoff radius of 4 Å. For the analysis of water layers on top of Pt(111), we also include the substrate Pt positions in the environment within the sphere defined by the cutoff. In both cases, crossover terms between different atomic species in the power spectrum were allowed to include the information of hydrogen and, in the later case, platinum as well. A description of the entire system was obtained by using the inner average of the SOAP vectors.[79] The hyperparameters for computing the SOAP descriptors used throughout this work are $n_{\max} = 8$, $l_{\max} = 8$, $\sigma = 0.3$, and $r_{\text{cutoff}} = 4$ Å.

For comparing the structural similarity of single structures A with a reference structure B, we use the average distance $\bar{D}$[93] as given by the average kernel $\bar{K}$[93] and defined by

$$\bar{D}(\mathrm{A},\mathrm{B}) = \sqrt{2 - 2\,\bar{K}(\mathrm{A},\mathrm{B})}, \tag{A5}$$

$$\bar{K}(\mathrm{A},\mathrm{B}) = \left[\frac{1}{N}\sum_i \mathbf{p}(\mathcal{X}_i^{\mathrm{A}})\right]\cdot\left[\frac{1}{M}\sum_j \mathbf{p}(\mathcal{X}_j^{\mathrm{B}})\right], \tag{A6}$$

where N and M are the number of atoms in structures A and B, respectively. The so-obtained distance measure $\bar{\mathrm{D}}$ is subsequently averaged over all structures in the reference dataset to obtain an average structural dissimilarity measure $\langle\bar{D}\rangle$ with the reference ensemble, which we call shortly *average SOAP distance*, here. In the present work, the reference ensemble was created by taking snapshots every 0.1 ps from the AIMD(P) trajectory[21] that was provided by Cheng.

REFERENCES

[1] X. Guo, S. Gin, and G. S. Frankel, npj Mater. Degrad. **4**, 34 (2020).

[2] J. H. Stenlid, E. C. Dos Santos, A. Bagger, A. J. Johansson, J. Rossmeisl, and L. G. M. Pettersson, J. Phys. Chem. C **124**, 469 (2020).

[3] J. K. Nørskov, J. Rossmeisl, A. Logadottir, L. Lindqvist, J. R. Kitchin, T. Bligaard, and H. Jónsson, J. Phys. Chem. B **108**, 17886 (2004).

[4] J. K. Nørskov, T. Bligaard, J. Rossmeisl, and C. H. Christensen, Nat. Chem. **1**, 37 (2009).

[5] N. G. Hörmann, M. Jäckle, F. Gossenberger, T. Roman, K. Forster-Tonigold, M. Naderian, S. Sakong, and A. Groß, J. Power Sources **275**, 531 (2015).

[6] Z. W. Seh, J. Kibsgaard, C. F. Dickens, I. Chorkendorff, J. K. Nørskov, and T. F. Jaramillo, Science **355**, eaad4998 (2017).

[7] P. Fenter and N. C. Sturchio, Prog. Surf. Sci. **77**, 171 (2004).

[8] O. Björneholm, M. H. Hansen, A. Hodgson, L.-M. Liu, D. T. Limmer, A. Michaelides, P. Pedevilla, J. Rossmeisl, H. Shen, G. Tocci, E. Tyrode, M.-M. Walz, J. Werner, and H. Bluhm, Chem. Rev. **116**, 7698 (2016).

[9] O. Andreussi, F. Nattino, and N. G. Hörmann, in *Atomic-Scale Modelling of Electrochemical Systems*, edited by M. Melander, T. Laurila, and K. Laasonen (John Wiley & Sons Ltd., 2020).

[10] K. Schwarz and R. Sundararaman, Surf. Sci. Rep. **75**, 100492 (2020).

[11] L. S. Pedroza, A. Poissier, and M.-V. Fernández-Serra, J. Chem. Phys. **142**, 034706 (2015).

[12] S. K. Natarajan and J. Behler, Phys. Chem. Chem. Phys. **18**, 28704 (2016).

[13] L. Bellarosa, R. García-Muelas, G. Revilla-López, and N. López, ACS Cent. Sci. **2**, 109 (2016).

[14] S. Sakong and A. Groß, J. Chem. Phys. **149**, 084705 (2018).

[15] H. H. Heenen, J. A. Gauthier, H. H. Kristoffersen, T. Ludwig, and K. Chan, J. Chem. Phys. **152**, 144703 (2020).

[16] J.-B. Le, A. Cuesta, and J. Cheng, J. Electroanal. Chem. **819**, 87 (2018).

[17] J.-B. Le, Q.-Y. Fan, J.-Q. Li, and J. Cheng, Sci. Adv. **6**, eabb1219 (2020).

[18] J.-B. Le, A. Chen, L. Li, J.-F. Xiong, J. Lan, Y.-P. Liu, M. Iannuzzi, and J. Cheng, JACS Au **1**, 569 (2021).

[19] Z. K. Goldsmith, M. F. Calegari Andrade, and A. Selloni, Chem. Sci. **12**, 5865 (2021).

[20] A. Hodgson and S. Haq, Surf. Sci. Rep. **64**, 381 (2009).

[21] J.-B. Le, M. Iannuzzi, A. Cuesta, and J. Cheng, Phys. Rev. Lett. **119**, 016801 (2017).

[22] L. Blumenthal, J. M. Kahk, R. Sundararaman, P. Tangney, and J. Lischner, RSC Adv. **7**, 43660 (2017).

[23] N. G. Hörmann, Z. Guo, F. Ambrosio, O. Andreussi, A. Pasquarello, and N. Marzari, npj Comput. Mater. **5**, 100 (2019).

[24] R. Jinnouchi and A. B. Anderson, Phys. Rev. B **77**, 245417 (2008).

[25] V. Tripkovic, M. E. Björketun, E. Skúlason, and J. Rossmeisl, Phys. Rev. B **84**, 115452 (2011).

[26] T. Ludwig, J. A. Gauthier, K. S. Brown, S. Ringe, J. K. Nørskov, and K. Chan, J. Phys. Chem. C **123**, 5999 (2019).

[27] J. Park and L. T. Roling, AIChE J. **66**, e17036 (2020).

[28] S. Schnur and A. Groß, Catal. Today **165**, 129 (2011).

[29] S. Sakong, K. Forster-Tonigold, and A. Groß, J. Chem. Phys. **144**, 194701 (2016).

[30] D. T. Limmer, A. P. Willard, P. Madden, and D. Chandler, Proc. Natl. Acad. Sci. U. S. A. **110**, 4200 (2013).

[31] A. P. Willard, D. T. Limmer, P. A. Madden, and D. Chandler, J. Chem. Phys. **138**, 184702 (2013).

[32] S. N. Steinmann, R. Ferreira De Morais, A. W. Götz, P. Fleurat-Lessard, M. Iannuzzi, P. Sautet, and C. Michel, J. Chem. Theory Comput. **14**, 3238 (2018).

[33] S. Sakong and A. Groß, Phys. Chem. Chem. Phys. **22**, 10431 (2020).

[34] H. H. Kristoffersen, T. Vegge, and H. A. Hansen, Chem. Sci. **9**, 6912 (2018).

[35] A. Bouzid and A. Pasquarello, J. Phys. Chem. Lett. **9**, 1880 (2018).

[36] X.-Y. Li, A. Chen, X.-H. Yang, J.-X. Zhu, J.-B. Le, and J. Cheng, J. Phys. Chem. Lett. **12**, 7299 (2021).

[37] G. S. Karlberg, Phys. Rev. B **74**, 153414 (2006).

© Author(s) 2021

[38] J. Rossmeisl, J. Greeley, and G. Karlberg, "Electrocatalysis and catalyst screening from density functional theory calculations," in *Fuel Cell Catalysis* (John Wiley & Sons Ltd., 2008), Chap. 3, pp. 57–92.

[39] M. E. Björketun, Z. Zeng, R. Ahmed, V. Tripkovic, K. S. Thygesen, and J. Rossmeisl, Chem. Phys. Lett. **555**, 145 (2013).

[40] Z.-D. He, S. Hanselman, Y.-X. Chen, M. T. M. Koper, and F. Calle-Vallejo, J. Phys. Chem. Lett. **8**, 2243 (2017).

[41] Q. Zhang and A. Asthagiri, Catal. Today **323**, 35 (2019).

[42] E. Skúlason, G. S. Karlberg, J. Rossmeisl, T. Bligaard, J. Greeley, H. Jónsson, and J. K. Nørskov, Phys. Chem. Chem. Phys. **9**, 3241 (2007).

[43] S. A. Akhade, N. J. Bernstein, M. R. Esopi, M. J. Regula, and M. J. Janik, Catal. Today **288**, 63 (2017).

[44] J. Rossmeisl, E. Skúlason, M. E. Björketun, V. Tripkovic, and J. K. Nørskov, Chem. Phys. Lett. **466**, 68 (2008).

[45] K. Chan and J. K. Nørskov, J. Phys. Chem. Lett. **6**, 2663 (2015).

[46] J. A. Gauthier, C. F. Dickens, H. H. Heenen, S. Vijay, S. Ringe, and K. Chan, J. Chem. Theory Comput. **15**, 6895 (2019).

[47] G. Kastlunger, P. Lindgren, and A. A. Peterson, J. Phys. Chem. C **122**, 12771 (2018).

[48] J. Hussain, H. Jónsson, and E. Skúlason, ACS Catal. **8**, 5240 (2018).

[49] J. Hussain, H. Jónsson, and E. Skúlason, Faraday Discuss. **195**, 619 (2016).

[50] S. Schnur and A. Groß, New J. Phys. **11**, 125003 (2009).

[51] T. Roman and A. Groß, Catal. Today **202**, 183 (2013).

[52] S. Meng, E. G. Wang, and S. Gao, Phys. Rev. B **69**, 195404 (2004).

[53] J. Carrasco, A. Hodgson, and A. Michaelides, Nat. Mater. **11**, 667 (2012).

[54] P. Clabaut, R. Staub, J. Galiana, E. Antonetti, and S. N. Steinmann, J. Chem. Phys. **153**, 054703 (2020).

[55] S. Standop, A. Redinger, M. Morgenstern, T. Michely, and C. Busse, Phys. Rev. B **82**, 161412 (2010).

[56] A. Groß, F. Gossenberger, X. Lin, M. Naderian, S. Sakong, and T. Roman, J. Electrochem. Soc. **161**, E3015 (2014).

[57] A. P. Bartók, R. Kondor, and G. Csányi, Phys. Rev. B **87**, 184115 (2013).

[58] K. Tonigold and A. Gross, J. Comput. Chem. **33**, 695 (2012).

[59] A. Massey, F. McBride, G. R. Darling, M. Nakamura, and A. Hodgson, Phys. Chem. Chem. Phys. **16**, 24018 (2014).

[60] T. Roman and A. Groß, J. Phys. Chem. C **120**, 13649 (2016).

[61] J. Chen, G. Schusteritsch, C. J. Pickard, C. G. Salzmann, and A. Michaelides, Phys. Rev. Lett. **116**, 025501 (2016).

[62] F. Corsetti, P. Matthews, and E. Artacho, Sci. Rep. **6**, 18651 (2016).

[63] F. Corsetti, J. Zubeltzu, and E. Artacho, Phys. Rev. Lett. **116**, 085901 (2016).

[64] S. P. Ong, W. D. Richards, A. Jain, G. Hautier, M. Kocher, S. Cholia, D. Gunter, V. L. Chevrier, K. A. Persson, and G. Ceder, Comput. Mater. Sci. **68**, 314 (2013).

[65] R. Tran, Z. Xu, B. Radhakrishnan, D. Winston, W. Sun, K. A. Persson, and S. P. Ong, Sci. Data **3**, 160080 (2016).

[66] W. Sun and G. Ceder, Surf. Sci. **617**, 53 (2013).

[67] A. Zur and T. C. McGill, J. Appl. Phys. **55**, 378 (1984).

[68] B. Monserrat, J. G. Brandenburg, E. A. Engel, and B. Cheng, Nat. Commun. **11**, 5757 (2020).

[69] Y. Zhang and W. Yang, Phys. Rev. Lett. **80**, 890 (1998).

[70] C. Adamo and V. Barone, J. Chem. Phys. **110**, 6158 (1999).

[71] S. Grimme, A. Hansen, J. G. Brandenburg, and C. Bannwarth, Chem. Rev. **116**, 5105 (2016).

[72] F. Ambrosio, Z. Guo, and A. Pasquarello, J. Phys. Chem. Lett. **9**, 3212 (2018).

[73] G. Miceli, S. de Gironcoli, and A. Pasquarello, J. Chem. Phys. **142**, 034501 (2015).

[74] J. P. Perdew, K. Burke, and M. Ernzerhof, Phys. Rev. Lett. **77**, 3865 (1996).

[75] S. Grimme, J. Antony, S. Ehrlich, and H. Krieg, J. Chem. Phys. **132**, 154104 (2010).

[76] S. Grimme, Wiley Interdiscip. Rev.: Comput. Mol. Sci. **1**, 211 (2011).

[77] B. Hammer, L. B. Hansen, and J. K. Nørskov, Phys. Rev. B **59**, 7413 (1999).

[78] J. Klimeš, D. R. Bowler, and A. Michaelides, J. Phys.: Condens. Matter **22**, 022201 (2009).

[79] L. Himanen, M. O. J. Jäger, E. V. Morooka, F. Federici Canova, Y. S. Ranawat, D. Z. Gao, P. Rinke, and A. S. Foster, Comput. Phys. Commun. **247**, 106949 (2020).

[80] F. Pedregosa, G. Varoquaux, A. Gramfort, V. Michel, B. Thirion, O. Grisel, M. Blondel, P. Prettenhofer, R. Weiss, V. Dubourg, J. Vanderplas, A. Passos, D. Cournapeau, M. Brucher, M. Perrot, and E. Duchesnay, J. Mach. Learn. Res. **12**, 2825 (2011).

[81] S. Surendralal, M. Todorova, and J. Neugebauer, Phys. Rev. Lett. **126**, 166802 (2021).

[82] J. Carrasco, J. Klimeš, and A. Michaelides, J. Chem. Phys. **138**, 024708 (2013).

[83] S. Trasatti, Electrochim. Acta **35**, 269 (1990).

[84] B. Cheng, R.-R. Griffiths, S. Wengert, C. Kunkel, T. Stenczel, B. Zhu, V. L. Deringer, N. Bernstein, J. T. Margraf, K. Reuter, and G. Csanyi, Acc. Chem. Res. **53**, 1981 (2020).

[85] O. Andreussi, I. Dabo, and N. Marzari, J. Chem. Phys. **136**, 064102 (2012).

[86] O. Andreussi and G. Fisicaro, Int. J. Quantum Chem. **119**, e25725 (2019).

[87] N. G. Hörmann, O. Andreussi, and N. Marzari, J. Chem. Phys. **150**, 041730 (2019).

[88] Jülich Supercomputing Centre, J. Large-Scale Res. Facil. **5**, A135 (2019).

[89] G. Fisicaro, L. Genovese, O. Andreussi, S. Mandal, N. N. Nair, N. Marzari, and S. Goedecker, J. Chem. Theory Comput. **13**, 3829 (2017).

[90] O. Andreussi, N. G. Hörmann, F. Nattino, G. Fisicaro, S. Goedecker, and N. Marzari, J. Chem. Theory Comput. **15**, 1996 (2019).

[91] P. Giannozzi, O. Andreussi, T. Brumme, O. Bunau, M. Buongiorno Nardelli, M. Calandra, R. Car, C. Cavazzoni, D. Ceresoli, M. Cococcioni, N. Colonna, I. Carnimeo, A. Dal Corso, S. de Gironcoli, P. Delugas, R. A. DiStasio, A. Ferretti, A. Floris, G. Fratesi, G. Fugallo, R. Gebauer, U. Gerstmann, F. Giustino, T. Gorni, J. Jia, M. Kawamura, H.-Y. Ko, A. Kokalj, E. Küçükbenli, M. Lazzeri, M. Marsili, N. Marzari, F. Mauri, N. L. Nguyen, H.-V. Nguyen, A. Otero-de-la-Roza, L. Paulatto, S. Poncé, D. Rocca, R. Sabatini, B. Santra, M. Schlipf, A. P. Seitsonen, A. Smogunov, I. Timrov, T. Thonhauser, P. Umari, N. Vast, X. Wu, and S. Baroni, J. Phys.: Condens. Matter **29**, 465901 (2017).

[92] K. F. Garrity, J. W. Bennett, K. M. Rabe, and D. Vanderbilt, Comput. Mater. Sci. **81**, 446 (2014).

[93] S. De, A. P. Bartók, G. Csányi, and M. Ceriotti, Phys. Chem. Chem. Phys. **18**, 13754 (2016).

© Author(s) 2021

Paper 2

Cavity formation at metal-water interfaces

Thorben Eggert, Nicolas G. Hörmann, and Karsten Reuter

J. Chem. Phys. **2023**, *159*, 194702.

Reprinted under the terms of the Creative Commons Attribution License (CC BY 4.0).
© 2023 The Authors. The Journal of Chemical Physics published by American Institute of Physics

The Journal of Chemical Physics

RESEARCH ARTICLE | NOVEMBER 15 2023

Cavity formation at metal–water interfaces

Thorben Eggert ; Nicolas G. Hörmann ; Karsten Reuter

Check for updates

J. Chem. Phys. 159, 194702 (2023)
https://doi.org/10.1063/5.0167406

View Online
Export Citation
CrossMark

15 November 2023 11:25:32

AIP Publishing

The Journal of Chemical Physics

ARTICLE

pubs.aip.org/aip/jcp

Cavity formation at metal–water interfaces

Cite as: J. Chem. Phys. **159**, 194702 (2023); doi: 10.1063/5.0167406
Submitted: 12 July 2023 • Accepted: 26 October 2023 •
Published Online: 15 November 2023

View Online Export Citation CrossMark

Thorben Eggert,[1,2] Nicolas G. Hörmann,[1,a)] and Karsten Reuter[1]

AFFILIATIONS

[1] Fritz-Haber-Institut der Max-Planck-Gesellschaft, Faradayweg 4-6, 14195 Berlin, Germany
[2] Chair of Theoretical Chemistry and Catalysis Research Center, Technische Universität München, Lichtenbergstr. 4, 85748 Garching, Germany

[a)] Author to whom correspondence should be addressed: hoermann@fhi.mpg.de

ABSTRACT

The free energy cost of forming a cavity in a solvent is a fundamental concept in rationalizing the solvation of molecules and ions. A detailed understanding of the factors governing cavity formation in bulk solutions has *inter alia* enabled the formulation of models that account for this contribution in coarse-grained implicit solvation methods. Here, we employ classical molecular dynamics simulations and multistate Bennett acceptance ratio free energy sampling to systematically study cavity formation at a wide range of metal–water interfaces. We demonstrate that the obtained size- and position-dependence of cavitation energies can be fully rationalized by a geometric Gibbs model, which considers that the creation of the metal–cavity interface necessarily involves the removal of interfacial solvent. This so-called competitive adsorption effect introduces a substrate dependence to the interfacial cavity formation energy that is missed in existing bulk cavitation models. Using expressions from scaled particle theory, this substrate dependence is quantitatively reproduced by the Gibbs model through simple linear relations with the adsorption energy of a single water molecule. Besides providing a better general understanding of interfacial solvation, this paves the way for the derivation and efficient parametrization of more accurate interface-aware implicit solvation models needed for reliable high-throughput calculations toward improved electrocatalysts.

© 2023 Author(s). All article content, except where otherwise noted, is licensed under a Creative Commons Attribution (CC BY) license (http://creativecommons.org/licenses/by/4.0/). https://doi.org/10.1063/5.0167406

15 November 2023 11:25:32

I. INTRODUCTION

Atomistically resolved simulations of liquids are particularly challenging due to the simultaneous presence of dynamic disorder and significant chemical interactions, such as H-bonding networks in aqueous solutions.[1–4] In particular, when it comes to solvation, there is, therefore, a long-standing tradition to replace explicit dynamical simulations with a statistically relevant number of solvent molecules through computationally more efficient coarse-grained simulations. The corresponding implicit solvation approaches then embed the finite, atomically resolved solute (molecule or ion) into a solvent region that, in the simplest case, is merely described as a dielectric continuum.[5,6] Not least from the angle of such implicit solvation models, cavity formation and concomitant cavity formation energies thus emerge as fundamental concepts in the general understanding of solvation. The latter energies denote the free energy cost of creating an excluded volume V_{cav} in the solvent that can then be occupied by the solute.

At a constant pressure, the cavitation free energy arises simply from the created internal interface between the solvent at the outside and vacuum at the inside of the cavity. It, therefore, scales naturally with the surface area of the cavity A_{cav}, with a liquid–cavity (LC) surface tension γ_{LC} as a proportionality factor,

$$F_{\mathrm{cav,\,bulk}} = \gamma_{\mathrm{LC}} A_{\mathrm{cav}}. \tag{1}$$

For large enough cavities, this proportionality factor is the macroscopic liquid–vapor (LV) surface tension, $\gamma_{\mathrm{LC}} \to \gamma_{\mathrm{LV}}$ for $A_{\mathrm{cav}} \to \infty$.[7–9] For smaller cavities, γ_{LC} is generally size-dependent. Within scaled particle theory (SPT), this size dependency can be derived rigorously for spherical cavities and expressed as a polynomial expansion in the cavity radius.[8,10,11] For small cavities, the thus approximately linear scaling of γ_{LC} with radius leads then overall to an approximate cubic scaling of $F_{\mathrm{cav,\,bulk}}$ with radius, i.e., $F_{\mathrm{cav,\,bulk}} \propto V_{\mathrm{cav}}$ for $V_{\mathrm{cav}} \to 0$.[7–9,12–15] As a result, it is not surprising that appropriately parametrized, effective continuum solvation models that use area and/or volume scaling to approximate $F_{\mathrm{cav,\,bulk}}$[6,11,16,17] succeed in accurately reproducing experimental solvation energies of different species in aqueous[16,17] and non-aqueous[18,19] bulk solvent environments.

More recently, according models have been applied to study the stability of adsorbates at extended solid–liquid interfaces (SLIs), for which an accurate account of solvation effects is generally critical to reach the predictive accuracy necessary to develop, for example, improved electrocatalysts.[20–23] Unfortunately, however, the present bulk continuum models fail to reach this desired accuracy in the description of solvation at such interfaces.[20–24] One evident source of error is that these models are agnostic to competitive adsorption.[20,23,25,26] The latter describes the necessity to remove specifically bound solvent molecules from the surface to create space for the adsorbate. This is more difficult at strongly binding surfaces, and cavity formation should thus depend on the interaction strength between substrate and solvent.[24] Instead, the existing bulk parametrizations only consider the scaling with the overall cavity area and/or volume.

To quantify the energetic contribution of competitive adsorption and derive simple models for cavity formation at SLIs, we here employ free energy sampling methods for cavity formation at various metal–water interfaces using classical molecular dynamics (MD) simulations. By screening different sizes and distances of the cavity to the substrate, we obtain effective interface tensions for each SLI. We find that these correlate with the adsorption energy of an individual water molecule on a substrate, in agreement with the concept of competitive adsorption. Cast into a simple geometric Gibbs model, which accounts for the introduced and removed interfaces, these results provide the basis for the efficient parameterization of an interface-aware general cavity formation model. They also rationalize why competitive adsorption effects are, in some cases, less important than expected and where their account in atomistic SLI simulations will be critical.

II. METHODS

Our systematic MD simulations employ the SPC model (CVFF) for water[27] and classical metal–water potentials (12-6 Lennard-Jones) by Heinz and co-workers[28] to investigate eight different Me(111)–water SLIs (Me = Pt, Ni, Pd, Cu, Au, Ag, Al, and Pb) that cover a wide range of interaction strengths and thus competitive adsorption effects. The atomic structures were managed with the atomic simulation environment (ASE),[29] and the initial water slabs were created with Packmol.[30] The simulation cell contains a four-layer metal(111) slab with a (12×12) surface unit cell. The two lowest layers were fixed to their initial positions. A 25 Å thick water film above one side of the slab is followed by 20 Å wide vacuum on both sides. The simulations were performed with Large-scale Atomic/Molecular Massively Parallel Simulator (LAMMPS)[31] in a canonical ensemble (NVT) at 300 K, which yields cavity formation energies without pressure contributions since the water volume can freely readjust upon the creation of the cavity. The lattice constants and the number of water molecules for each system are reported in Table S1 of the supplementary material.

Cavities were modeled as soft spheres and interacted only with the oxygen atoms of water via a Weeks–Chandler–Andersen potential,[32]

$$U(r) = \begin{cases} 4\varepsilon \times \left[\left(\frac{\sigma}{r}\right)^{12} - \left(\frac{\sigma}{r}\right)^{6}\right] + \varepsilon, & r \le 2^{1/6}\sigma, \\ 0, & r > 2^{1/6}\sigma, \end{cases} \tag{2}$$

which is a shifted and truncated Lennard-Jones potential; cf. Fig. S5 of the supplementary material.

It approaches zero smoothly at the cutoff $r_{\mathrm{cut}} = 2^{1/6}\sigma$. The corresponding radius of a hard sphere was obtained through a Boltzmann factor criterion as $U(r = r_{\mathrm{cav}}) = k_B T$.[33] We set $r_{\mathrm{cav}} = r_{\mathrm{cut}} - 0.5$Å for the different runs. Seven equally spaced cavity sizes r_{cav} between 2.5 and 5.5 Å were investigated in this study, and the lateral position of the cavity center was fixed to be above a top site. The z-coordinate of the cavity center was varied between $z_{\mathrm{top}} - r_{\mathrm{cut}}$ and $z_{\mathrm{top}} + r_{\mathrm{cut}} + 10$Å, where z_{top} is the position of the uppermost metal layer. Within this range, independent NVT-MDs runs were performed at every 0.25 Å at 300 K. The first 100 ps was used to equilibrate the system, and further 200 ps was used for data production. Atomic positions were saved every 1 ps. Ultimately, the free energy differences between all runs of one metal–water interface were calculated via MBAR as implemented in pymbar,[34]

$$\hat{f}_i = -\ln \sum_{j=1}^{K} \sum_{n=1}^{N_j} \frac{\exp\left[-u_i(x_{jn})\right]}{\sum_{k=1}^{K} N_k \exp\left[\hat{f}_k - u_k(x_{jn})\right]}, \tag{3}$$

where K denotes the thermodynamic states, N_j denote the uncorrelated equilibrium samples, u is the reduced potential, x denotes the atomic positions, and the index i is the state of interest. The equation is solved self-consistently for the dimensionless free energy $\hat{f}_i$, and then, all states are referenced to the initial state to obtain the free energy difference. This requires the calculation of the reduced (dimensionless) energy of all trajectories for one system with all possible cavity sizes and positions.

15 November 2023 11:25:32

III. RESULTS AND DISCUSSION

A. Size dependence of cavitation energies at metal–water interfaces

Previous studies on the cavity formation energy on metal–water interfaces relied on particle insertion to access the spatially resolved free energy.[35,36] However, this approach is limited by the probability of finding cavities in an MD simulation, which becomes increasingly unlikely for larger ones. To drive the system to create larger cavities, they need to be explicitly included in the MD, and their respective free energy is calculated using free energy integration methods.[15] In this regard, our approach is similar to the work of Godawat and coworkers, who investigated the cavity formation free energy at self-assembled monolayers for large cavities (up to ~10 Å).[37]

Exemplary cavity formation free energies $F_{\mathrm{cav}}^{\mathrm{MBAR}}$ for Pt(111) as a function of distance and cavity radius are plotted in Fig. 1(c). The results obtained for all other surfaces follow an analogous pattern; see below and Fig. S1 of the supplementary material. At most negative z_{cav}, the cavity is still completely inside the metal surface and $F_{\mathrm{cav}}^{\mathrm{MBAR}}$ is correspondingly zero.

We do not include any interaction between the metal and the cavity, since the focus of this work is to understand exclusively the free energy cost of creating a cavity, aka free space, within the solvent. In this regard, our approach is similar to the cavitation free energy costs in implicit solvation models, which have no repulsive interaction between the cavity and the substrate.[38] In order to understand how repulsive interactions between the substrate and a solute within the cavity would modify the overall free energy cost,

© Author(s) 2023

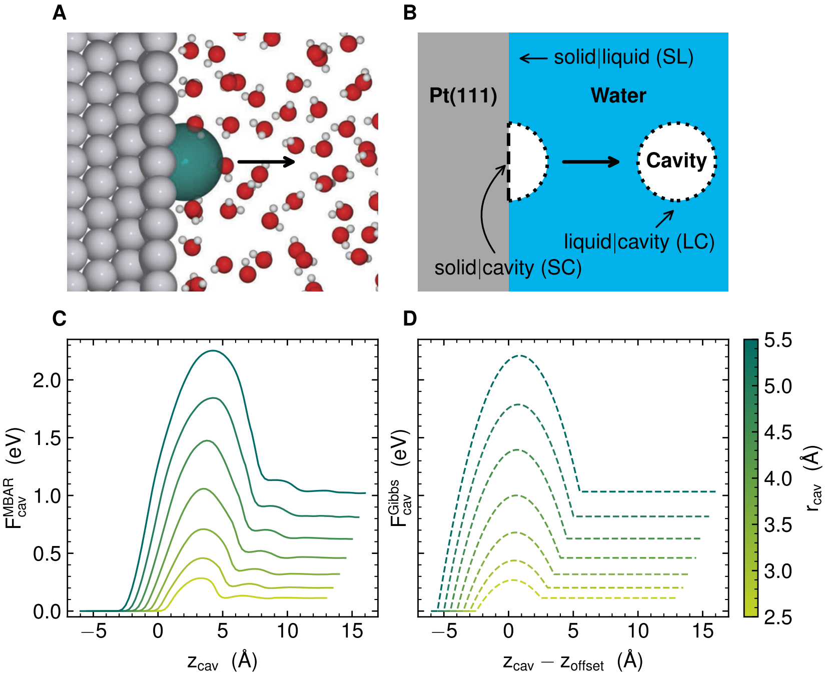

FIG. 1. Cavity formation at a Pt(111)–water interface. (a) Snapshot from an MD simulation with an explicit cavity cap emerging from the metal surface. (b) Continuum Gibbs model considering a sharp interface between the metal substrate and the solvent. The cavity creates new interfaces of the two subsystems with vacuum inside the cavity. (c) MD-simulated cavity formation free energy $F_{\text{cav}}^{\text{MBAR}}$ as a function of distance of the cavity center to the Pt(111) surface z_{cav}. Results are shown for different cavity radii from 2.5 to 5.5 Å. (d) Corresponding cavity formation free energy $F_{\text{cav}}^{\text{Gibbs}}$ from the Gibbs model fitted to the MD data. Note that the fitting procedure includes a z-shifting (z_{offset}) to align the curves in (c) and (d) (see the text).

15 November 2023 11:25:32

we reevaluated the free energy calculations by adding a repulsive metal–cavity interaction identical to the water–cavity interaction (cf. Fig. S2 of the supplementary material), which leads to a sharp increase in F_{cav} for $z_{\text{cav}} < r_{\text{cav}}$, but the profiles remain unchanged for $z_{\text{cav}} > r_{\text{cav}}$.

With increasing z_{cav}, the cavity formation free energy then rises to an initial peak that is followed by a smaller peak or shoulder before it reaches a constant plateau value. Since all investigated metal surfaces in this study show perfect wetting $(W_{\text{ad}} > 2\gamma_{\text{lv}})$ and are hydrophilic,[28] this overall pattern can be rationalized qualitatively in a straightforward way by the additional cost to remove water from the substrate. With the cavity cap emerging from the metal surface at increasing z_{cav}, more and more water molecules are displaced from the interface to the bulk liquid. This leads to an increase in $F_{\text{cav}}^{\text{MBAR}}$ up to a maximum, beyond which it reduces toward the bulk water level, where the favorable substrate–water interface has been reestablished. Obviously, both the initial peak and the plateau value thus also scale with the size of the cavity.

As explained in Fig. 1(b), we can cast this qualitative understanding into a simple geometric Gibbs model[39,40] that considers the sum of infinitely sharp continuum interfaces introduced by the cavity times their effective interface tensions,

$$\begin{aligned} F_{\text{cav}}^{\text{Gibbs}} &= \gamma_{\text{SC}}\cdot A_{\text{SC}} + \gamma_{\text{LC}}\cdot A_{\text{LC}} - \gamma_{\text{SL}}\cdot A_{\text{SC}} \\ &= \tilde{\gamma}^{\text{Me}}\cdot A_{\text{SC}} + \gamma_{\text{LC}}\cdot A_{\text{LC}}, \end{aligned} \tag{4}$$

where A_{SC} is the contact area of the spherical cavity with the metallic surface and A_{LC} is the surface area of the cavity that is accessible to the solvent [cf. dashed and dotted lines in Fig. 1(b), respectively]. γ_{SC}, γ_{LC}, and γ_{SL} are the effective interface tensions for the different interfaces—solid–cavity (SC), liquid–cavity (LC), and solid–liquid (SL), respectively. $\tilde{\gamma}^{\text{Me}} = (\gamma_{\text{SC}} - \gamma_{\text{SL}})$ thus introduces competitive adsorption by accounting for the substrate-dependent differential cost of removing water from the metal contact area instead of creating an equally sized internal water–vacuum interface as considered in bulk solvation models.

As already mentioned initially, previous studies have clarified that for small cavities, a purely geometric Gibbs model with size-independent interface tensions fails in describing cavity formation in the case of bulk solvation.[7–9,12–15] We correspondingly fit Eq. (4) separately to the MD data obtained for each cavity radius, i.e., $\tilde{\gamma}^{\text{Me}} = \tilde{\gamma}^{\text{Me}}(r_{\text{cav}})$ and $\gamma_{\text{LC}} = \gamma_{\text{LC}}(r_{\text{cav}})$. The areas A_{SC} and A_{LC} are entirely determined by geometric considerations and are given by the cavity radius r_{cav}, the cavity position z_{cav}, and one offset fit parameter $z_{\text{offset}}^{\text{Me}}(r_{\text{cav}})$, which accounts for the shift between the position of the topmost metal layer atoms in the MD simulations and the idealized position of the SLI in the continuum model. $\gamma_{\text{LC}}(r_{\text{cav}})$ is assumed to be independent of the metal surface, consistent with a substrate-independent cavitation energy in bulk water. It is important to note here that making interface energies in Eq. (4) size-dependent allows us to capture any functional dependence on r_{cav}, including from common correction terms, such as the line tension. Figure 1(d)

© Author(s) 2023

shows $F_{\text{cav}}^{\text{Gibbs}}$ obtained from the fit for Pt(111). It compares almost perfectly with the simulated $F_{\text{cav}}^{\text{MBAR}}$ shown in Fig. 1(c), except for the second peak/shoulder. This feature is probably caused by the second water layer, which is not accounted for in the present Gibbs model and thus absent in $F_{\text{cav}}^{\text{Gibbs}}$. Previous studies on Au(100)[36,41] and Pt(100)/Pt(111)[35] reported a reduced cavity formation between the first and second water layers for small cavities. In addition, the study by Serva and co-workers reported that with increasing size, this position becomes unfavorable because the gap between the layers fits only small cavities.[36] Our results show the same behavior for the small cavities ($r_{\text{cav}} \leq 3$ Å), for which the profile in Fig. 1(b) shows a minimum between the two peaks caused by the water layers. For larger cavities, this becomes a shoulder and the cavity is destabilized compared to the bulk. A comparison of the heights of the two peaks clarifies that the cavity formation energy at the interface is dominated by the first water layer, which justifies the omission of second water layer effects in our energy model. It should be kept in mind, though, that the contribution of the second water layer can be ~0.15 eV for larger cavities.

Figure 2 shows the cavity-size dependence of the parameters $\gamma_{\text{LC}}(r_{\text{cav}})$ and $\tilde{\gamma}^{\text{Me}}(r_{\text{cav}})$ for Me = Pt. The results obtained for all other surfaces are listed in Table S2 of the supplementary material. Both interface tensions increase with cavity size. The roughly linear scaling for $r_{\text{cav}} \lesssim 4$ Å will lead to a cavity formation energy that scales proportional to the cavity volume, as often also included in continuum solvation models.[38,42,43] The saturation of $\gamma_{\text{LC}}(r_{\text{cav}})$ and $\tilde{\gamma}^{\text{Pt}}(r_{\text{cav}})$ slowly setting in for the larger r_{cav} values, in turn, indicates the approach to the area-scaling F_{cav} of an infinitely large cavity. The absolute values of $\gamma_{\text{LC}}(r_{\text{cav}})$ are in almost perfect quantitative agreement with those determined in earlier bulk cavity formation studies by Hummer *et al.*,[13] Floris *et al.*,[14] and Grigor'ev *et al.*[9]; cf. Figure 2(b). We attribute the small differences at larger cavities to differences in the employed water potential. The SPC model[44] employed by Hummer *et al.* and us (CVFF)[27] is known to underestimate the surface tension of liquid water[45] as compared to the TIP4P model[46] employed by Floris *et al.* and Grigor'ev *et al.*

We can accurately interpolate the similar and smooth size dependencies of $\tilde{\gamma}^{\text{Me}}(r_{\text{cav}})$ and $\gamma_{\text{LC}}(r_{\text{cav}})$ with the following expressions:

$$\begin{aligned} \tilde{\gamma}^{\text{Me}}(r_{\text{cav}}) &= k_0^{\text{Me}}/r_{\text{cav}}^2 + k_1^{\text{Me}}/r_{\text{cav}} + \tilde{\gamma}_\infty^{\text{Me}}, \\ \gamma_{\text{LC}}(r_{\text{cav}}) &= k_0^{\text{water}}/r_{\text{cav}}^2 + k_1^{\text{water}}/r_{\text{cav}} + \gamma_{\text{LV}}, \end{aligned} \tag{5}$$

where $\tilde{\gamma}_\infty^{\text{Me}}$ is the difference of the macroscopic solid–vapor and SL interface tensions and γ_{LV} is the afore-introduced macroscopic surface tension of liquid water. The coefficients $k_0^{\text{water}}, k_1^{\text{water}}$ (and analogously $k_0^{\text{Me}}, k_1^{\text{Me}}$) relate to the coefficients of the polynomial expansion in r_{cav} for the cavity formation free energy on the basis of SPT as performed by Pierotti.[11] Mapping this expansion in r_{cav} back onto surface areas (r_{cav}^2) then naturally yields Eq. (5). The next higher order term that is proportional to the cavity volume was shown to be negligible at atmospheric pressures[8] and is apparently also not required for the data in Fig. 2. Within SPT, the coefficient k_1 is negative—consistent with the observations here—and related to the density of the liquid and the curvature of the cavity.[11,47] The other coefficient k_0 emerges from the atomistic dimension of the cavity and is absent in macroscopic thermodynamic descriptions.[8] Taking published $\tilde{\gamma}_\infty^{\text{Me}}$ for the employed interatomic potentials[28] and γ_{LV} from independent own simulations, we fit the coefficients k_0^{Me}, k_1^{Me} and k_0^{water}, k_1^{water} to obtain the accurate interpolations shown in Fig. 2 for Pt(111) and in Fig. S1 of the supplementary material for the other metals. The fitted coefficients for all interfaces are listed in Table S3 of the supplementary material. This accuracy, together with the overall similar size variations in $\tilde{\gamma}^{\text{Me}}(r_{\text{cav}})$ and $\gamma_{\text{LC}}(r_{\text{cav}})$, suggests that SPT considerations apply as well for the free energy cost of creating the two-dimensional cavity contact area at an SLI.

Furthermore, we performed additional free energy calculations for Pt(111) with a chain of cavities to test the applicability of Eq. (4). The chain consists of three stacked cavities, where the lowest cavity is centered in the interfacial water layer. We compared this setup with results for a single cavity placed at the same position. For a fixed total excluded volume, the two setups create different amounts of the areas A_{LC} and A_{SC}. Since the chain creates less A_{SC}, its cavity formation free energy is for all investigated excluded volumes lower than an equivalent single cavity at the interface, even though its total surface area is greater. Applying Eq. (4) and taking the coefficients from Table S2 of the supplementary material for both setups yields results in good agreement with the free energy calculations. These findings underline the possibility of separating interfacial cavity formation into two components, which depend on the solvent ($\gamma_{\text{LC}} \times A_{\text{LC}}$) and the substrate–solvent interface ($\tilde{\gamma}^{\text{Me}} \times A_{\text{SC}}$).

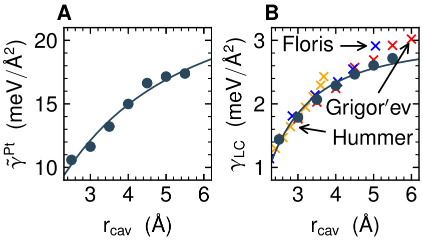

FIG. 2. Fitted parameters of the Gibbs model for the Pt(111)–water SLI as a function of cavity radius r_{cav}. (a) Effective interface tension $\tilde{\gamma}^{\text{Pt}}$ as extracted from the MD simulations (circles) and fit according to Eq. (5) (solid line). (b) Same for the effective surface tension for bulk water γ_{LC} (circles and solid line). The standard deviation is smaller than the size of the marker. The crosses show the reference data from bulk simulations of Floris *et al.* (blue),[14] Hummer *et al.* (orange),[13] and Grigor'ev *et al.* (red).[9]

B. Variation with substrate

Figure 3(a) shows the MD-simulation results for the cavity formation free energy for Ni(111), Au(111), and Pb(111) and for a cavity radius of 5.5 Å. The corresponding data for the other metal surfaces and cavity sizes are provided in Fig. S1 of the supplementary material. All $F_{\text{cav}}^{\text{MBAR}}$ collapse for $z_{\text{cav}} > 11$ Å. At these large distances from the surface, the cavity is fully immersed in the water and we consistently recover the substrate-independent bulk cavity formation free energy value. In contrast, a strong substrate dependence results for the prominent first peak where the cavity cap emerges from the surface—and to a lesser degree also for the small second peak/shoulder attributed to the second water layer. Not surprisingly from the perspective of competitive adsorption, this substrate dependence correlates with the binding strength of the substrate.

15 November 2023 11:25:32

© Author(s) 2023

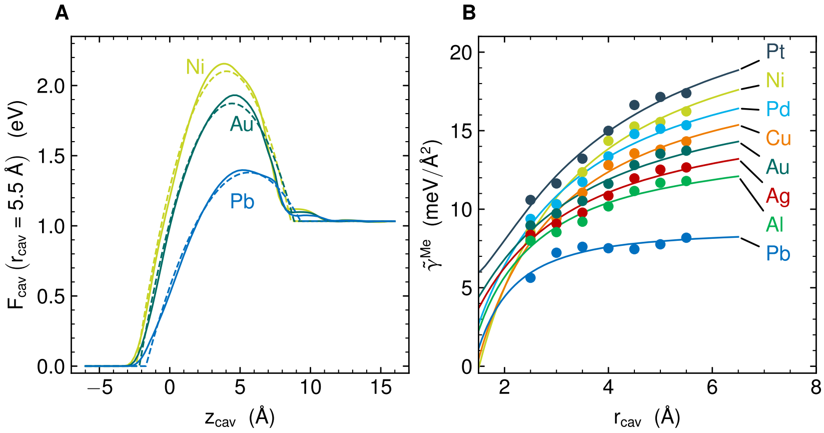

FIG. 3. Substrate dependence of the cavity formation free energy. (a) MD-simulated cavity formation free energy F_{cav}^{MBAR} (solid lines) and fitted Gibbs model F_{cav}^{Gibbs} (dashed lines) as a function of distance z_{cav} above Ni(111), Au(111), and Pb(111). Shown are the data for a fixed cavity radius of r_{cav} = 5.5 Å. (b) Fitted effective interface tension $\tilde{\gamma}^{Me}$ of the continuum Gibbs model as in Fig. 2(a), now for all eight metal surfaces.

It is much less favorable to form the cavity at the strongly binding Ni(111) surface as compared to Pb(111), and the ordering over the eight metals for the formation cost follows the one, for example, expected from the macroscopic work of adhesion of water at these surfaces: Pt > Ni > Pd > Cu > Au > Ag > Al > Pb.[28]

As apparent from Fig. 3(a) and Fig. S1 of the supplementary material, excellent fits to the MD data are also achieved for the other metals and cavity sizes, which then allows us to conveniently discuss the variations over substrates and cavity size on the basis of the $\tilde{\gamma}^{Me}$ interface tension that contributes the competitive adsorption related part to the overall cavity formation free energy. The corresponding data summarized in Fig. 3(b) reveal a size dependence for all metals that is analogous to the one discussed for Pt(111) before. All $\tilde{\gamma}^{Me}$ become smaller for smaller cavities. Intriguingly, they do so with different slopes though. For the strongest binding surfaces with the largest interface tension, the drop of $\tilde{\gamma}^{Me}$ toward smaller r_{cav} is also strongest. Expressed in the parameters of the SPT equation (5), the coefficient k_1^{Me} is thus always negative and more negative for the stronger interacting substrates. This makes perfect sense as denser liquids generally exhibit more negative k_1 coefficients.[8] All here considered surfaces are wetting, which induces a water density peak directly at the SLI; cf. Fig. S4 of the supplementary material. This density peak is stronger for stronger interacting substrates, which, in turn, leads to more negative k_1^{Me} coefficients.

This understanding suggests that k_1^{Me} should also correlate with the adsorption energy of a single water molecule $E_{ads}^{H_2O}$, as the latter is a simple descriptor for the interaction strength at the SLI. The same correlation with $E_{ads}^{H_2O}$ should also hold for the $\tilde{\gamma}_\infty^{Me}$ parameter in Eq. (5), as this difference of the macroscopic solid–vapor and SL interface tensions trivially relates to the work of adhesion at the SLI for which the adsorption energy of a single water molecule is again a suitable descriptor.[48] In fact, we had already seen above that $\tilde{\gamma}^{Me}(r_{cav})$ for the larger cavity radius of 5.5 Å in Fig. 3(b) does follow the ordering expected from the work of adhesion. Figure 4 confirms this expected linear correlation and demonstrates that it also extends to the third parameter k_0^{Me} of the SPT equation (5). Expecting that these simple correlations equally hold for other interaction potentials, for example, from first-principles calculations, suggests then a computationally highly efficient approach to parameterize an interface-aware cavity formation free energy model for

15 November 2023 11:25:32

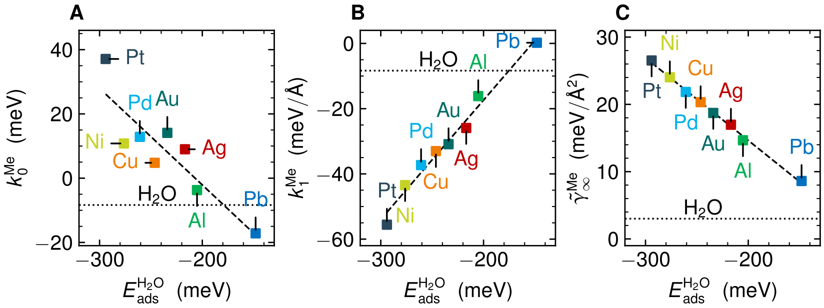

FIG. 4. Simple descriptor for the parameter determination of the Gibbs model. Correlation of all three parameters of the SPT equation (5) for the interface tension $\tilde{\gamma}^{Me}$ with the adsorption energy of a single water molecule $E_{ads}^{H_2O}$: (a) k_0^{Me}, (b) k_1^{Me}, and (c) $\tilde{\gamma}_\infty^{Me}$.

© Author(s) 2023

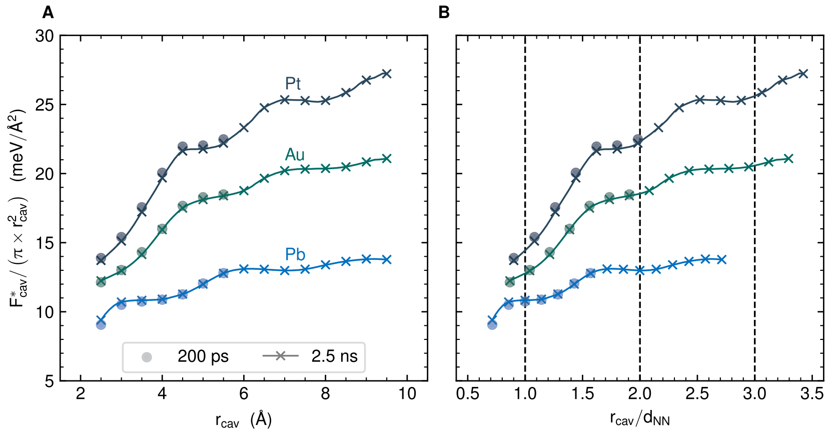

FIG. 5. Comparison of the area-normalized free energy of formation $F^*_{cav}/(\pi r^2_{cav})$ of cavities positioned in the center of the density peak of the first water layer (Pt, Au: z_{cav} = 2.75 Å; Pb: z_{cav} = 3.00 Å) using MD runs of 200 ps and 2.5 ns. The results are plotted against the (a) absolute size of the cavity and (b) the size of the cavity relative to the nearest-neighbor distance d_{NN} with a solid line serving as a guide to the eye. The results demonstrate that convergence is already obtained from 200 ps MD sampling and that the oscillation frequency scales with the lattice of the underlying substrate. Further studies (see the text and supplementary material) confirm that they originate from the sequential exclusion of water adsorption on different adsorption sites.

substrates from all across the periodic system and any surface orientation. In this case, it would be sufficient to simulate ~3 cavity sizes for only two different materials to obtain the slopes and offsets of Figs. 4(a)–4(c). From this, one can then infer the k_0^{Me}, k_1^{Me}, and $\tilde{\gamma}_\infty$ parameters (and therewith $\tilde{\gamma}^{Me}$) for any other material or surface orientation based on the calculation of the adsorption energy of a single water molecule.

C. Effect of the lattice

The careful eye notices that our fit to the data in Fig. 3(b) is not perfect, but the data points rather oscillate around an average trend captured by the fit function. To further investigate this behavior and demonstrate the overall convergence of our setup, we performed a more detailed analysis for Pt, Au, and Pb. Only cavities centered in the adsorbed water layer were considered; however, the studied size range was increased up to 9.5 Å and the MD runtime was significantly extended to 2.5 ns. Free energy differences F^*_{cav} are computed between all sizes and a reference calculation without a cavity. Figure 5(a) displays the area-normalized quantity $F^*_{cav}/\pi r^2_{cav}$ from this and the previous set of calculations (cf. Fig. S1 of the supplementary material), demonstrating the overall convergence and revealing that the oscillations are neither an artifact of our free energy calculation nor the fitting procedure. Renormalizing the cavity size to the substrates' nearest-neighbor distances results in the alignment of the oscillations across all substrates [Fig. 5(b)]. The oscillations thus likely arise from the preference of water to adsorb at specific sites, and an increase in the (normalized) cavity radius leads to the sequential exclusion of different sets of adsorption sites and thus oscillating cavity formation energies. As an example, the blocking of top sites demands less energy for the present force field (see Table S4 of the supplementary material), leading to a shallow slope between $1.7 \leq d_{NN} \leq 2.0$, while the blocking of fcc/hcp sites between $1.1 \leq d_{NN} \leq 1.6$ results in a steep slope. This hypothesis is supported by the observed shifted oscillations, when placing the cavities at a different lateral position (see Fig. S3 of the supplementary material). Although these deviations of ~0.1 eV from the average trend are relevant for small cavities, their magnitude becomes increasingly negligible compared to the overall free energy cost for larger cavities. Similarly, the impact on the differences between different substrate materials is only minor, which justifies our oscillation-free fit with a smooth, low-order polynomial, as above.

Nonetheless, the choice of the force field plays a crucial role in this regard. Static[49,50] and dynamic[51,52] first-principle calculations have shown that water preferably adsorbs on the top site of the investigated metal surfaces. However, the employed force field predicts adsorption on the threefold coordinated hcp and fcc sites (cf. Table S4 of the supplementary material). Therefore, the oscillations in Fig. S3(B) of the supplementary material should have a maximum when we replace water from the favorable top site and a minimum for the less favorable hcp/fcc sites for more realistic models. The amplitude depends likely on the energetic difference between the adsorption sites.

Finally, the interface tension $\tilde{\gamma}^{Me}$ of the metal–water interface and the convergence tendency (k_0^{Me}, k_1^{Me}) against this value might be affected by a different calculation method as well. However, the comparison with the existing theoretical and experimental benchmarks in Sec. IV underlines that our results are within a reasonable range.

IV. SUMMARY AND CONCLUSION

Our results demonstrate that cavity formation at solid–liquid interfaces is strongly substrate-dependent and that the observed trends are fully consistent with the idea of competitive adsorption. In general, cavitation energies F_{cav} increase with cavity size and substrate reactivity. Both dependencies can be fully rationalized based on a simple geometric Gibbs model that explains F_{cav} via the free energy cost of introduced interfaces—namely the cavity–solvent and cavity–solid interfaces. The creation of the cavity–solid interface is

15 November 2023 11:25:32

© Author(s) 2023

associated with removing interfacial solvent from a given surface contact area, and, as a result, its energy cost correlates with the adsorption strength of individual solvent molecules. Using expressions from SPT, the parameters of the Gibbs model exhibit even a simple, intelligible linear correlation with this adsorption strength. On the one hand, this opens an avenue for the simple parametrization of a general interface-aware cavitation model that could replace the existing bulk cavitation models in common implicit solvation approaches. On the other hand, it suggests that the present insight gained specifically for water is transferable to other solvents as well.

One shortcoming of the current setup is the omission of polarization effects. Therefore, we computed the cavity formation energy on Au(111) with a polarizable force field,[53] which is based on the same framework and adds a core–shell description for the metal. The results agree well with the ones obtained from the non-polarizable force field (cf. Fig. S6 of the supplementary material), which is not surprising since the interface tensions of both models are similar ($\tilde{\gamma}^{\mathrm{Au}} = 0.30$ J m^{-2} vs $\tilde{\gamma}^{\mathrm{Au}}_{\mathrm{pol}} = 0.32$ J m^{-2}).[28,53]

Apart from generating leads to improved solvation models, the here identified trends also provide important insights into the general relevance and effects of competitive adsorption. The observed material- and size-dependence of the effective interface energies leads to cavity formation energies for small adsorbates ($r_{\mathrm{cav}} \approx 3$ Å) that are, on the one hand, significantly smaller than that estimated from the macroscopic interface tensions [e.g., by a factor of 2 for Pt(111)] and that, on the other hand, exhibit a smaller-than-expected spread between the different substrates, which makes the missing account in existing implicit solvation methods less dramatic.[54] However, the account of competitive adsorption is crucial for understanding the stability of large adsorbates.[26,55–57] This is, for example, already the case for phenol[21,22,26,58,59] ($r_{\mathrm{cav}} \approx 4.35$ Å), for which the adsorption energy on Pt(111) in an aqueous environment is smaller by 1.6 eV than in gas phase.[26] While schemes that include explicit solvation through QM/MM setups[21] or the three-dimensional reference interaction site model (3D-RISM)[58] predict a comparable reduction as the experiment, current implicit solvation models leave the adsorption energy in solvent essentially unchanged.[21,22,60,61] However, including cavitation free energy costs via geometric considerations already explains an additional energy cost of ~0.95 eV, as estimated from our model and similarly from the model of Akinola *et al.* (0.92 eV) when assuming a contact area of $A_{\mathrm{SC}} \sim 60$ Å^{2}[26] and $\tilde{\gamma}^{\mathrm{Pt}} = 16$ meV Å^{-2}. An according energy cost can be included in the non-electrostatic cavitation energy descriptions of implicit models by making these curvature- and substrate-dependent—a possible pathway for future improved implementations.

Another important aspect of competitive adsorption in solvent is the reduction in reactivity differences between different substrates or adsorption sites. This arises from the fact that reactive sites are typically more reactive toward not only a given adsorbate but also the solvent molecules, thus leading to higher cavitation costs at more reactive sites and thus to differences in adsorption energies in solvent that are smaller than in vacuum. Trends such as prevalent volcano plots in surface catalysis may, therefore, be distorted when computed in vacuum, with the amount of distortion depending on overall reactivity, e.g., the coordination of considered adsorption site.[60,62] As an example, reactive edge and kink sites that are characterized as too strongly binding or poisoned in vacuum calculations might as well exhibit suitable reactivity upon immersion in solvent.

SUPPLEMENTARY MATERIAL

The supplementary file contains the following:

- Table S1: The lattice constant and number of water molecules for each investigated system.
- Table S2: The effective interface tensions for all investigated sizes and interfaces.
- Table S3: The polynomial coefficients to fit the size-dependent interface tensions.
- Table S4: Adsorption energies of a single water molecule on each metal surface for the different adsorption sites.
- Figure S1: Free energy profiles of all metal–water interfaces for all investigated sizes.
- Figure S2: Free energy profiles of all metal–water interfaces for all investigated sizes, including a repulsive metal–cavity interaction.
- Figure S3: Comparison between the cavity formation free energy at the Pt(111)/water interface for the adsorption on the top and hcp site.
- Figure S4: Oxygen density profile along the surface normal and areal density of adsorbed water molecules on the studied metal substrates as a function of adsorption energy.
- Figure S5: Weeks–Chandler–Andersen potentials for the seven investigated cavity sizes.
- Figure S6: Comparison of cavity formation energies at the Au(111)/water interface as obtained from the non-polarizable and polarizable force fields.
- Figure S7: Comparison of cavity formation energies at the Pt(111)/water interface as obtained for two different cavity geometries (one sphere and a chain of three spheres).

15 November 2023 11:25:32

ACKNOWLEDGMENTS

We acknowledge the financial support from the Deutsche Forschungsgemeinschaft (DFG, German Research Foundation) under Germany's Excellence Strategy—Grant No. EXC 2089/1-390776260. Computations were performed on the HPC system Raven at the Max Planck Computing and Data Facility.

AUTHOR DECLARATIONS

Conflict of Interest

The authors have no conflicts to disclose.

Author Contributions

Thorben Eggert: Conceptualization (equal); Data curation (lead); Formal analysis (lead); Investigation (lead); Methodology (equal); Visualization (lead); Writing – original draft (equal); Writing – review & editing (equal). **Nicolas G. Hörmann**: Conceptualization (equal); Methodology (equal); Supervision (equal); Writing – original draft (equal); Writing – review & editing (equal). **Karsten Reuter**: Conceptualization (equal); Funding acquisition (equal);

© Author(s) 2023

Supervision (equal); Writing – original draft (equal); Writing – review & editing (equal).

DATA AVAILABILITY

The results of the interface tensions for all investigated systems and the obtained coefficients for Eq. (5) are tabulated in the supplementary file. In addition, it contains information about the setup (lattice constant and number of water molecules) for each system.

The data for the energy profiles (resulting from the free energy integration, the initially fitted Gibbs model, and the model using the observed linear relations) are uploaded to https://doi.org/10.17617/3.WERJXN, together with an exemplary input script.

APPENDIX: EFFECTIVE SURFACE TENSION OF WATER

The effective surface tension for bulk water $\gamma_{\mathrm{LC}}(r_{\mathrm{cav}})$ was fitted to the free energy profile in the range between $z_{\mathrm{top}} + r_{\mathrm{cut}} + 5$ Å and $z_{\mathrm{top}} + r_{\mathrm{cut}} + 10$ Å. This ensures that the cavity is always fully surrounded by bulk water, and therefore, the cavity formation energy is constant. After fixing $\gamma_{\mathrm{LC}}(r_{\mathrm{cav}})$, the effective interface tensions $\tilde{\gamma}^{\mathrm{Me}}(r_{\mathrm{cav}})$ and $z^{\mathrm{Me}}_{\mathrm{offset}}$ were fitted through Eq. (4) and shifting of the free energy profile. The macroscopic surface tension of liquid water γ_{LV} was calculated from the ensemble-averaged pressure tensor[63] via

$$\gamma_{\mathrm{LV}} = \frac{L_z}{2}\left\langle p_{zz} - \frac{1}{2}\left(p_{xx} + p_{yy}\right)\right\rangle. \tag{A1}$$

For this purpose, we created a cube of $(40\ \text{Å})^3$ filled with 2140 water molecules. After adding 30 Å of vacuum along the z direction on both sides and running an NVT-MD for 10 ns, we determined a surface tension of 48.2 mJ m^{-2}.

REFERENCES

[1] O. Björneholm, M. H. Hansen, A. Hodgson, L.-M. Liu, D. T. Limmer, A. Michaelides, P. Pedevilla, J. Rossmeisl, H. Shen, G. Tocci, E. Tyrode, M.-M. Walz, J. Werner, and H. Bluhm, "Water at interfaces," Chem. Rev. **116**, 7698–7726 (2016).

[2] V. Molinero and E. B. Moore, "Water modeled as an intermediate element between carbon and silicon," J. Phys. Chem. B **113**, 4008–4016 (2009).

[3] K. Forster-Tonigold and A. Groß, "Dispersion corrected RPBE studies of liquid water," J. Chem. Phys. **141**, 064501 (2014).

[4] M. J. Gillan, D. Alfè, and A. Michaelides, "Perspective: How good is DFT for water?," J. Chem. Phys. **144**, 130901 (2016).

[5] J. Tomasi and M. Persico, "Molecular interactions in solution: An overview of methods based on continuous distributions of the solvent," Chem. Rev. **94**, 2027–2094 (1994).

[6] J. Tomasi, B. Mennucci, and R. Cammi, "Quantum mechanical continuum solvation models," Chem. Rev. **105**, 2999–3094 (2005).

[7] D. Chandler, "Interfaces and the driving force of hydrophobic assembly," Nature **437**, 640–647 (2005).

[8] S. Höfinger and F. Zerbetto, "Simple models for hydrophobic hydration," Chem. Soc. Rev. **34**, 1012 (2005).

[9] F. V. Grigor'ev, M. V. Bazilevskii, S. N. Zhabin, A. N. Romanov, and V. B. Sulimov, "Calculations of the Gibbs energy of formation of cavities in water," Russ. J. Phys. Chem. **82**, 517–525 (2008).

[10] H. Reiss, H. L. Frisch, and J. L. Lebowitz, "Statistical mechanics of rigid spheres," J. Chem. Phys. **31**, 369–380 (1959).

[11] R. A. Pierotti, "A scaled particle theory of aqueous and nonaqueous solutions," Chem. Rev. **76**, 717–726 (1976).

[12] A. Pohorille and L. R. Pratt, "Cavities in molecular liquids and the theory of hydrophobic solubilities," J. Am. Chem. Soc. **112**, 5066–5074 (1990).

[13] G. Hummer, S. Garde, A. E. García, A. Pohorille, and L. R. Pratt, "An information theory model of hydrophobic interactions," Proc. Natl. Acad. Sci. U. S. A. **93**, 8951–8955 (1996).

[14] F. M. Floris, M. Selmi, A. Tani, and J. Tomasi, "Free energy and entropy for inserting cavities in water: Comparison of Monte Carlo simulation and scaled particle theory results," J. Chem. Phys. **107**, 6353–6365 (1997).

[15] I. Sedov and T. Magsumov, "The Gibbs free energy of cavity formation in a diverse set of solvents," J. Chem. Phys. **153**, 134501 (2020).

[16] D. A. Scherlis, J.-L. Fattebert, F. Gygi, M. Cococcioni, and N. Marzari, "A unified electrostatic and cavitation model for first-principles molecular dynamics in solution," J. Chem. Phys. **124**, 074103 (2006).

[17] O. Andreussi, I. Dabo, and N. Marzari, "Revised self-consistent continuum solvation in electronic-structure calculations," J. Chem. Phys. **136**, 064102 (2012).

[18] A. V. Marenich, C. J. Cramer, and D. G. Truhlar, "Generalized Born solvation model SM12," J. Chem. Theory Comput. **9**, 609–620 (2013).

[19] J. Zhang, H. Zhang, T. Wu, Q. Wang, and D. van der Spoel, "Comparison of implicit and explicit solvent models for the calculation of solvation free energy in organic solvents," J. Chem. Theory Comput. **13**, 1034–1043 (2017).

[20] H. H. Heenen, J. A. Gauthier, H. H. Kristoffersen, T. Ludwig, and K. Chan, "Solvation at metal/water interfaces: An *ab initio* molecular dynamics benchmark of common computational approaches," J. Chem. Phys. **152**, 144703 (2020).

[21] P. Clabaut, B. Schweitzer, A. W. Götz, C. Michel, and S. N. Steinmann, "Solvation free energies and adsorption energies at the metal/water interface from hybrid quantum-mechanical/molecular mechanics simulations," J. Chem. Theory Comput. **16**, 6539–6549 (2020).

[22] G. Bramley, M.-T. Nguyen, V.-A. Glezakou, R. Rousseau, and C.-K. Skylaris, "Reconciling work functions and adsorption enthalpies for implicit solvent models: A Pt (111)/water interface case study," J. Chem. Theory Comput. **16**, 2703–2715 (2020).

[23] S. N. Steinmann, P. Sautet, and C. Michel, "Solvation free energies for periodic surfaces: Comparison of implicit and explicit solvation models," Phys. Chem. Chem. Phys. **18**, 31850–31861 (2016).

[24] S. Ringe, N. G. Hörmann, H. Oberhofer, and K. Reuter, "Implicit solvation methods for catalysis at electrified interfaces," Chem. Rev. **122**, 10777–10820 (2022).

[25] H. H. Kristoffersen, J.-E. Shea, and H. Metiu, "Catechol and HCl adsorption on $\mathrm{TiO_2}$(110) in vacuum and at the water–$\mathrm{TiO_2}$ interface," J. Phys. Chem. Lett. **6**, 2277–2281 (2015).

[26] J. Akinola, C. T. Campbell, and N. Singh, "Effects of solvents on adsorption energies: A general bond-additivity model," J. Phys. Chem. C **125**, 24371–24380 (2021).

[27] P. Dauber-Osguthorpe, V. A. Roberts, D. J. Osguthorpe, J. Wolff, M. Genest, and A. T. Hagler, "Structure and energetics of ligand binding to proteins: *Escherichia coli* dihydrofolate reductase-trimethoprim, a drug-receptor system," Proteins: Struct., Funct., Bioinf. **4**, 31–47 (1988).

[28] H. Heinz, R. A. Vaia, B. L. Farmer, and R. R. Naik, "Accurate simulation of surfaces and interfaces of face-centered cubic metals using 12–6 and 9–6 Lennard-Jones potentials," J. Phys. Chem. C **112**, 17281–17290 (2008).

[29] A. Hjorth Larsen, J. Jørgen Mortensen, J. Blomqvist, I. E. Castelli, R. Christensen, M. Dułak, J. Friis, M. N. Groves, B. Hammer, C. Hargus, E. D. Hermes, P. C. Jennings, P. Bjerre Jensen, J. Kermode, J. R. Kitchin, E. Leonhard Kolsbjerg, J. Kubal, K. Kaasbjerg, S. Lysgaard, J. Bergmann Maronsson, T. Maxson, T. Olsen, L. Pastewka, A. Peterson, C. Rostgaard, J. Schiøtz, O. Schütt, M. Strange, K. S. Thygesen, T. Vegge, L. Vilhelmsen, M. Walter, Z. Zeng, and K. W. Jacobsen, "The atomic simulation environment—A Python library for working with atoms," J. Phys.: Condens. Matter **29**, 273002 (2017).

[30] L. Martínez, R. Andrade, E. G. Birgin, and J. M. Martínez, "PACKMOL: A package for building initial configurations for molecular dynamics simulations," J. Comput. Chem. **30**, 2157–2164 (2009).

[31] A. P. Thompson, H. M. Aktulga, R. Berger, D. S. Bolintineanu, W. M. Brown, P. S. Crozier, P. J. in 't Veld, A. Kohlmeyer, S. G. Moore, T. D. Nguyen, R. Shan, M. J. Stevens, J. Tranchida, C. Trott, S. J. Plimpton, and S. J. Plimpton,

15 November 2023 11:25:32

© Author(s) 2023

"LAMMPS—A flexible simulation tool for particle-based materials modeling at the atomic, meso, and continuum scales," Comput. Phys. Commun. **271**, 108171 (2022).

[32] D. M. Heyes and H. Okumura, "Some physical properties of the Weeks–Chandler–Andersen fluid," Mol. Simul. **32**, 45–50 (2006).

[33] D. Ben-Amotz and G. Stell, "Reformulation of Weeks–Chandler–Andersen perturbation theory directly in terms of a hard-sphere reference system," J. Phys. Chem. B **108**, 6877–6882 (2004).

[34] M. R. Shirts and J. D. Chodera, "Statistically optimal analysis of samples from multiple equilibrium states," J. Chem. Phys. **129**, 124105 (2008).

[35] D. T. Limmer, A. P. Willard, P. Madden, and D. Chandler, "Hydration of metal surfaces can be dynamically heterogeneous and hydrophobic," Proc. Natl. Acad. Sci. U. S. A. **110**, 4200–4205 (2013).

[36] A. Serva, M. Salanne, M. Havenith, and S. Pezzotti, "Size dependence of hydrophobic hydration at electrified gold/water interfaces," Proc. Natl. Acad. Sci. U. S. A. **118**, e2023867118 (2021).

[37] R. Godawat, S. N. Jamadagni, and S. Garde, "Characterizing hydrophobicity of interfaces by using cavity formation, solute binding, and water correlations," Proc. Natl. Acad. Sci. U. S. A. **106**, 15119–15124 (2009).

[38] O. Andreussi, N. G. Hörmann, F. Nattino, G. Fisicaro, S. Goedecker, and N. Marzari, "Solvent-aware interfaces in continuum solvation," J. Chem. Theory Comput. **15**, 1996–2009 (2019).

[39] J. W. Gibbs, *Collected Works* (Yale University Press, New Haven, 1948), Vol. I, pp. 219–237.

[40] G. G. Láng, "Basic interfacial thermodynamics and related mathematical background," ChemTexts **1**, 16 (2015).

[41] A. Serva, M. Havenith, and S. Pezzotti, "The role of hydrophobic hydration in the free energy of chemical reactions at the gold/water interface: Size and position effects," J. Chem. Phys. **155**, 204706 (2021).

[42] J. Dzubiella, J. M. J. Swanson, and J. A. McCammon, "Coupling nonpolar and polar solvation free energies in implicit solvent models," J. Chem. Phys. **124**, 084905 (2006).

[43] J. A. Wagoner and N. A. Baker, "Assessing implicit models for nonpolar mean solvation forces: The importance of dispersion and volume terms," Proc. Natl. Acad. Sci. U. S. A. **103**, 8331–8336 (2006).

[44] H. J. C. Berendsen, J. P. M. Postma, W. F. van Gunsteren, and J. Hermans, "Interaction models for water in relation to protein hydration," in *Intermolecular Forces: Proceedings of the Fourteenth Jerusalem Symposium on Quantum Chemistry and Biochemistry Held in Jerusalem, Israel, April 13–16, 1981*, edited by B. Pullman (Springer, Netherlands, Dordrecht, 1981), pp. 331–342.

[45] S. P. Kadaoluwa Pathirannahalage, N. Meftahi, A. Elbourne, A. C. G. Weiss, C. F. McConville, A. Padua, D. A. Winkler, M. Costa Gomes, T. L. Greaves, T. C. Le, Q. A. Besford, and A. J. Christofferson, "Systematic comparison of the structural and dynamic properties of commonly used water models for molecular dynamics simulations," J. Chem. Inf. Model. **61**, 4521–4536 (2021).

[46] W. L. Jorgensen, J. Chandrasekhar, J. D. Madura, R. W. Impey, and M. L. Klein, "Comparison of simple potential functions for simulating liquid water," J. Chem. Phys. **79**, 926–935 (1983).

[47] R. C. Tolman, "The effect of droplet size on surface tension," J. Chem. Phys. **17**, 333–337 (1949).

[48] S. Gim, K. J. Cho, H.-K. Lim, and H. Kim, "Structure, dynamics, and wettability of water at metal interfaces," Sci. Rep. **9**, 14805 (2019).

[49] A. Michaelides, "Density functional theory simulations of water–metal interfaces: Waltzing waters, a novel 2D ice phase, and more," Appl. Phys. A **85**, 415–425 (2006).

[50] J. Carrasco, A. Michaelides, and M. Scheffler, "Insight from first principles into the nature of the bonding between water molecules and 4*d* metal surfaces," J. Chem. Phys. **130**, 184707 (2009).

[51] S. Schnur and A. Groß, "Properties of metal–water interfaces studied from first principles," New J. Phys. **11**, 125003 (2009).

[52] S. Sakong and A. Groß, "Water structures on a Pt(111) electrode from *ab initio* molecular dynamic simulations for a variety of electrochemical conditions," Phys. Chem. Chem. Phys. **22**, 10431–10437 (2020).

[53] I. L. Geada, H. Ramezani-Dakhel, T. Jamil, M. Sulpizi, and H. Heinz, "Insight into induced charges at metal surfaces and biointerfaces using a polarizable Lennard–Jones potential," Nat. Commun. **9**, 716 (2018).

[54] J. Park and L. T. Roling, "Elucidating energy scaling between atomic and molecular adsorbates in the presence of solvent," AIChE J. **66**, e17036 (2020).

[55] J. O. Bockris and K. T. Jeng, "In-situ studies of adsorption of organic compounds on platinum electrodes," J. Electroanal. Chem. **330**, 541–581 (1992).

[56] N. Singh and C. T. Campbell, "A simple bond-additivity model explains large decreases in heats of adsorption in solvents versus gas phase: A case study with phenol on Pt(111) in water," ACS Catal. **9**, 8116–8127 (2019).

[57] J. R. Rumptz and C. T. Campbell, "Adhesion energies of solvent films to Pt(111) and Ni(111) surfaces by adsorption calorimetry," ACS Catal. **9**, 11819–11825 (2019).

[58] A. Takamatsu, M. Higashi, and H. Sato, "Free energy and solvation structure analysis for adsorption of aromatic molecules at Pt(111)/water interface by 3D-RISM theory," Chem. Lett. **51**, 791–795 (2022).

[59] M. Zare, M. S. Saleheen, N. Singh, M. J. Uline, M. Faheem, and A. Heyden, "Liquid-phase effects on adsorption processes in heterogeneous catalysis," JACS Au **2**, 2119–2134 (2022).

[60] J. Akinola, I. Barth, B. R. Goldsmith, and N. Singh, "Adsorption energies of oxygenated aromatics and organics on rhodium and platinum in aqueous phase," ACS Catal. **10**, 4929–4941 (2020).

[61] G. A. Bramley, M.-T. Nguyen, V.-A. Glezakou, R. Rousseau, and C.-K. Skylaris, "Understanding adsorption of organics on Pt(111) in the aqueous phase: Insights from DFT based implicit solvent and statistical thermodynamics models," J. Chem. Theory Comput. **18**, 1849–1861 (2022).

[62] S. D. Beinlich, N. G. Hörmann, and K. Reuter, "Field effects at protruding defect sites in electrocatalysis at metal electrodes?," ACS Catal. **12**, 6143–6148 (2022).

[63] D. Bhatt, J. Newman, and C. J. Radke, "Molecular dynamics simulations of surface tensions of aqueous electrolytic solutions," J. Phys. Chem. B **108**, 9077–9084 (2004).

15 November 2023 11:25:32

© Author(s) 2023